Title
Imaging Electrically-Active Defects in Gallium Arsenide and Cobalt Nanowire Devices

Author
Zutter, Brian

Publication Date
2021

Peer reviewed|Thesis/dissertation

UNIVERSITY OF CALIFORNIA
Los Angeles

Imaging Electrically-Active Defects in Gallium Arsenide and Cobalt Nanowire Devices

A dissertation submitted in partial satisfaction
of the requirements for the degree
Doctor of Philosophy in Physics

by

Brian Zutter

2021

ABSTRACT OF THE DISSERTATION

Imaging Electrically-Active Defects in Gallium Arsenide and Cobalt Nanowire Devices

by

Brian Zutter
Doctor of Philosophy in Physics
University of California, Los Angeles, 2021
Professor Brian C. Regan, Chair

Abstract

Nanostructured materials are of critical importance in modern electronic devices. Semiconducting channels of sub-10 nm critical dimension are the primary active components of the smallest transistors. Electric current is transported to these transistors through equally small metallic vias. Crystalline defects play a critical role in the performance of such small devices. An individual vacancy-interstitial point defect, whether introduced through fabrication or through radiation damage, can dramatically alter the performance of a semiconductor device. In metallic interconnects, electromigration (EM) at high current densities causes a flux of atomic vacancies, eventually leading to failure.

Aberration-corrected scanning transmission electron microscopy (STEM) can resolve individual point defects within nanostructured devices, but is blind to the electronic impact of such defects. In the first half of this dissertation, we locate and characterize electrically-active vacancy-interstitial point defects within gallium arsenide nanowire devices using high-resolution STEM electron beam-induced current (EBIC). We directly measure the radius of the 9.6 ± 0.4 nm e-h generation volume of the STEM beam within the nanowire, which sets the limit of EBIC's electronic resolution. This high resolution allows us to directly map a decrease in minority-carrier diffusion length, due to increased surface recombination, across the width of the 135 nm diameter nanowire device.

If the primary beam energy is raised to 300 kV, vacancy-interstitial defects can be precisely introduced with the electron beam. In real time, the electronic impact of these inserted defects is subsequently recorded with EBIC. In some cases defect insertion events can be localized to within a single sub-nm pixel, by recording abrupt changes in EBIC signal as the beam rasters. The location of these defects, obvious in the EBIC image, is completely invisible in typical STEM imaging channels.

Cobalt is being investigated as a next-generation interconnect material to replace copper, due to its superior EM resistance at small critical dimensions. However, cobalt's EM behavior is complex and poorly understood. In the second half of this dissertation we use electron-energy loss spectroscopy (EELS) to monitor EM-induced stress and thickness changes in cobalt nanowires under bias *in situ* . EM is strongly dependent on temperature, and nanowire devices under high current density can Joule heat significantly. To account for increases in temperature influencing EM we develop high-resolution techniques such as plasmon-energy expansion thermometry (PEET) and 4D-STEM to measure temperature directly within nanoscale interconnects. Not only can strain due to Joule heating be measured with nanoscale spatial resolution, but so can strain due to the electron-wind force, the root cause of EM. Bias-dependent changes in plasmon energy allows us to measure cobalt's effective ionic charge $Z^* = +0.62 \pm 0.09$ at $400 \pm 20^\circ$ C.

Under high current density, the nanowire heats significantly due to Joule heating, and the grain structure changes dramatically. We observe secondary grain growth of the hcp phase that is accelerated by EM: Grains on the anode of the nanowire are consistently larger than grains on the cathode. Control of secondary grain growth with an electric current may allow engineering of grains which are larger compared to grains achieved by an equivalent anneal, and may further increase a cobalt nanowire's EM resistance. This possibility, along with the STEM-EBIC techniques developed in gallium arsenide, pave the way towards more failure-resistant nanoscale devices.

The dissertation of Brian Zutter is approved.

Jianwei (John) Miao

Hongwen Jiang

Timothy Fisher

Brian C. Regan, Committee Chair

University of California, Los Angeles

2021

I dedicate this thesis to my wife, Erin, and to my parents.

Erin you have done so much to support me through all the highs and lows.

I couldn't have finished this journey without you.

To my mother and father

who have worked tirelessly for my sister and me.

so that we can pursue our dreams. I am forever grateful.

I couldn't have started this journey without you.

TABLE OF CONTENTS

List of Figures . . . . . **viii**

Acknowledgments . . . . . **xi**

Vita . . . . . **xiii**

1 Introduction **1**

1.1 Scanning Transmission Electron Microscopy 1

1.2 *In Situ* Sample Fabrication 6

2 High-Resolution STEM EBIC characterization of Surface and Point Defects in Gallium Arsenide Nanowire Heterojunctions **9**

2.1 Introduction to Electron-Beam Induced Current 9

2.2 Nanowire substrate preparation 15

2.3 Nanowire growth parameters 15

2.4 Electrical transport data in nanowire devices 24

2.5 Characterization of Electrically-Active Frenkel Defects in GaAs Nanowire Devices with STEM EBIC 26

2.6 Direct Measurement of e-h Generation Volume in STEM 40

2.6.1 Validity of the 1-D Approximation 43

2.7 Measurement of Charge-Collection Efficiency with STEM EBIC 48

2.8 EBIC's structural resolution limit 54

3 Strain and Temperature Measurement with 4D-STEM and PEET **56**

3.1 Introduction to 4D-STEM 56

3.2 Extracting Temperature from Strain Measurements 58
3.3 Mapping Temperature with Plasmon Energy Expansion Thermometry 63

4 Mapping Electromigration and Temperature in Cobalt Nanowires 67
4.1 Introduction to Electromigration 68
4.2 Optimization of Multi-Peak Fit Windows 69
4.3 PEET in Cobalt by Multi-Peak Fitting 75
4.4 Plasmon Energy Expansion Thermometry (PEET) 79
4.5 Measuring Temperature in Cobalt Nanowires via the TCR 80
4.6 Electromigration-Driven Grain Growth in Cobalt Nanowires 89
4.7 *Ex Situ* Analysis of Cobalt Grain Structure with Transmission Kikuchi Diffraction 96
4.8 Measurement of Effective Ionic Charge (Z^*) in Cobalt 98

5 Conclusion 105

References 107

LIST OF FIGURES

1.1 Diagram of scanning transmission electron microscope 2

1.2 Bright field and high-angle annular dark field images of a Au-GaAs nanowire heterojunction 3

1.3 EELS diagram and cobalt spectrum 5

1.4 In situ TEM biasing platform 7

1.5 Hummingbird Scientific In Situ Biasing Holder 8

2.1 Planar and orthogonal EBIC geometries 10

2.2 EBIC electronic resolution is limited by e-h generation volume size 11

2.3 Everhart's model for electron penetration depth in silicon 13

2.4 The stopping power of silicon 14

2.5 Optical and SEM images of GaAs nanowires on their native growth substrate . . 16

2.6 A cartoon of the mechanical transfer process of nanowires to an *in situ* biasing substrate 18

2.7 SEM images of nanowire transfer and contact deposition 19

2.8 Forming intruded gold nanowire contacts with RTA 21

2.9 STEM imaging of intruded gold nanowire contacts 22

2.10 STEM energy-dispersive spectroscopy of an abrupt Au-GaAs nanowire heterojunction 23

2.11 Electrical transport in an individual nanowire diode device. 24

2.12 Extracting GaAs nanowire resistivity from multiple devices in parallel. 26

2.13 STEM EBIC imaging of a Au-GaAs nanowire heterojunction at 200 kV 28

2.14 Extraction of minority-carrier diffusion length at 200 kV accelerating potential . 30

2.15 High-resolution mapping of the minority-carrier diffusion length at 200 kV accelerating potential 31
2.16 STEM EBIC at 80, 200, and 300 kV accelerating voltage 32
2.17 Annular dark-field, bright-field, and EBIC imaging before and after irradiation with 300 kV STEM electrons. 34
2.18 STEM EBIC before and after annealing 35
2.19 Defect insertion and pinpoint localization with STEM EBIC at 300 kV 39
2.20 One-dimensional convolution of G and CCE 41
2.21 Two-dimensional convolution of g and η 44
2.22 Comparison of 2-D and 1-D convolution of g and η 46
2.23 Accuracy of the one-dimensional g approximation 47
2.24 STEM EBIC profiles acquired at 80, 200 and 300 kV 49
2.25 Stopping power of GaAs and predicted e-h pair generation rate 50
2.26 Charge-collection efficiency across the width of the nanowire 52
2.27 Charge-collection efficiency along the axis of the nanowire 53
2.28 STEM EBIC physical structural resolution 55

3.1 Cartoon of 4-D STEM data acquisition 57
3.2 CBED pattern acquired on a K2 CMOS detector 59
3.3 Grain orientations within a polycrystalline aluminum nanowire. 60
3.4 Strain measured from shifts in G 61
3.5 Temperature in an aluminum nanowire measured with 4D-STEM. 62
3.6 Temperature mapping in a biased aluminum nanowire 66

4.1 Optimizing the fit bounds for an asymmetric ZLP 71
4.2 Optimizing fit bounds for the silicon nitride plasmon 73

4.3 ZLP fit parameters and histograms 74
4.4 Silicon nitride plasmon fit parameters and histograms 76
4.5 Cobalt multi-peak fit window optimization 77
4.6 Optimized cobalt multi-peak fit 79
4.7 PEET temperature profiles across a biased cobalt nanowire. 81
4.8 Heated probe station setup 82
4.9 Measuring temperature via cobalt's TCR. 83
4.10 4-wire transport data and temperature measurements in both polarities 85
4.11 4-wire transport data and temperature measurements in one polarity. 86
4.12 Device architecture and EELS spectra. 88
4.13 Electromigration measured by EELS 90
4.14 Strain measurements across the nanowire. 91
4.15 Correlating 4-wire electrical transport to thickness changes. 93
4.16 Secondary grain growth induced by EM 95
4.17 *Ex-situ* TKD grain analysis of a biased cobalt nanowire 97
4.18 TEAM 1.0 STEM equipped with a Gatan Continuum EELS spectrometer . . . 99
4.19 Plasmon energy maps acquired on a Continuum EELS spectrometer 101
4.20 Changes in plasmon energy due to grain boundaries 102
4.21 Temperature measurement in a cobalt nanowire with a Continuum EELS spectrometer 103
4.22 Maps of electromigration-induced pressure 104

ACKNOWLEDGMENTS

I am immensely grateful to the many people who have helped me over the years in my graduate work. A PhD, and research in general, is truly a team effort. The last year of my PhD was completed during the COVID-19 pandemic, and I am grateful to many for helping me complete my research during exceptionally difficult circumstances.

I thank my advisor Chris Regan for teaching me how to become a better researcher and scientist. In particular, I am grateful for his lessons on improving my scientific writing, which is a critical skill in research. I am also grateful for his willingness to let me work independently, and pursue new research directions that were not initially foreseen.

I would like to thank Matt Mecklenburg for patiently teaching me how to use the Jeol STEM and USC, along with the EELS spectrometer. Much of the work in this thesis is an extension of EELS techniques developed by Matt. I am also extremely grateful for weekend days Matt spent at USC during the COVID-19 pandemic obtaining data which has helped me graduate.

Thanks to Jared Lodico and Billy Hubbard for training me on the Titan STEM at UCLA, and also for many hours of their time training me in various cleanroom fabrication techniques. A special thanks to Jared for many long conversations we had (work related or not) which helped me stay sane over the years. I would also like to give a special thanks to Andy Chan for helping with various sample fabrication steps at UCLA during the pandemic. Special thanks to the cleanroom staff at ISNC and Nanolab at UCLA, in particular Krissy Do, Lorna Tokunaga, Tony Wright, Yuwei Fan, and Hoc Ngo.

I greatly enjoyed working with our collaborators Hyunseok Kim and Dingkun Ren on the EBIC radiation damage project and am grateful for their efforts. Both Hyunseok and Dingkun are MOCVD experts, and together grew the GaAs nanowires upon which much of this thesis is based.

During the final months of my PhD I have relied heavily on the instruments available at the National Center for Electron Microscopy (NCEM) at Lawrence Berkeley National

Laboratory (LBNL). I am immensely grateful for the kind and expert assistance of Rohan Dhall, Karen Bustillo, and Jim Ciston, which has allowed me to access state-of-the-art instruments there during difficult circumstances.

Lastly, I would like to thank my good friend Tony Farina for sparking my interest in science. Tony was like a grandfather to me, a great role model, and made a great impact in his community. I am lucky to have known him.

Work in this thesis was supported by NSF award DMR-1611036, the Semiconductor Research Corporation (SRC), and by NSF STC Grant No. DMR-1548924 (STROBE)

VITA

2010–2014	Undergraduate Reserach Assistant to Prof. Thomas Kuech at the University of Wisconsin-Madison Chemical Engineering Dept
2014	B.S. (Physics) and B.S. (Mathematics), University of Wisconsin-Madison.
2015	M.S. (Physics), UCLA Los Angeles, California.
2014–2018	Teaching Assistant, Physics and Astronomy Department, UCLA.
2018–present	Graduate Research Assistant, Physics and Astronomy Department, UCLA.

PUBLICATIONS

[1] M. Mecklenburg, **B. Zutter**, B.C. Regan. "Thermometry of Silicon Nanoparticles". Physical Review Applied **9**. 014005 (2018).

[2] T. Chang, H. Kim, **B. Zutter**, W. Lee, B.C. Regan, D. Huffaker, **B. Zutter**, B.C. Regan. "Orientation-Controlled Selective-Area Epitaxy of III–V Nanowires on (001) Silicon for Silicon Photonics". Advanced Functional Materials **30**. 2002220 (2020).

[3] W. Hubbard, M. Mecklenburg, J. Lodico, Y. Chen, X. Ling, R. Patil, W. Kessel, G. Flatt, H. Chan, B. Vareskic, G. Bal, **B. Zutter**, B.C. Regan. "Electron-Transparent Thermoelectric Coolers Demonstrated with Nanoparticle and Condensation Thermometry". ACS Nano **14**. 11510-11517 (2020).

[4] W. Hubbard, J. Lodico, X. Ling, **B. Zutter**, Y. Yu, D. Shapiro, B.C. Regan. "Differential

electron yield imaging with STXM". Ultramicroscopy **222**. 113198 (2021).

[5] **B. Zutter**, H. Kim, W. Hubbard, D. Regn, M. Mecklenburg, D. Huffaker, B.C. Regan "Mapping Charge Recombination and the Effect of Point Defect Insertion in Gallium Arsenide Nanowire Heterojunctions". In Review. (2021).

[6] M. Mecklenburg, **B. Zutter**, W. Hubbard, X. Ling, B.C. Regan "The Electron Wind Force in the Elastic Regime". In Preparation. (2021).

[7] **B. Zutter**, M. Mecklenburg, H. Chan, J. Lodico, B.C. Regan. "Asymmetric Grain Growth Induced by Electromigration in Cobalt Nanowires". In Preparation. (2021).

CHAPTER 1

Introduction

1.1 Scanning Transmission Electron Microscopy

Transmission electron microscopy (TEM) is the highest-resolution imaging technique available. Since its first demonstration in 1931 by Max Knoll and Ernst Ruska[1], TEMs have become a ubiquitous and critical material characterization tool in a variety of fields. A variety of imaging modes can be implemented which can measure atomic lattice spacings, determine crystal orientation, and acquire diffraction patterns [2, 3] . TEM's superior resolution over conventional optical microscopy is due, fundamentally, to the much smaller wavelength of electrons versus visible light. An electron within a TEM, accelerated to relativistic speeds with a 300 kV potential, will have a wavelength of 2.2 pm. This wavelength is two orders of magnitude below an average inter-atomic spacing, and over five orders of magnitude below visible light wavelengths[2].

Scanning TEM (STEM) was not developed until the 1970's, significantly after the TEM. Unlike in a TEM, where the sample is illuminated by a parallel beam of electrons, in STEM the sample is scanned by an electron beam which converges to a point (Fig. 1.1). In a modern aberration-corrected STEM the width of the waist of this probe, and the corresponding spatial resolution the STEM, can fall well below[4] 100 pm. The current resolution record of any imaging technique is held by STEM, and with an aberration-corrected STEM (which are now fairly common at large research institutions), individual atoms can be routinely imaged.

As the convergent electron beam rasters across the sample, both elastic and inelastic scattering processes occur. Elastic scattering from crystalline regions in the sample will result in a convergent-beam electron diffraction pattern (CBED) and scatter electrons into

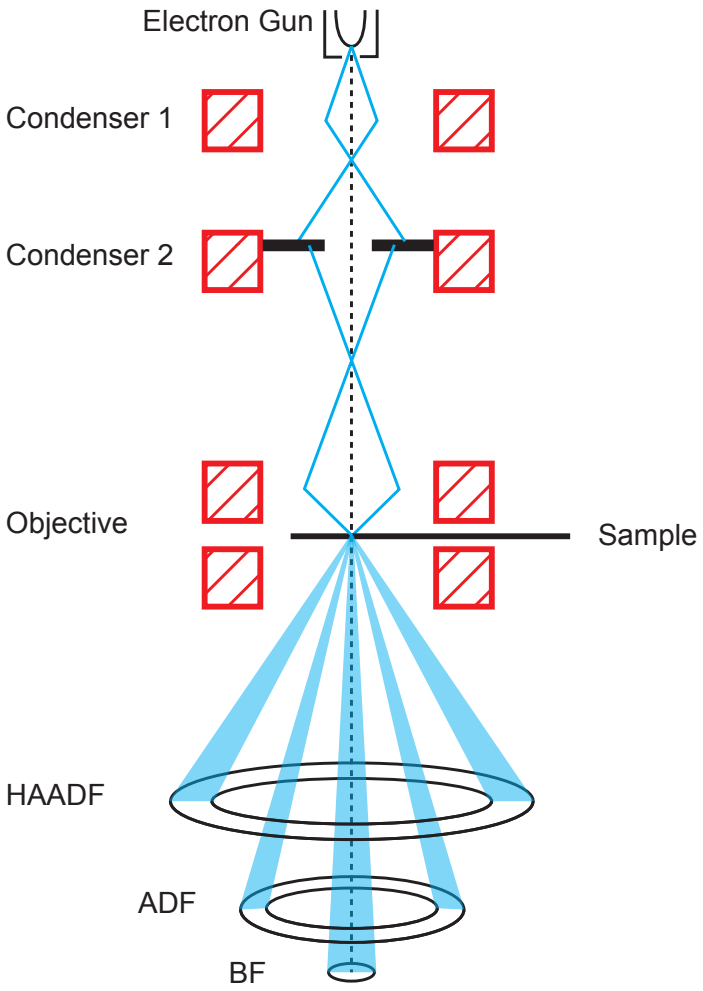

Figure 1.1: **Scanning transmission electron microscope.** A diagram of the electron trajectories within a scanning transmission electron microscope. Hatched red squares represent electromagnetic lenses, and blue lines denote possible electron trajectories.

discrete angles away from the optical axis of the microscope[3]. An annular dark-field (ADF) detector is often placed within an angular range (< 60 mRad) to detect changes in the CBED pattern as the beam rasters across a polycrystalline film. At higher collection angles (> 60 mRad) inelastic Rutherford scattering will dominate the signal, which the high-angle annular dark-field (HAADF) detector collects. HAADF images provide contrast as the product of

Z and thickness, where Z is the atomic charge. At small collection angles near the optical axis (< 4 mRad), electrons are nearly coherent, and phase-shifts due to interactions with the nuclei of atoms in the sample can be detected by a circular bright-field (BF). Analogously to bright-field optical microscopy, coherent BF images are often called "phase-contrast" images.

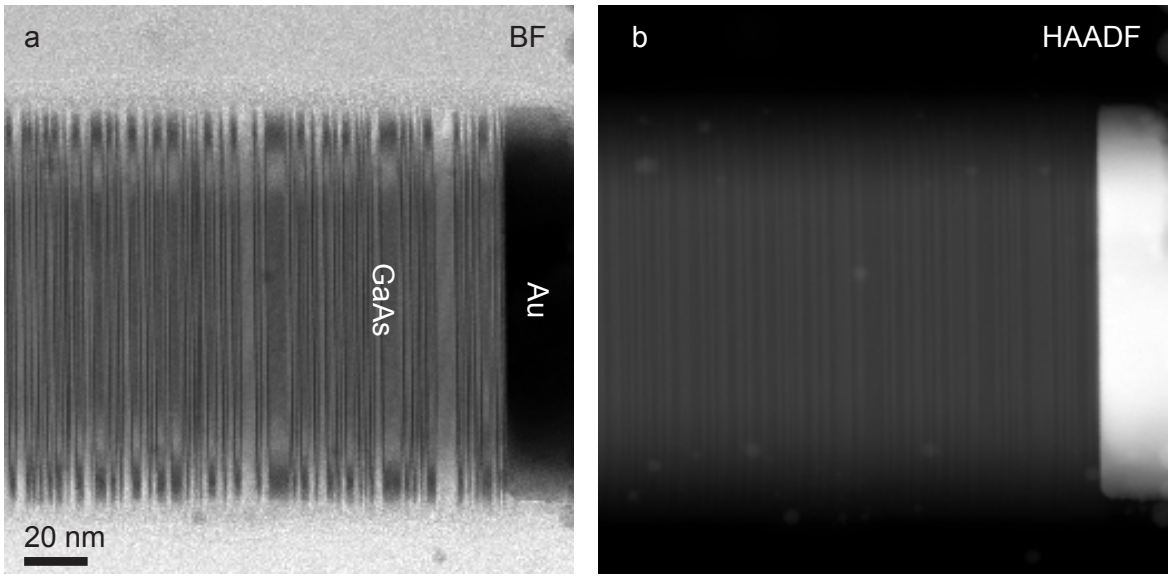

Figure 1.2: **BF and HAADF images of a Au-GaAs nanowire heterojunction.** Simultaneously-acquired BF (a) and HAADF (b) STEM images of a GaAs nanowire with an intruded gold contact. The zincblende twinning defects of the nanowire are easily visible in the bright-field STEM image. In the HAADF images, the hexagonal cross-section and the high-Z of the gold contact provide provide the dominant contrast.

A gallium arsenide nanowire with an intruded gold contact provides an excellent demonstration of contrast given by scattered electrons of different angles[5]. Immediately the nomenclature "bright-field" and "dark-field" becomes obvious: The thin (electron-transparent) silicon nitride membrane scatters few electrons and is thus appears bright in the BF image and dark in the HAADF image. The vertical striations within the GaAs portion of the nanowire, visible in both images, are the result of twinning boundaries in the zincblende crystal structure. However these crystal defects are starkly visible in the BF image, and

only barely visible in the HAADF image, demonstrating that BF is dominated by phase contrast. The HAADF image (Fig. 1.2 b) provides an excellent example of the simultaneous Z and thickness contrast of HAADF. The GaAs nanowire has a nearly-perfect hexagonal cross section, and since one of its faces is flat against the silicon nitride membrane, at the top and bottom of the image its thickness decreases linearly to zero. The change in thickness within the gallium arsenide (constant Z) is readily apparent in HAADF, but completely invisible in the BF image. Moving along the central axis of the nanowire, the thickness is constant, but a huge change in Z from the GaAs to the gold segments is easily visible. The gold appears bright because the atomic charge of the gold (79) is significantly higher than gallium (31) or arsenic (33).

A large advantage of STEM over TEM is interpretation of contrast within an image. In high-resolution TEM, the contrast transfer function (CTF) oscillates in sign as spatial frequencies become larger[3, 2]. Thus high-frequency (high-resolution) spatial information, while technically resolvable, may be practically useless. In practice, this means that interpretation of a TEM image can be difficult: Atomic spacings in a gold nanoparticle may be easily visible, but bright contrast could correlate to an atomic plane, or a lack of one. The CTF of a STEM is single-signed and does not oscillate, and thus it will always be known with certainty that in a HAADF image (for example) a bright column of atoms reflects the true position of the atoms.

Another advantage of STEM is the large suite of accessory instruments that have been developed for STEM. The STEM lends itself to auxiliary instrumentation since the probe size is so small, and thus the sample is illuminated with a point of electrons whose position is well-known. Accessory instruments are often of considerable cost and complexity, and a fully-equipped STEM may have extra instrumentation that easily exceeds the cost of the microscope itself. A common add-on is energy-dispersive spectroscopy (EDS), where an x-ray detector collects photons (keV range) emitted by inner-shell electrons returning to their ground state, after being excited by primary beam electrons. EDS is a powerful and easy-to-use tool which allows for elemental identification and quantification in a wide variety of

materials, although it works best in high-Z atoms.

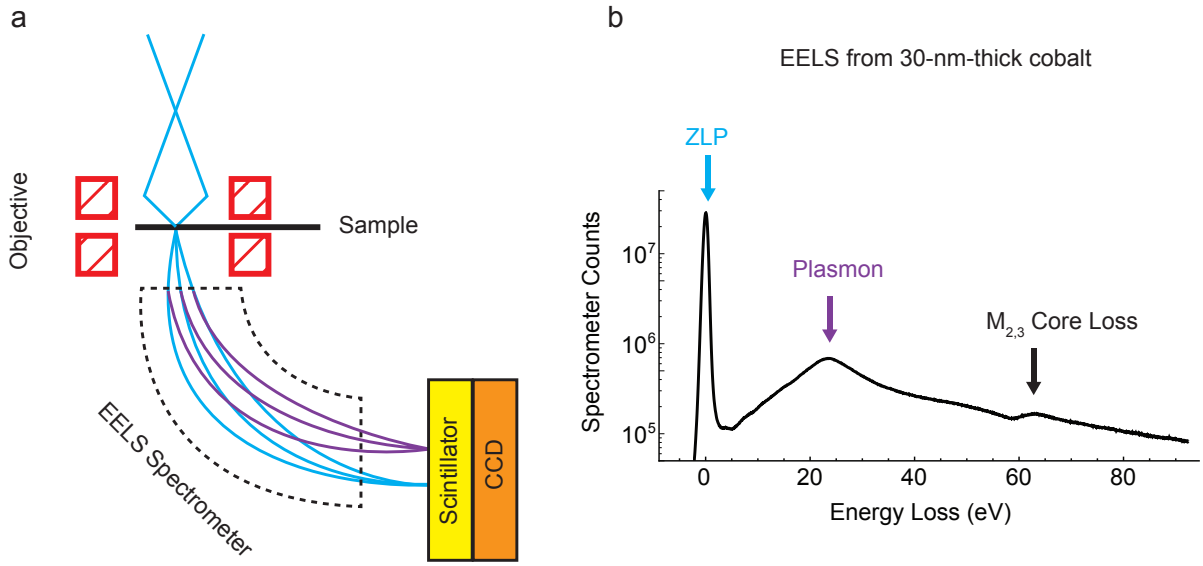

Figure 1.3: **EELS diagram and cobalt spectrum.** A ray diagram (a) depicting how inelastically scattered electrons are collected by an EELS spectrometer. The cyan-colored rays depict unscattered electrons, and the purple-colored electrons have been inelastically scattered, and separated by non-scattered electrons by the magnetic prism. An example spectrum of a 30-nm-thick cobalt film (b), plotted on a semi-log scale, shows the ZLP, first plasmon, and a core-loss peak. The black-labeled electrons form the ZLP, and the purple-labeled electrons have a non-zero energy loss (due to exciting one cobalt plasmon, for example).

Another powerful analytical tool is electron-energy loss spectroscopy (EELS). An EELS spectrometer collects inelastically scattered electrons, disperses them by energy with a magnetic prism, and collects the spectrum with a charge-coupled device (CCD) or complementary metal-oxide semiconductor (CMOS) detector. EELS, as with EDS, is generally used for elemental identification by finding characteristic excitation edges (core-loss) superimposed on the residual background due to low-loss (dielectric) scattering [6].

An EELS spectrometer is located below the conventional annular and circular STEM detectors. Electrons can scatter inelastically from a sample, losing energy to a variety of excitations of varying cross-sections. One of the largest cross-section excitations is the plasmon exciation, which contributes the bulk of the low-loss (dielectric) portion of the spectrum. A plasmon excitation is generally in the $10 - 30$ eV range[7], which is a tiny (.01%) fraction of the primary electron energy. The tiny differences in kinetic energy between unscattered and scattered electrons are resolved by dispersing electrons with a magnetic prism. A system of electromagnetic lenses after the magnetic prism then disperse the electrons onto a scintillator, which is optically coupled to a CCD.

1.2 *In Situ* Sample Fabrication

A significant challenge associated with transmission electron microscopy is the requirement that samples be electron-transparent. At typical STEM accerating voltages, the maximum useful sample thickness[3] is of order 100 nm. Taking a bulk device or crystal and thinning it to electron-transparency is challenging and is the subject of decades of technological innovation. An ultramicrotome can be used to fabricate large, thin cross-section of material. More recently, focused-ion-beam (FIB) technology has been implemented within an SEM, allowing for the extraction of cross sections from a semiconductor wafer. FIB's are an invaluable tool in failure analysis, since an individual nanoscale device can be located within a large wafer, and cross-sectioned individually.

Regan group has developed and honed, over the course of multiple graduate student careers, an in-house fabricated STEM biasing platform[8, 9, 10]. Chips are fabricated in UCLA's cleanrooms, starting with 4" wafers (200 μm 100 Si, 800 nm silicon oxide, 15 nm low-stress stoichiometric silicon nitride). First the back side of the wafers are patterned with optical lithography, using AZ5214 E positive resist, to reveal 0.3 mm square windows. The outer nitride film is removed in the exposed regions using a plasma dry etching recipe, and the photoresist is removed using a resist strip solution. The whole wafer is then immersed in a heated KOH bath for several hours, which anisotropically etches through the silicon

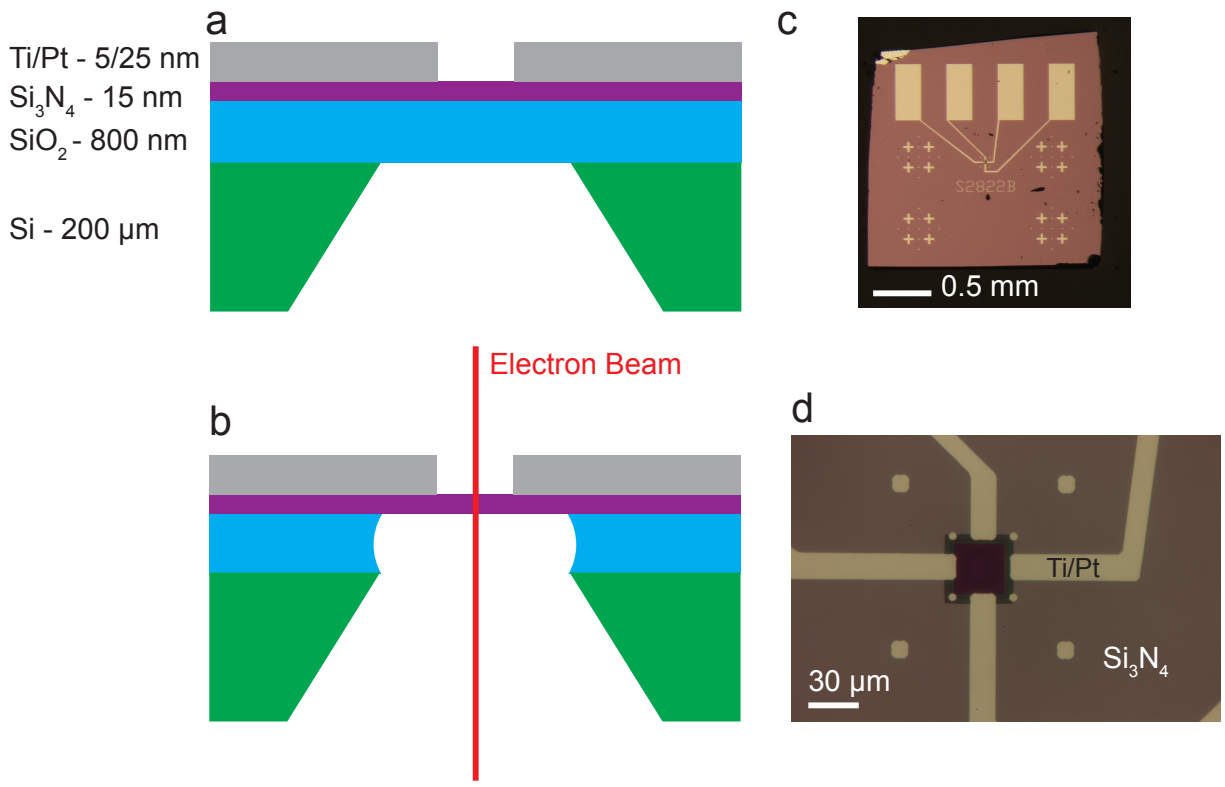

Figure 1.4: **In situ TEM biasing platform.** A cartoon of the TEM chip (a) after KOH etching and metal electrode deposition (a). The 800 nm silicon oxide support film is removed with a hydrofluoric acid vapor etch, making the sample electron-transparent (b). The Ti/Pt electrodes appear bright yellow, and the silicon nitride film appear pink in an optical micrograph (c). A higher-magnification optical micrograph reveals the thinner square window between the electrodes (d).

wafer at an angle of 55° to the surface[8]. Thus on the backside of the wafer, the 0.3 mm windows are reduced to 30 μm when the etch stops at the top silicon oxide layer. Next, the top surface of the wafer is patterned using AZ5214E positive resist to create Ti/Pt electrodes that terminate on the thin window (Fig. 1.4 a,c).

At this point in the fabrication process the biasing chips are versatile, and have served as the foundation for nearly every paper published in the Regan group. Nanostructured thin films can be fabricated easily using electron-beam lithography, nanoparticles or nanowires

can be spun on or transferred mechanically, or two chips can be glued together to make a liquid cell[10]. Once the sample has been fabricated, the silicon oxide support membrane is thinned using hydroflouric acid (HF) vapor. If the device is sensitive to HF, a home-built rig is used to clamp an o-ring over top of the chip, protecting the device from HF vapor. The finished device (Fig. 1.4 b) is at its thinnest 15 nm, and is electron-transparent to (80-300 kV) electrons.

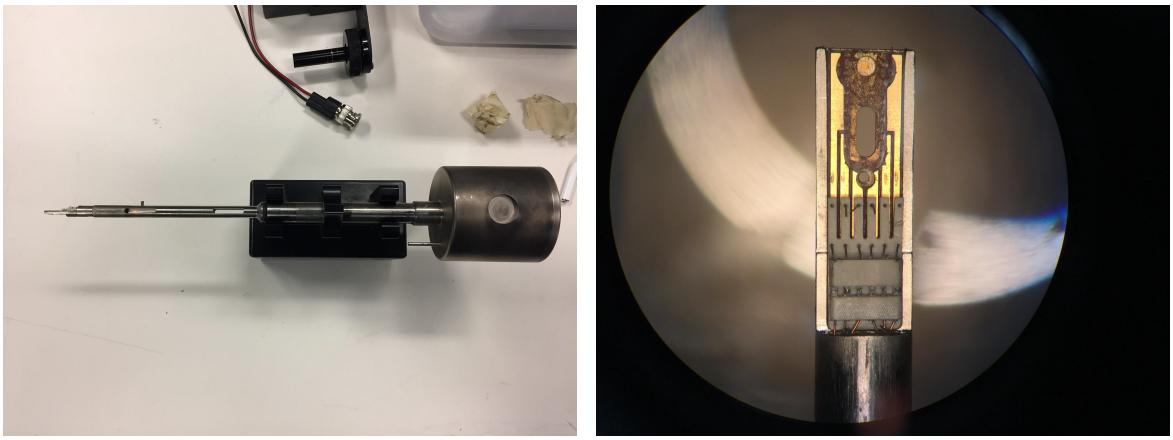

Figure 1.5: **Hummingbird Scientific in situ biasing holder.** Images of the entire Hummingbird Scientific biasing holder (left) and the end of the holder (right) where electrical connections can be made to the sample. Images courtesy of J. Lodico.

Samples are loaded into an in situ biasing holder, manufactured by Hummingbird Scientific (Fig. 1.4 c), and used with the FEI Titan electron microscope. A custom clamp makes electrical contact to the pads on the chip (not shown), and simultaneously lock the chip in place so it will not fall off in the microscope column. Electrical feed-throughs in the holder allow external electronics to manipulate the sample in situ while it is being imaged in the STEM.

CHAPTER 2

High-Resolution STEM EBIC characterization of Surface and Point Defects in Gallium Arsenide Nanowire Heterojunctions

2.1 Introduction to Electron-Beam Induced Current

Electron-beam induced current (EBIC) was first developed shortly after the commercialization of scanning electron microscopes (SEM) in the 1960's[11, 12, 13]. The instrumentation behind EBIC is relatively straightforward: A high-gain current amplifier collects electron-hole pairs that are generated by a primary electron beam. The only hardware required, besides an SEM, are electrical feedthroughs, the current amplifier, and a means of syncing the amplifier with the electron beam position to create an image. Generally the challenging aspect of EBIC is both sample preparation and data interpretation.

Two of the simplest EBIC sample geometries are the planar (Fig. 2.1 a) and orthogonal (Fig. 2.1 b) geometries. A semiconductor p-n heterojunction has a depletion width of size W which separates beam-generated electron-hole pairs. The electrons and holes are then collected by electrodes attached to the sample and constitute the EBIC. Also note that a "p-n" junction is not required: The requirement is a built-in electric field to separate e-h pairs, and this can be made equally well with a Schottky junction.

In the planar geometry (Fig. 2.1 a), the electron beam axis passes through both types of semiconductor, and in the side-on geometry, shown on the right, the electron beam passes through either the p type or the n-type semiconductor. The bread and butter of EBIC is

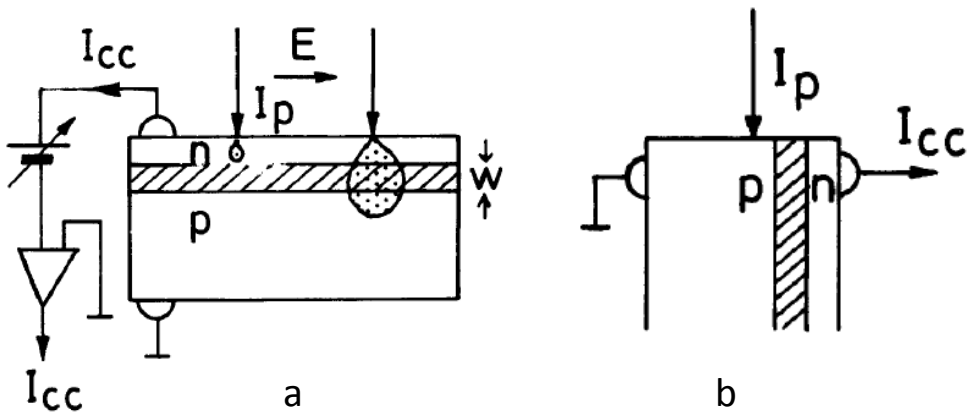

Figure 2.1: **Planar and Orthogonal EBIC geometries**. The planar EBIC geometry (a) and orthogonal (b) geometry of a p-n junction semiconductor sample. In both drawings, the hatched region indicates the depletion region which contains an internal E field. Two electrical connections are made to the n-type and p-type semiconductor to allow for the collection of e-h pairs. A sensitive transimpedance amplifier converts the pA to nA scale EBIC to a sub-10 V signal, which can be synchronized with the electron beam position to form an image. Reproduced from Ref. [14].

to locate electrically-active defects, measure depletion-region widths, and measure minority-carrier diffusion lengths. This chapter focuses on measuring the electrical activity of surface and Frenkel defects in gallium arsenide nanowires, and their impact on the minority-carrier diffusion length of the device.

Electron-hole (e-h) pairs are generated through a variety of mechanisms when a fast electron impacts a semiconductor. Primary electrons generate plasmon excitations, secondary electrons, back-scattered electrons, Auger electrons, and x-rays[14]. For electron energies of (< 100 eV), the plasmon excitatation is dominant[15]. Thus as the primary electron loses

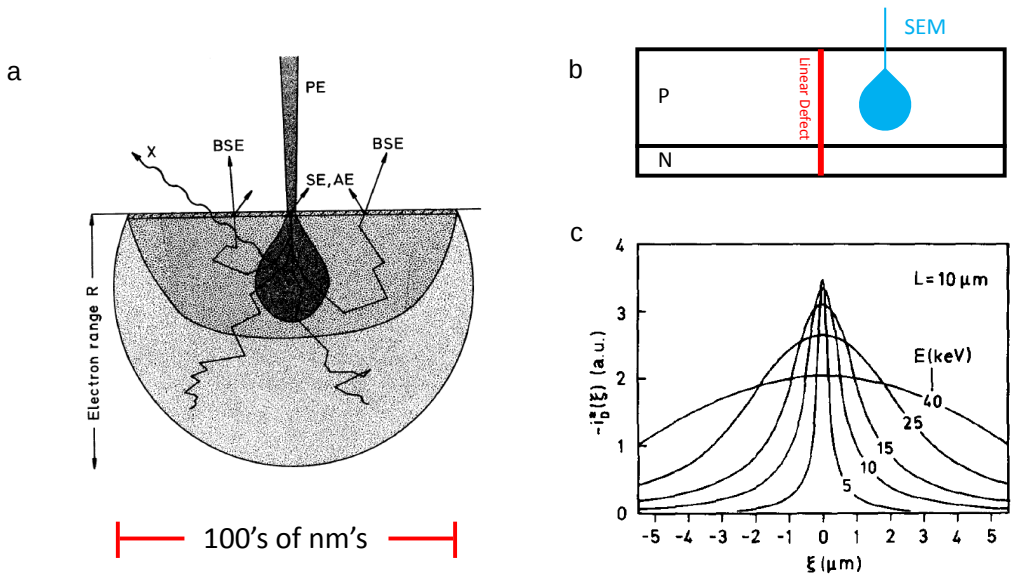

Figure 2.2: **EBIC electronic resolution is limited by e-h generation volume size**. A cartoon of excitations possible when an electron beam impacts a sample, adapted from [14]. The resolution limit of EBIC is limited by the e-h generation volume size, as shown in a theoretical model published by Donolato [17].

energy to lower energy secondary excitations, much of the e-h generation energy will pass through the plasmon stage[7]. A plasmon will decay efficiently into fast e-h pairs, which will quickly lose their excess energy to phonon scattering[7, 16]. However, modeling the pathways (and their relative probabilities) in which a primary SEM electron beam ($1 - 30$ keV) generates e-h pairs is a daunting task. Even basic assumptions, such as the entire primary energy being deposited into the sample, are not necessarily true since back-scattered electrons and x-ray excitations may escape the sample.

Calculating the size of the generation volume is a therefore a daunting task, but is critical to the resolution and interpretation of EBIC images. Similar to an optical point-spread function, the e-h generation volume blurs the electronic structure of a sample, and thus limits the resolution of EBIC images. Much of the basic theory behind contrast in EBIC

was developed by Donolato in a series of papers spanning from the 1970's to the 1980's. In an early paper by Donolato[17], he investigates a simple planar-geometry sample with a vertically-oriented linear defect (Fig. 2.2 b). Without any defects, in the planar geometry, the EBIC will be constant regardless of beam position. This current is defined by Donolato as the background current I_0. If a vertical defect is present in the sample (at beam position $\xi = 0$), the EBIC will be reduced (I^*) due to e-h recombination assisted by the mid-band gap states created by the irregular crystal bonds of the defect. This recombination is visible within the EBIC is a reduction of signal. The contrast profile of the image, defined as $i^* = I^*/I_0$, due to the defect is blurred by the size of the generation volume. As the primary electron energy is increased through 40 keV, the generation increases in size, blurring the delta-function defect to a greater extent. Thus for high-resolution work in SEM-EBIC, lower accelerating voltage is better.

Measurement of primary electron penetration ranges is possible, and was first performed by Everhart and Hoff in silicon[11] for typical SEM primary electron energies of up to 20 keV. Their approximation for electron range in silicon is $R = .0171T^{1.75}$, where R is in micrometers and T is in keV. This function is plotted for typical SEM energies of 1-30 keV (Fig. 2.3 a). At a primary beam energy of 10 keV, the penetration distance of the beam is 1 micron. As an approximation, the width of the e-h generation volume is similar to the penetration depth[17], and thus the shape of the generation volume resembles a pear or bulb. The expression for electron range is extrapolated to higher primary electron energies (Fig.2.3 a), up to the maximum of a typical TEM (300 keV). In a semi-infinite sample, with a primary electron energy of 200 keV, the size of the e-h generation bulb is huge, greater than 50 microns. This generation volume size is orders of magnitude larger than the feature size of modern electronic devices, and thus at first glance STEM EBIC seems ill-equipped to characterize modern devices.

A key difference between samples fabricated for SEM EBIC and STEM EBIC is of course that STEM samples are very thin (< 100 nm) to allow for optimal structural imaging by high-energy electrons. In this regime of thin samples and high-energy electrons, the e-h

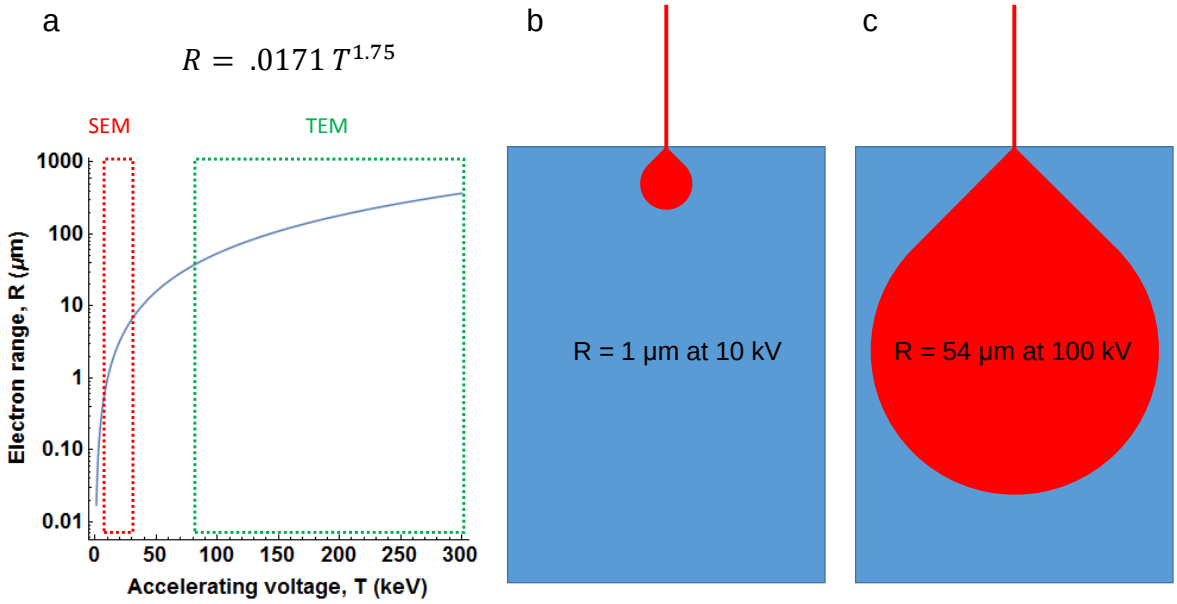

Figure 2.3: **Everhart's model for electron penetration depth in silicon**. Everhart's formula for penetration depth of electrons in silicon is extrapolated to TEM accelerating voltages (a). Cartoons of the generation volume at a typical SEM accelerating voltage (b) and a typical TEM accelerating voltage (c) demonstrate dramatically larger e-h generation volumes at TEM accelerating voltages in semi-infinite samples.

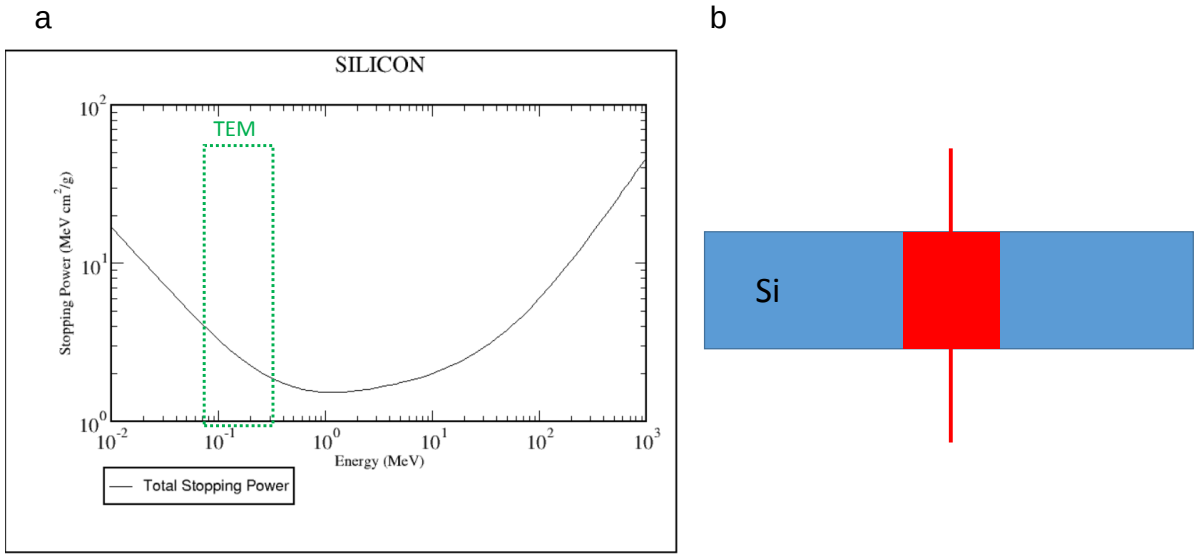

Figure 2.4: **The stopping power of silicon**. The stopping power of silicon is plotted in the TEM accelerating voltage range, according to the NIST ESTAR database (a). A cartoon of the cylindrical generation volume (b), a manifestation of the extremely small fraction of the primary beam energy which is deposited into the sample.

generation volume is the narrow neck of the full e-h generation pear that would apply to a semi-infinite sample at equivalent primary electron energy. The e-h generation volume will be cylindrical[16], with its axis of symmetry equal to the axis of the primary electron beam.

Accurate data of electron stopping power is available in a variety of materials from the National Institute of Standards and Technology (NIST) through the ESTAR database[18]. Data within this database is based on a modified Bethe scattering theory, which is accurate to within a few percent at energies above 100 keV. The stopping power of silicon is plotted through a range of primary electron energies (Fig. 2.4). In the range of typical TEM primary beam energy (80-300 keV), the stopping power decreases steadily, before increasing again at energies over a MeV. In a 100-nm-thick silicon sample, each primary electron on average will lose, on average, 7.6 eV. This energy loss corresponds to 76 ppm of the total energy of

the electron beam, which is the complete opposite situation of SEM EBIC, where all of the primary electron energy is lost.

2.2 Nanowire substrate preparation

GaAs nanowires are grown by Hyunseok Kim and Dingkun Ren (Diana Huffaker Group, UCLA Electrical Engineering Dept.) A semi-insulating GaAs (111)B wafer is used as a growth substrate. First, a 20 nm-thick silicon dioxide film is deposited on the substrate as a growth mask by electron-beam evaporation. Next, nanoholes are patterned on the film by electron beam lithography using a positive e-beam resist (ZEP 520A), followed by reactive ion etching (RIE). The wafer is then diced into square pieces for MOCVD growth, and the resist is removed by wet etching and oxygen plasma etching.

2.3 Nanowire growth parameters

GaAs nanowires are grown using selective-area epitaxy in a vertical MOCVD reactor (Emcore D-75) at 60 Torr, with hydrogen as a carrier gas. Triethylgallium (TEGa), tertiarybutylarsine (TBAs), and diethylzinc (DEZn) are used as precursors for gallium, arsenic, and zinc, respectively (Fig. 2.5). The reactor temperature is first ramped up to 690 °C while flowing 6.1×10^{-5} mol/min of TBAs, and then held for 10 minutes to thermally etch the native oxide. Next, GaAs nanowires are nucleated by flowing 7.5×10^{-7} mol/min of TEGa and 6.1×10^{-5} mol/min of TBAs for 3 min, followed by p-type GaAs growth for 55 minutes while flowing 7.5×10^{-7} mol/min of TEGa, 6.1×10^{-5} mol/min of TBAs, and 3.7×10^{-7} mol/min of DEZn. After the growth, the reactor temperature is cooled down to 300 °C while flowing 6.1×10^{-5} mol/min of TBAs to prevent desorption of arsenic.

Nanowires as-grown are vertically oriented on thick GaAs (111) substrates (Fig. 2.5). More common methods of nanowire growth such as the vapor-liquid-solid (VLS) method[19] produce vast quantities of nanowires, since gold nanoparticles can be spun onto arbitrarily large substrates, and each gold nanoparticle can produce a single nanowire. SAMOVCD, on

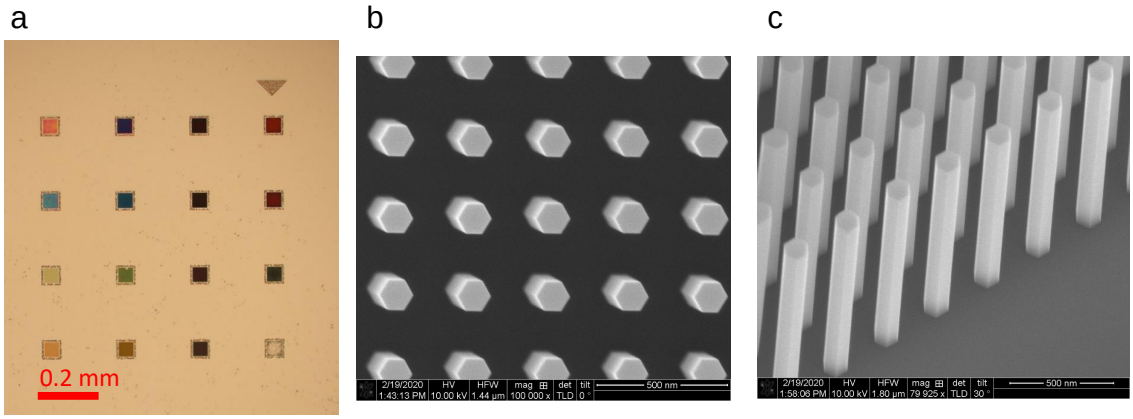

Figure 2.5: **Optical and SEM images of GaAs nanowires on their native growth substrate**. Arrays of GaAs nanowires are grown using SAMOVPE with different diameters and pitches (a). SEM images acquired with the electron beam normal to the substrate (b) and at a 30° angle from the substrate reveal the nearly perfect hexagonal cross section of the nanowires.

the other hand, requires e-beam lithography to open holes in a silicon dioxide film. E-beam lithography is a slow and costly process, and patterning large area of substrate is impractical. The trade-off is that nanowires can be precisely positioned, their width precisely controlled by the diameter of the nanohole, and no risk of metal catalyst atoms incorporating into the semiconductor nanowire[20].

Nanowires are patterned in 16 arrays that vary in both nanowire pitch and nanowire diameter. The row indicates the diameter of the nanoholes, and the column indicates the array pitch. From top to bottom, the nanohole diameters are (40, 50, 70, and 90 nm). From left to right, and array pitch is (1000, 600, 300, and 180 nm). These nanowire arrays act as microscale gratings, and reflect light dramatically differently based on the pitch and diameter of their constituent nanowires. A finer pitch results more light absorption, and thus a darker reflected image. There is also a non-trivial relation between the dominant color of light reflected and the diameter of the nanowires. For example, in the leftmost column, the nanowire diameter is increasing while moving downward in row, yet the colors reflected are pink, blue, yellow and orange. Interestingly, the wavelength of these reflected colors does not increase monotonically with the diameter of the nanowires within the array.

The sparsity of as-grown nanowires also makes transfer to electron-transparent substrates more difficult. A dense forest of nanowires, such as that grown by VLS or metal-assisted etching, can be scraped into a solvent, sonicated, and drop-cast onto a substrate. If nanowires are grown by VLS at a density of, for example, 10 per square micron, even a substrate with an area of one square centimeter would contain one billion nanowires. Nanowires patterned by SAMOCVD are far more sparse, and on the entire substrate (Fig. 2.5), there are only of order 10^5 nanowires available. Conventional drop-casting methods are doomed to fail, since the density of nanowires per volume of fluid will be orders of magnitude too small to ensure a nanowire will land over the electron-transparent region of *in situ* TEM biasing chip.

A simple mechanical transfer method using a sharp tungsten probe tip, while crude, is surprisingly effective. A sharp probe tip is positioned over the correct array, then lowered slowly until the tip makes contact with the desired nanowire array (Fig. 2.6). Some nanowires

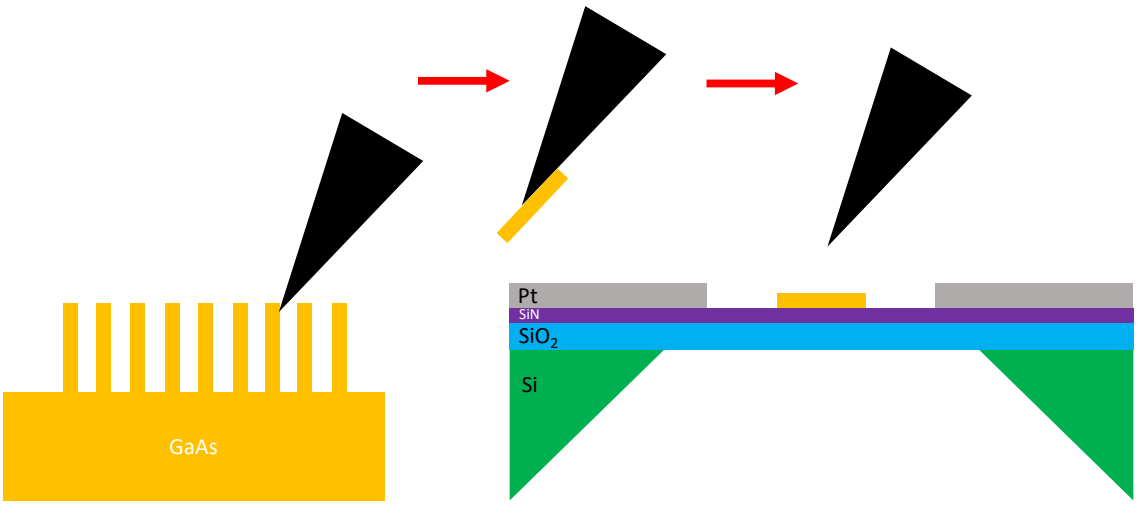

Figure 2.6: **A cartoon of the mechanical transfer process of nanowires to an *in situ* biasing substrate**. A sharpened tungsten probe tip is lowered until contact is made with the nanowires. Some nanowires adhere to the probe tip due to Van der Waals attraction. The probe tip is carefully lowered to make contact with the TEM biasing substrate, where some nanowires then adhere to the thin silicon nitride membrane.

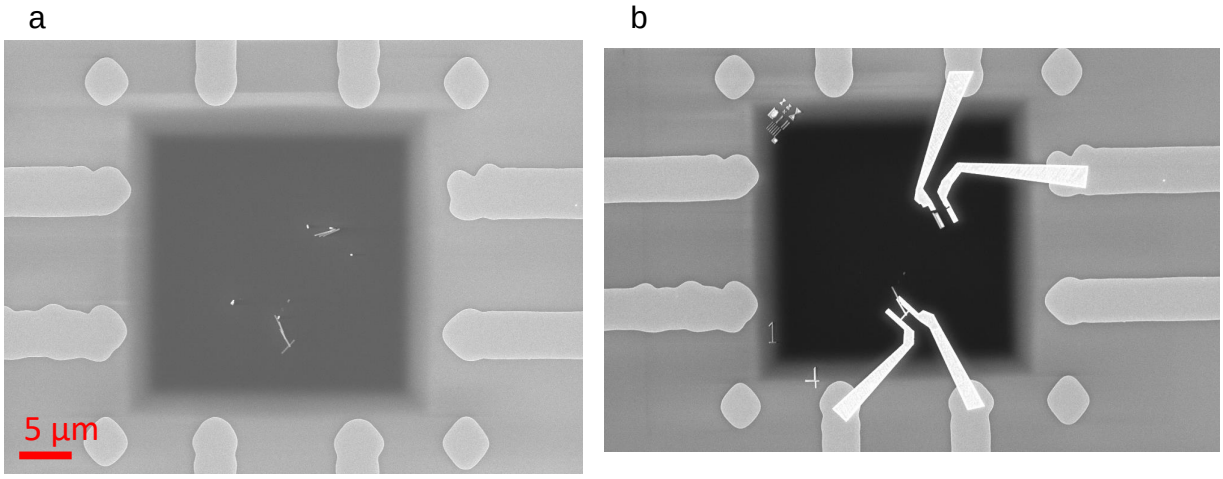

Figure 2.7: **SEM images of nanowire transfer and contact deposition**. SEM images after nanowires have been transferred using the tungsten probe tip (a). Nanowires are randomly oriented on each sample, and must be imaged in SEM to locate their positions. Contacts are defined for each chip using e-beam lithography, and 250 nm of gold is deposited (b).

adhere to the tungsten probe tip due to Van der Waals attraction. The micromanipulator is then positioned over a silicon nitride membrane with its silicon oxide backing film still intact. The probe tip is then very gently lowered until it makes contact with the window, on some occasions leaving nanowires behind on the membrane. It is a testament to the strength of the windows that they can visibly bend due to the probe tip, but do not break.

Although nanowires can be positioned with few-micron accuracy using the micromanipulator, their precise position and orientation are random. To write electrical contacts with electron-beam (e-beam) lithography, first the nanowires must be precisely located with SEM. An image of each TEM biasing chip is acquired at high enough resolution to easily identify the positions of all nanowires on the electron-transparent membrane (Fig. 2.7 a). Next,

each image is overlaid on a drawing of the optical leads in AutoCad, and patterns for gold contacts are drawn to both ends of each nanowire. A custom pattern must be drawn for each chip, because the positions of the nanowires varies randomly from chip-to-chip.

To cover the nanowires completely with metal and ensure a good electrical contact, a thick electrode is needed. A 250-nm-thick gold electrode is needed to completely cover a 130 nm diameter nanowire. To ensure good-quality liftoff of the gold contact, an extra-thick film of e-beam resist (495 PMMA A4) is needed. To achieve this extra-thick film, a slower spin speed of 1000 RPM is used, compared to the standard 4000 RPM for thinner metal films. The thickness of the PMMA resist will be approximately 300 nm using a 1000 RPM spin speed, compared to 200 nm for 4000 RPM spin speed, which is thick enough to ensure good-quality patterns can be written with e-beam lithography.

The PMMA is exposed using e-beam lithography in a Jeol SEM equipped with a Nabity Pattern Generation System (NPGS). Each chip is written with a different, custom pattern to ensure as many nanowires as possible are connected to the large optically-defined platinum leads. The e-beam pattern is aligned by locating four square optically-defined pads and inputting their positions into the NPGS software. To minimize write time, two layers are written at different beam currents. A fine-features layer that makes direct contact to the nanowires is written using a low (5 pA) beam current, and the larger pads which connect the fine features to the optical leads are written with a larger (50 pA) beam current. The total write time is roughly one minute per chip.

The e-beam resist is developed using a solution of 1:3 methylisobutylketone (MIBK) to isopropanol (IPA) for 60 seconds. Immediately before loading into an electron-beam evaporator (CHA), samples are immersed in a diluted 1:10 hydrofluoric acid solution for 60 s to remove native oxides on the GaAs nanowires. Care must be taken to not immerse the patterns for too long, as eventually the PMMA will lift off and the patterns will be destroyed by the acid. Within 10 mins of acid immersion, samples are loaded into the CHA e-beam evaporator, and 250 nm of gold is deposited. Metal liftoff is performed in acetone.

Intruded gold nanowire contacts are formed using a rapid thermal anneal (RTA) at 340° C

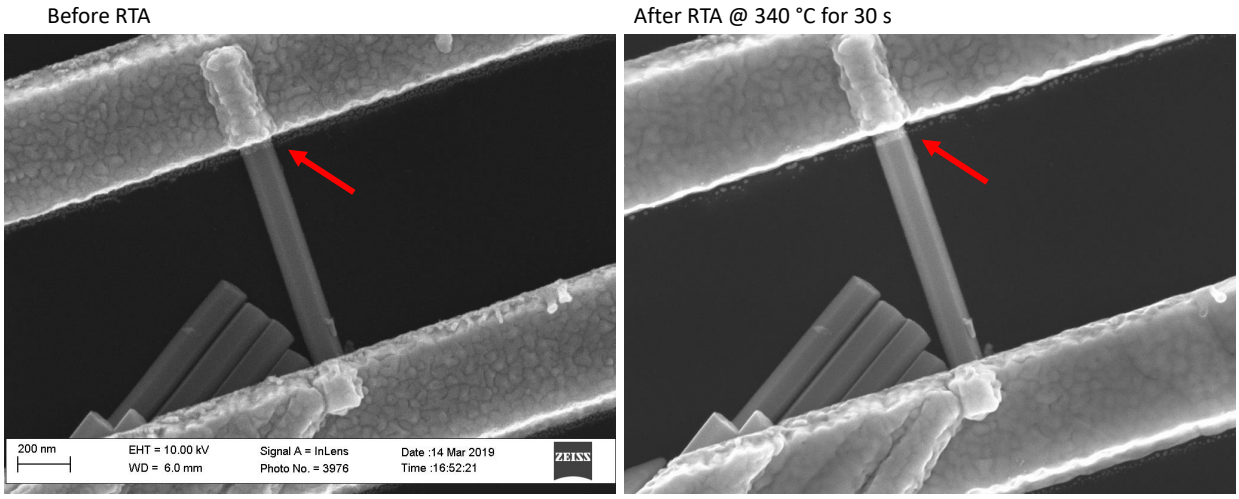

Figure 2.8: **Forming intruded gold nanowire contacts with RTA**. Before (a) and after (a) images of a nanowire device that has been annealed in an RTA at 340° C for 30 s. The red arrow indicates the location of the intruded gold nanowire contact.

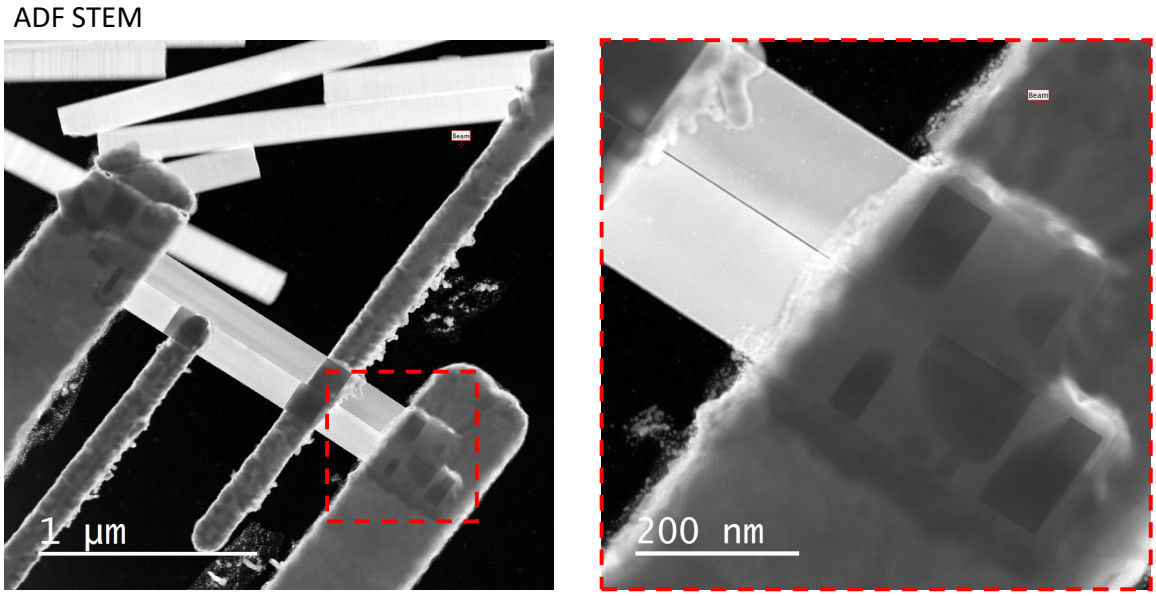

Figure 2.9: **STEM imaging of intruded gold nanowire contacts**. A low-magnification STEM annular dark-field (ADF) image (left) of a device shows 130 nm diameter GaAs nanowires and 250 nm-thick, lithographically-defined gold contacts supported by a 15 nm-thick silicon nitride membrane. The locations of gold intrusion are visible through the contacts in a higher-magnification inset (right).

for 30 s (Fig. 2.8). At elevated temperatures, gallium and arsenic dissolve into the gold contact [21, 22, 23]. The arsenic has a high enough vapor pressure at this temperature that it evaporates, while the gallium mixes with the gold. The intruded contact, which is nearly all gold with a small percentage of gallium, stops at the (111) crystal planes of the nanowire. Since the nanowire axis is aligned along the (111) GaAs crystal direction, these heterojunction nano-contacts are self-aligned perpendicular to the axis of the nanowire (Fig. 2.9).

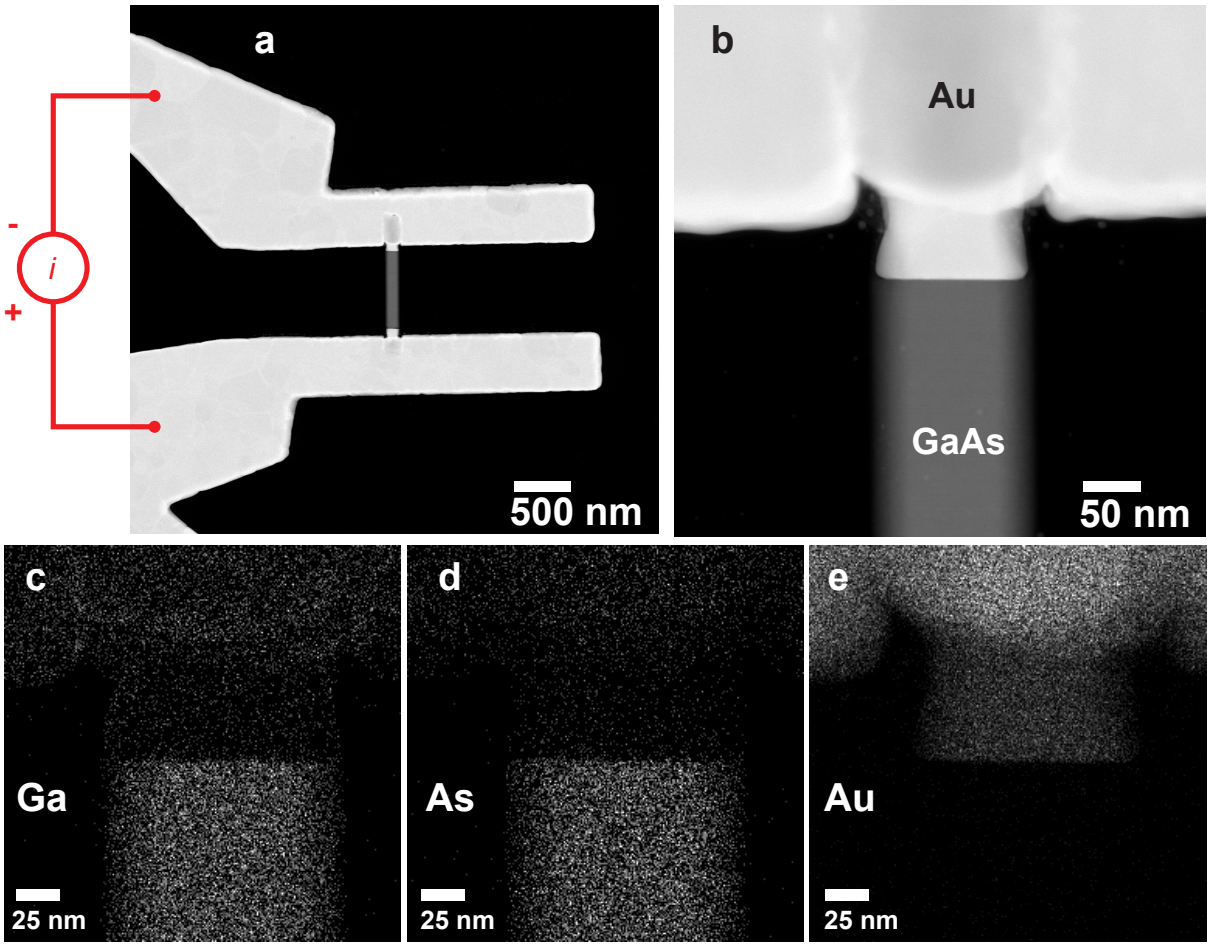

Figure 2.10: **STEM energy-dispersive spectroscopy of an abrupt Au-GaAs nanowire heterojunction**. STEM ADF images of a Au-GaAs nanowire junction taken at a) low and b) high magnification. The electrical connections and the location of the transimpedance amplifier are indicated schematically on (a). The transition from gold to GaAs is extremely abrupt (<2 nm), as verified by STEM energy-dispersive spectroscopy (EDS) maps of the Ga K edge, As K edge, an Au L edge (panels c, d, e).

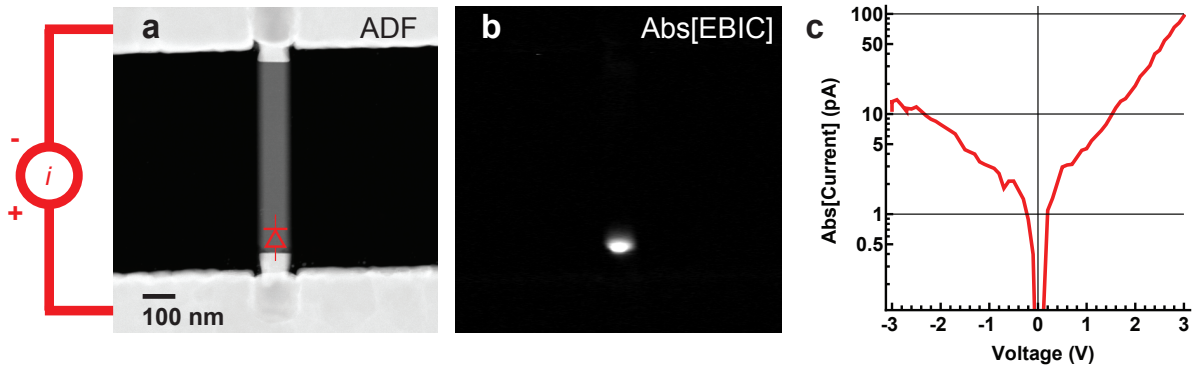

Figure 2.11: **Electrical transport in an individual nanowire diode device.** STEM ADF (a) and corresponding absolute value of STEM EBIC (b) images of a nanowire diode device. Current-voltage data is shown in panel (c), where the bias polarity is the same as the transimpedance amplifier polarity shown on (a). The lower contact generates strong EBIC, while the upper contact generates no EBIC, indicating that the lower contact is a Schottky diode and the upper contact is ohmic. This result agrees with the transport data (c), which is indicative of a single Schottky diode with reverse-bias leakage current.

2.4 Electrical transport data in nanowire devices

Electrical transport data can be correlated to EBIC. In conventional STEM imaging channels our nanowires appear uniform, yet much more EBIC is generated at one contact than the other (Fig. 2.11 b). The cause of this end-to-end EBIC asymmetry is likely due to a gradient in dopant concentration introduced by the growth process. As noted previously, nanowires are grown via a two-step process of nucleation and elongation, and the Zn dopant precursor gas flows only during elongation. If one end of a nanowire is more highly-doped than the other, the end with higher dopant density will make better ohmic contact to the gold. Conversely, the lower-doped end will form a Schottky contact, generating more EBIC since Schottky contacts have a built-in E field. The end-to-end asymmetry in EBIC is reflected in an asymmetric IV profile (Fig. 2.11 c). Forward-bias current is exponentially increasing with voltage (linear increase in semi-log plot), in agreement with the Shockley diode equation. The IV profile is indicative of a single diode with reverse-bias leakage current, not back-

to-back diodes. Coupling information from electrical transport and EBIC, we determine that although both heterojunctions look similar in the ADF image, the lower junction with strong EBIC is a Schottky contact, and the upper junction with no EBIC is an ohmic contact. This image thus provides another example showing how STEM EBIC imaging can reveal information not available to standard methods (e.g. standard STEM, electrical transport).

When multiple nanowires are in parallel (Fig. 2.12 a), EBIC imaging can reveal which ones dominate the transport. This device has five nanowires connected in parallel between the gold contacts. All five have stronger EBIC at one heterojunction than the other (Fig. 2.12 b). Schottky contacts have larger E fields than ohmic contacts, and thus generate stronger EBIC. The Schottky contacts are denoted with diode symbols in Fig. 2.12 a). The polarity of the EBIC flips from positive to negative (white to black) from the bottom contact to the top, since the built-in E field flips direction within the circuit. In this field of view (Fig. 2.12 a), the left-most nanowire generates EBIC at both junctions, and thus allows little current transport since it contains back-to-back diodes. Based on the EBIC images, we expect carrier transport to be dominated by the four right-most nanowires, which have Schottky contacts (strong EBIC) to the lower gold lead, and ohmic connections at the top gold interfaces (no EBIC). Electrical transport can be modeled as an ideal diode in series with a resistor, where the diode represents the Au-GaAs Schottky junction with strong EBIC, and the resistor is the GaAs nanowire resistance:

$$V = V_{diode} + V_{resistor} \tag{2.1}$$

$$V = \eta kT \ln\left[\frac{I}{I_0} + 1\right] + IR \tag{2.2}$$

Here I_0 is the scale current, η is the ideality factor, and R is resistance of the four right-most nanowires in parallel. A resistance of 950 kΩ is found by fitting equation 2.2 to the transport data in Fig. 2.12 c. Assuming uniform dopant density throughout the combined volume of the four nanowires (930 nm length, 130 nm diameter hexagonal cross section), gives a nanowire resistivity of 5 Ω-cm. This measured resistivity is an upper bound; If

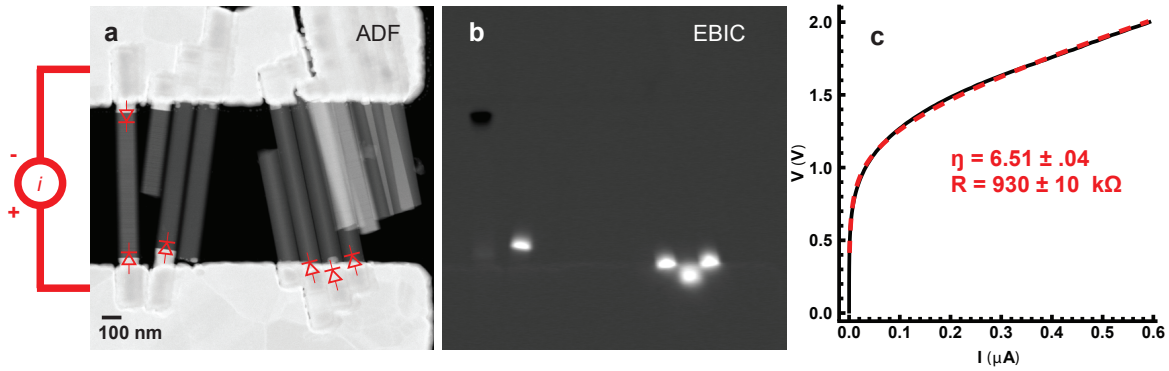

Figure 2.12: **Extracting GaAs nanowire resistivity from multiple devices in parallel.** STEM ADF (a) and corresponding STEM EBIC (b) images of a device with multiple nanowire diode devices in parallel. Current-voltage data is shown in panel (c), with the dashed-red line indicating the best-fit of equation 2.2. The bias polarity in (c) is the same as the transimpedance amplifier polarity shown on (a). Assuming that the four forward-biased nanowires contribute equally to the resistance value extracted from the fit gives an upper bound on the nanowire resistivity.

one nanowire is dominating transport, then the cross-sectional area of R and the measured resistivity will both be a factor of four lower. This maximum resistivity corresponds to a minimum dopant concentration of $\gtrsim 5 \times 10^{15}$ cm^{-3} in bulk GaAs[24].

2.5 Characterization of Electrically-Active Frenkel Defects in GaAs Nanowire Devices with STEM EBIC

Crystal defects in semiconductor devices, whether present at fabrication or introduced later via radiation damage, can dramatically impair device performance[5, 25, 26, 27, 28, 29, 30]. Most common methods for characterizing semiconductor defects have spatial resolution that is crude compared to the feature size in modern microelectronic devices. For example, capacitance-voltage (CV) profiling [31], and deep-level transient spectroscopy (DLTS)[32] can extract defect concentration and energy, respectively, from simple heterojunctions. But the

spatial information provided by these techniques is one dimensional at best. Two dimensional mapping is possible with scanning electron microscope electron-beam induced current (SEM EBIC) imaging, which can locate electrically-active extended (i.e. one- and two-dimensional) defects[33, 34, 27], measure depletion region widths [35], and map minority carrier diffusion lengths[19, 36, 27]. However, the spatial resolution of SEM EBIC imaging is limited by the size of its e-h (electron-hole) generation volume[17]. In a standard, electron-opaque SEM sample, primary (beam) electrons deposit most of their energy near the end of their range. The resulting pear-shaped e-h generation volumes are of order 100 nm on a side[17, 14], which is large compared to feature sizes in many modern devices.

Because a STEM sample is electron-transparent, the corresponding e-h generation volume is the cylindrical, narrow neck of the SEM e-h generation pear[16]. With this much smaller e-h generation volume STEM EBIC imaging has the potential to achieve higher spatial resolution relative to SEM EBIC imaging[37, 38, 39, 40, 41, 42]. Moreover, the higher beam energies accessible with STEM (usually 60–300 keV vs. the 1–30 keV of SEM) span the knock-on damage threshold in semiconductors, which enables a STEM operator to selectively introduce defects in a semiconductor device. The combination of superior spatial resolution and precision modification allows *in situ* STEM EBIC experiments that directly reveal e-h recombination physics in semiconductor nanodevices. In essence, the STEM's focused electron beam serves both as a highly localized source of β-radiation damage, and as an immediate local probe of its effects. This combination allows individual point (i.e. zero-dimensional) defects to be located to within < 1 nm^2.

To produce targets for demonstrating these capabilities, we fabricate heterojunctions in semiconductor nanowires (Fig. 2.13a and Fig. S1), which are model systems for elucidating defect physics[29, 19, 43, 44, 36]. We put Au contacts on 130 nm-diameter p-type GaAs nanowires with electron-beam lithography, and then briefly anneal the devices [23, 22] (see Supplementary Information). At elevated temperatures gallium and arsenic interdiffuse with the gold at the contacts, forming abrupt (< 2 nm) axial Au-GaAs heterojunctions aligned with the (111) GaAs planes (Fig. 2.13b). Since the growth direction of the GaAs nanowires

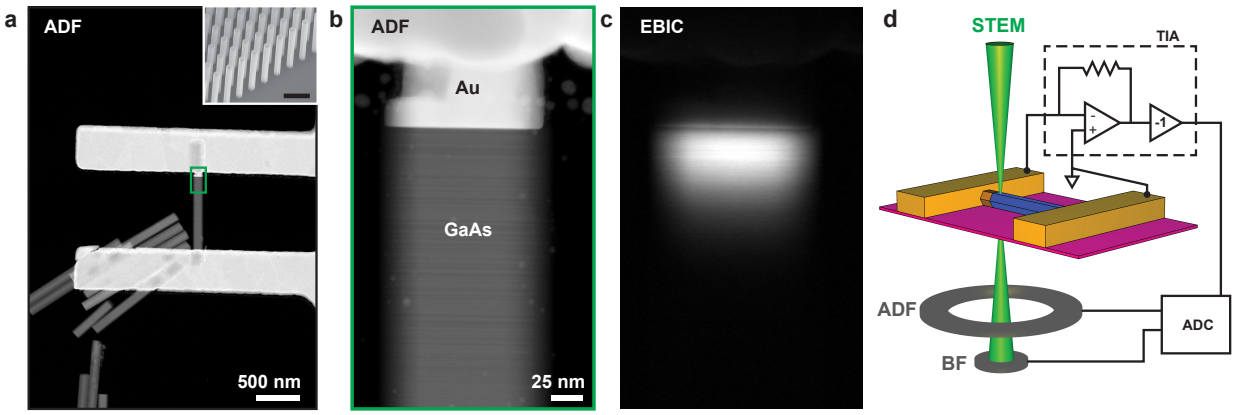

Figure 2.13: **STEM EBIC imaging of a Au-GaAs nanowire heterojunction at 200 kV**. A low-magnification STEM annular dark-field (ADF) image (a) of a device shows 130 nm diameter GaAs nanowires and 250 nm-thick, lithographically-defined gold contacts supported by a 15 nm-thick silicon nitride membrane. An SEM image (a, inset) acquired with 30° stage tilt, shows the nanowires as grown, before transfer to the silicon nitride membrane (scale bar is 500 nm). When the region indicated in green in (a) is imaged at higher-magnification (b), twin boundaries in the GaAs are apparent. An EBIC image (c), acquired simultaneously with (b), reveals the e-h separation that occurs near the Au-GaAs heterojunction. The electrical connections and the locations of the TIA, STEM detectors (ADF,BF), and analog-to-digial converter (ADC) are indicated on a cartoon (d).

is along the [111] crystalline direction, these heterojunctions are self-aligned perpendicular to the nanowire axis. Striations in the GaAs nanowire (Fig. 2.13b) indicate twin boundaries within the zincblende crystal

Connecting a transimpedance amplifier to a device (Fig. 2.13a) allows us to generate a STEM EBIC image simultaneously with every STEM annular dark-field (ADF) image [37, 41, 42]. The contrast mechanisms generating the two types of images are entirely different, and thus the images provide complementary information. The ADF image (Fig. 2.13b) provides information only about the device's physical structure (e.g. composition and crystal lattice orientation), while the EBIC image (Fig. 2.13c) also reveals the device's electronic structure, in this case the CCE, the size of the space-charge region, and the minority carrier diffusion length.

We understand the EBIC signal as being generated as follows. Within some generation volume surrounding the path of the primary electrons through the sample, the STEM electron beam creates e-h pairs, either directly via primary excitation of the GaAs and plasmon decay[16], or indirectly via secondary electrons produced by primaries (in either the GaAs or the Au). Electrons in the conduction band, which are the minority carriers in these p-doped nanowires, then diffuse some distance, parametrized by the minority carrier diffusion length, before recombining probabilistically. Electrons that happen to diffuse to the space-charge region near the Au-GaAs heterojunction can be permanently separated from their holes by the built-in electric field E. The separated charge is collected by the electrodes and constitutes the EBIC. A nanowire heterojunction thus functions as a variable sensitivity beam-electron detector. This sensitivity is equal to the charge-collection efficiency (CCE) of the diode, and is simply the ratio of EBIC to e-h generation rate, G. Although the absolute magnitude of G, and thus CCE, is difficult to quantify precisely due to multiple significant e-h generation mechanisms (plasmon decay, conduction-electron excitation, and core-loss excitations[14]), in our experiments relative changes in the CCE can be precisely measured since our primary beam current, and thus the e-h generation rate per volume, can be kept constant. A detector's relative CCE, proportional to EBIC, varies spatially

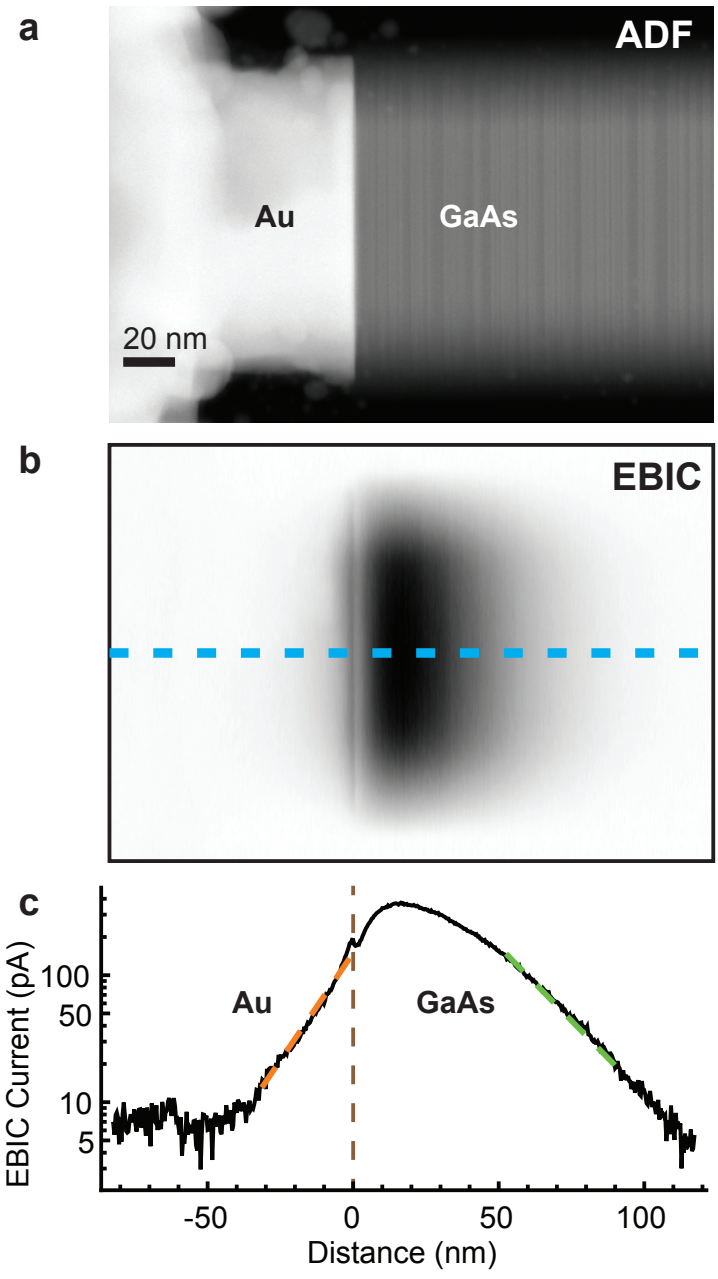

Figure 2.14: **Extraction of minority-carrier diffusion length at 200 kV accelerating potential**. A STEM ADF image (a) of a device and simultaneously-acquired EBIC image (b) are acquired at 200 kV accelerating potential. An EBIC line profile (c) is extracted from the data along the dashed blue line in (b). The EBIC decay length (dashed-orange line) of $R = 12.8 \pm 0.2$ nm within the gold indicates the size of the e-h generation volume. Far from the interface (> 50 nm), within the gallium arsenide, the EBIC decay length (dashed-green line) of $L = 19.9 \pm 0.1$ nm is equal to the minority-carrier diffusion length.

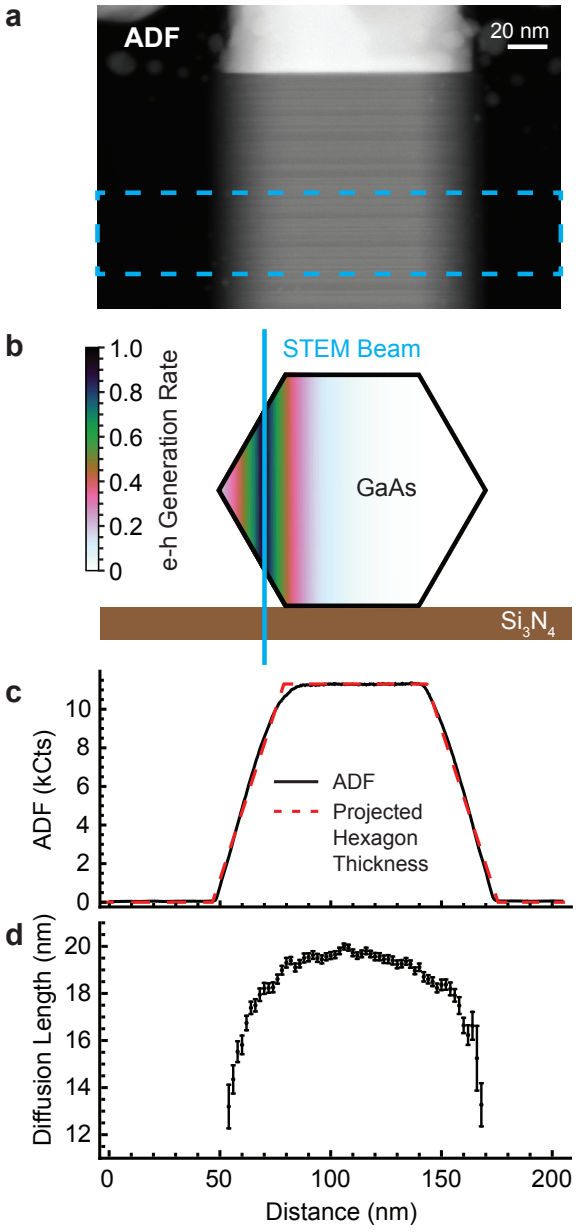

Figure 2.15: **High-resolution mapping of the minority-carrier diffusion length at 200 kV accelerating potential**. The same data shown in Fig. 2.14 (a) is rotated 90° (a) to align the Schottky interface with the horizontal axis. A slice of the cylindrical e-h generation volume is overlaid on the nanowire cross-section (b), with a radial decay length equal to R measured in Fig. 2.14 c. ADF data (c), which is approximately proportional to sample thickness, is summed vertically over the dashed-blue ROI in (a). The cross-section of the nanowire is found to be a nearly perfect hexagon, since a fit of the projected thickness of a mathematically-perfect hexagon (dashed-red line in c) agrees well with ADF data. The minority-carrier diffusion length is mapped across the hexagonal nanowire (d), and decreases dramatically near the nanowire's narrow edges due to increased surface recombination. All panels are aligned horizontally on the same distance axis.

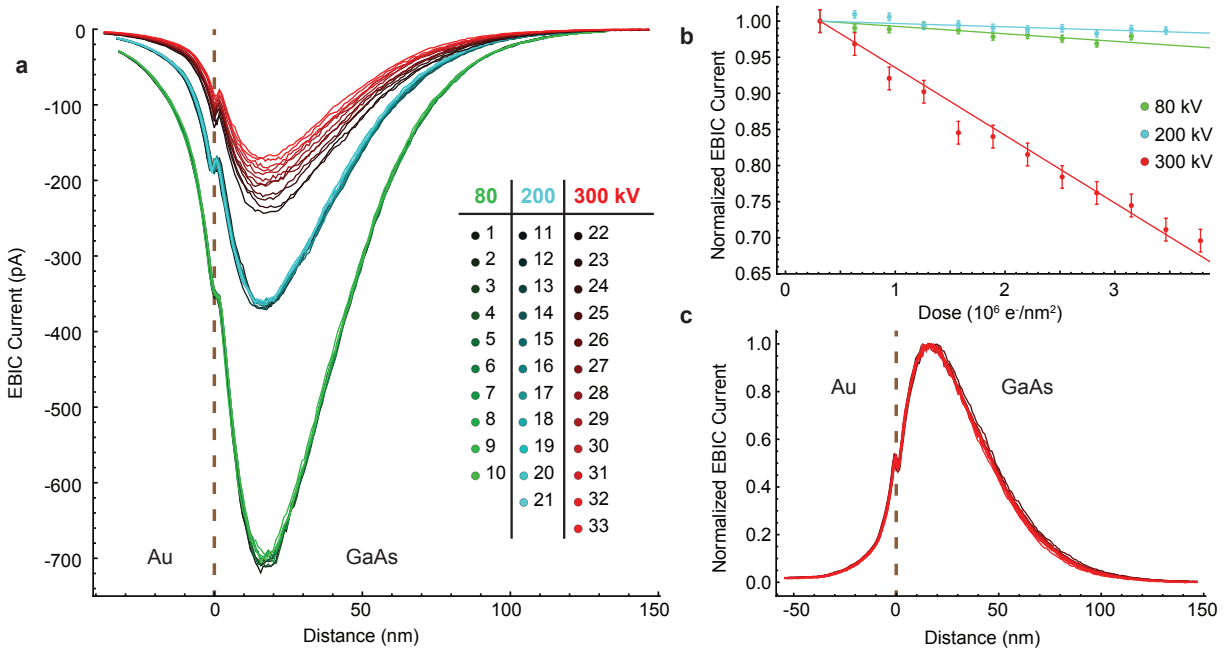

Figure 2.16: **STEM EBIC at 80, 200, and 300 kV accelerating voltage**. Line profiles (a) show the effect of repeated imaging of a device (shown in Fig. 2.17) at 80 kV (green), 200 kV (cyan) and 300 kV (red). Line profiles are extracted from the cyan boxes shown in Fig. 2.17 a. Only the 300 kV curves show a significant decrease in the EBIC with repeated imaging. Plotting the profile minima, normalized relative to their initial values, versus dose shows (b) a linear dose effect at 300 kV and insignificant effects at 80 and 200 kV. At 300 kV the maximum EBIC decreases by $\sim 3\%$ per image. Error bars on the 80, 200 and 300 kV data series are determined by setting the reduced $\chi^2 = 1$ for the linear fits. Normalizing the profiles of the 300 kV data series by the minimum value of each (c) shows that only the amplitude of the EBIC line profile changes, not the shape.

across the device according to three size scales: the e-h generation volume, the minority-carrier diffusion length, and the size of the space-charge region. An EBIC image can provide information on each of them[45].

These length scales collectively determine the shape of the EBIC profile (Fig. 2.14 c). Just as an optical point-spread function limits the resolution of an optical microscope, the size of the e-h generation volume limits the EBIC electronic spatial resolution, and manifests itself clearly in at least two ways. First, a non-zero EBIC is generated when the beam is incident on the Au side of the heterojunction, even though gold is not a semiconductor and has no band gap; secondary electrons generated when the primary beam is incident on the gold travel as far as 50 nm to create e-h pairs in the GaAs. Second, the position of the EBIC profile maximum 20 nm away from the heterojunction interface indicates that, at smaller separations, a sizable fraction of the e-h generation volume is in the Au. The radius of the cylindrical e-h generation volume can be measured by fitting an exponential decay function to EBIC within the gold. A decay length of $R = 12.8 \pm 0.2$ nm is measured (Fig. 2.14 c, dashed-orange line), and the e-h generation function (in cylindrical coordinates) is thus $G(\rho) \propto e^{-\rho/R}$, where ρ is the radial distance from the primary STEM beam. The generation function $G(\rho)$ is normalized to one and plotted when the primary beam is near the edge of the nanowire (Fig. 2.5 b). Notably, the width of the generation function is an upper bound: Gallium arsenide has $\sim 1/3$ the nuclear charge of gold, and its Rutherford scattering cross section is correspondingly ~ 9 times smaller. Fewer multiple-scattering events in the gallium arsenide relative to the gold will only decrease the spatial extent of the generation volume within gallium arsenide.

Far (> 50 nm) from the heterojunction, the EBIC decays exponentially within the GaAs, indicating that minority-carrier diffusion is the dominant transport mechanism in this region. Fitting the measured EBIC current I to $I \propto e^{-x/L}$, where x is the distance from the heterojunction and L is the minority-carrier diffusion length, gives $L = 19.9 \pm 0.1$ nm (Fig. 2.14 c, dashed-green line), where the error bar reflects the statistical uncertainty in a linear least-squares fit. This relatively short diffusion length likely results not from the

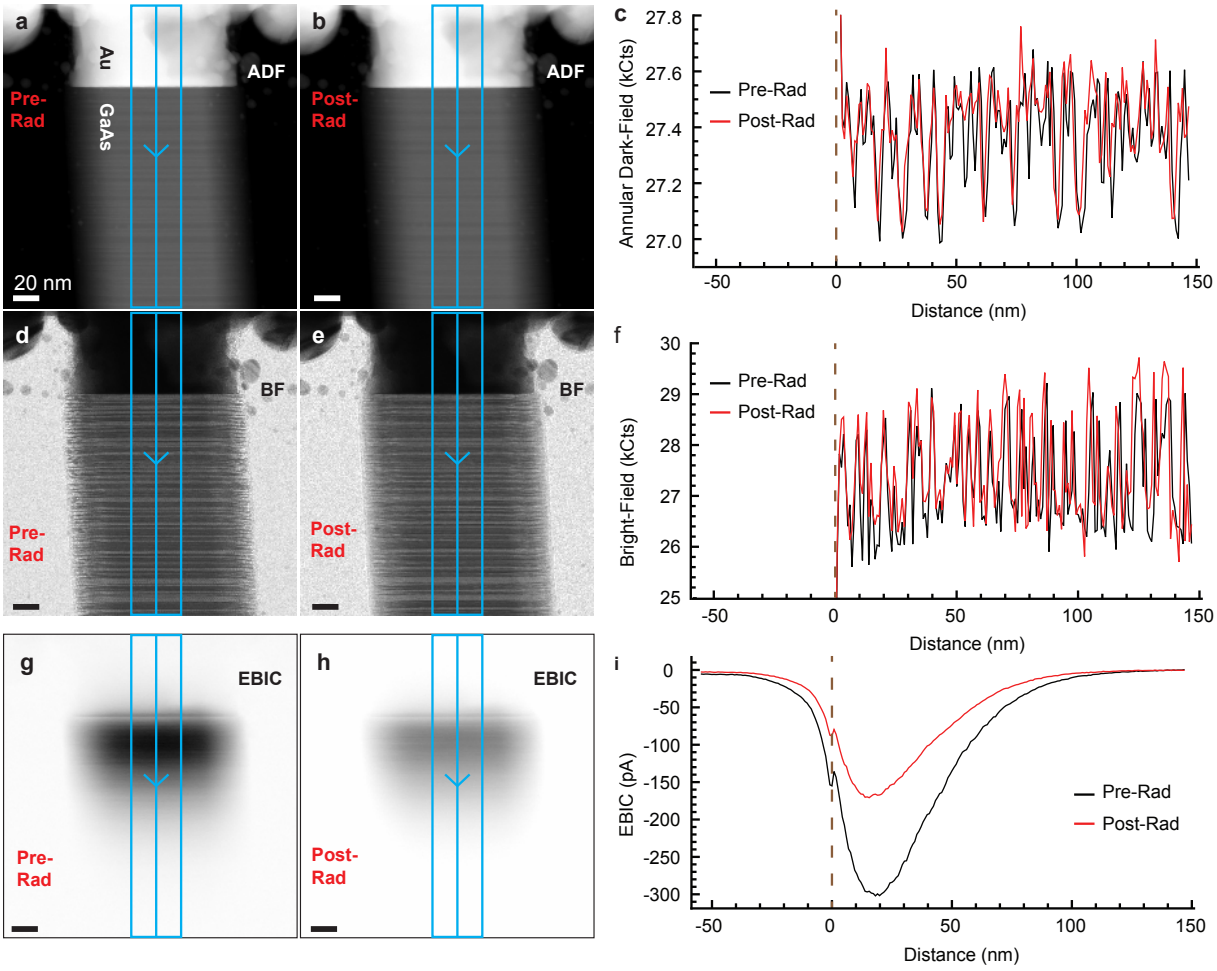

Figure 2.17: **Annular dark-field, bright-field, and EBIC imaging before and after irradiation with 300 kV STEM electrons.** STEM ADF, bright-field (BF), and STEM EBIC images acquired before (a,d,g) and after (b,e,h) a dose of 6.0×10^6 e^-/nm^2 at 300 kV accelerating voltage. The total dose is applied while acquiring the twelve images #22–#33 (Fig. 2.16) and three alignment images (between #21 and #22). Line profiles are extracted (c,f,i) by horizontally averaging data within the blue boxes. A dashed brown line in the line profiles indicates the Au-GaAs interface. Irradiation produces almost no change in the conventional imaging channels (ADF, BF), but a 44% decrease in the maximum EBIC, which highlights the advantage of EBIC over conventional imaging for revealing functional properties such as the CCE.

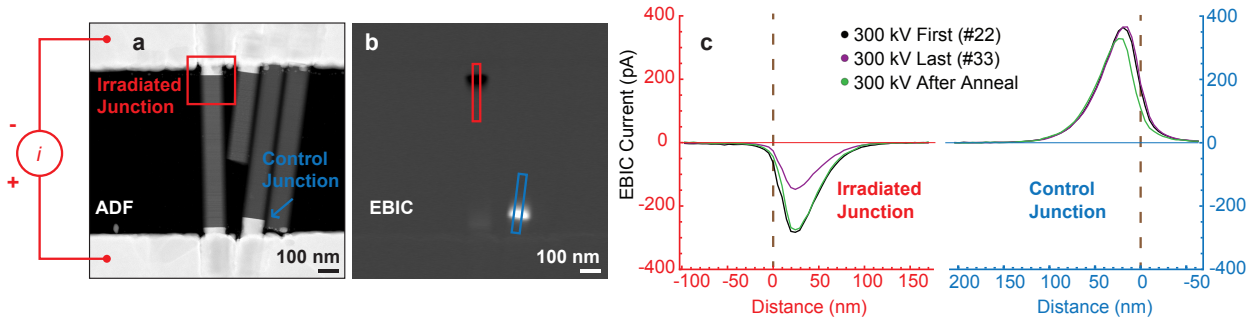

Figure 2.18: **STEM EBIC before and after annealing**. A low-magnification STEM ADF image (a) of the device of Fig. 2.16 shows both the heavily irradiated Au-GaAs heterojunction (red square) and the adjacent control, a heterojunction irradiated less frequently and only at low magnification (cyan arrow). The simultaneously-acquired EBIC image (b) shows that the two heterojunctions have EBICs with opposite signs because of their relative orientations in the circuit. The red and cyan rectangles in (b) indicate the sources of the line profiles in the red and cyan plots of (c). After irradiation with 300 kV electrons the magnitude of the irradiated heterojunction's EBIC is reduced relative to the control. After an anneal the irradiated heterojunction's EBIC recovers.

nanowire's dense zincblende twin boundaries (Fig 2.14 a), but rather surface recombination [36]. This hypothesis can be verified by measuring the minority-carrier diffusion length across the width of the nanowire. We measure the cross-section of the nanowire to be a nearly perfect hexagon, based on the good-quality fit of the ADF signal, which is approximately equal to projected GaAs thickness, to an analytical expression for the projected thickness of a hexagon (Fig. 2.5 c). The diffusion length is measured by fitting an exponential decay function to data within the dashed-blue ROI in (a), which is coincident with the region indicated by the dashed-green line in Fig. 2.14 c. The diffusion length is at its maximum of 20.0 ± 0.1 nm near the central axis of the 130 nm-wide nanowire, and shortens dramatically to 13.2 ± 0.9 nm near the thin edges (Fig. 2.5 d). This reduction is due to a local increase in surface-to-volume ratio, and increased probability of surface-defect recombination, near the thin edges of the nanowire. Thus we determine unambiguously that the minority-carrier recombination length is limited by surface defects within this nanowire device.

Within 50 nm of the interface, the EBIC signal deviates from the straight line on the log-linear plot (Fig. 2.14 c). As mentioned above, this deviation indicates that some of the e-h generation volume is in the Au (Fig 2.5 d), where it contributes less to the EBIC. We might instead expect an EBIC increase because, due to the E-field in the space-charge region near the heterojunction, the charge separation efficiency should increase (perhaps to unity [45]) relative to simple diffusion. However, no increase is evident in Fig. 2.13d. Thus from the EBIC data we can only conclude that the thickness t of the space-charge region is less than the radius $R = 12.8 \pm 0.2$ nm e-h pair generation volume.

To compare damage rates at various accelerating voltages, we image a different device while keeping all other imaging conditions (e.g. the 50 pA STEM beam current, 762 μs pixel dwell time, and 0.87 nm pixel size) constant (Fig. 2.16). Repeated imaging at 80 kV and 200 kV has little effect on the EBIC, but 300 kV imaging markedly reduces the EBIC signal (Fig. 2.16a). The decrease in EBIC magnitude with increasing accelerating potential is expected, as the energy lost per distance for an electron in a solid decreases as the electron's energy increases [46].

As a function of dose, the EBIC, and thus the CCE, decreases linearly at 300 kV (Fig. 2.16b). We attribute the reduction in CCE to knock-on damage that introduces electronically-active vacancy-interstitial (VI) defects, probably on the As sublattice [47]. These defects function as e-h recombination centers, reducing the current that is collected to form the EBIC signal. Energy and momentum conservation dictate that the maximum possible energy transfer from a beam electron to a gallium (mass number $A = 70$) nucleus is 2.7, 7.5, and 12.2 eV for incident electron kinetic energies of 80, 200, and 300 keV, respectively [6]. The maximum energy transfer varies inversely with the mass of the target nucleus, so the numbers for arsenic (A=75) are nearly the same (2.5, 7.0, and 11.4 eV, respectively). Gold (A=197) allows only $70/197 \sim 1/3$ the energy transfer, which is small enough at all of the accelerating voltages used in these experiments that the displacement or knock-on damage in this material is negligible. But the displacement damage threshold energy in GaAs is ~ 10 eV [25, 47, 48, 49] (although with substantial uncertainty — see Ref. [49] and

references within), which leads us to expect an onset of electron beam-induced displacement damage between the accelerating voltages of 200 and 300 kV.

EBIC profiles taken at the damaging 300 kV accelerating voltage overlap closely after they have been normalized relative to their minima (Fig. 2.16c). That the defects introduced do not change the minority-carrier diffusion length L indicates that L is still dominated by surface recombination, and that this length scale is determined by the nanowire cross section as discussed earlier.

Repeated imaging of this device at 300 kV thus causes a substantial reduction in the EBIC (and thus the CCE) of the nanowire junction — the radiation damage destroys this device's ability to effectively separate of e-h pairs. Given the large dose (six million 300 keV electrons per square nanometer) and accompanying efficiency drop, it is remarkable that the device appears undamaged in the standard STEM imaging channels (Figs. 2.17a–f). But while standard STEM imaging is blind to the inserted defects, which have a relatively minor effect on the nanowire's physical structure, EBIC imaging (Figs. 2.17g–i), vividly reveals their outsize impact on the nanowire's electronic structure (namely a 44% reduction of the maximum EBIC).

The device of Figs. 2.16–2.17 is part of a larger circuit (Fig. 2.18). At low magnification a second heterojunction, on an adjacent nanowire but also in the circuit, is visible. The second heterojunction is imaged at lower magnification and less frequently (4.8 nm pixel size, 0.762 μs dwell time), and is thus subjected to less than 1% of the radiation dose of the irradiated junction. This adjacent junction can control for changes that are independent of radiation dose.

To corroborate the role of radiation-induced defects in the observed EBIC reduction, after image #33 of Figs. 2.16–2.17 we anneal the nanowire device in an inert argon atmosphere at 250°C for 30 minutes. Such treatment reduces the density of VI defects within the nanowire, since the elevated temperature makes the beam-induced defects mobile, allowing interstitials and vacancies to meet and annihilate[50, 47]. After the annealing treatment, we image the nanowire heterojunction again (Fig. 2.18). The anneal restores the EBIC to its pre-irradiated

value while changing the measured EBIC in the control junction by only a small amount ($< 10\%$). The post-anneal restoration is consistent with the hypothesis that the radiation-induced CCE reduction is caused by defects — specifically VI defects — that anneal away at high temperature.

The STEM's precise electron beam positioning allows us to observe the effect of selectively dosing just part of the nanowire. In an experiment performed on the Fig. 2.18 device (after the annealing experiment), we irradiate a narrow strip of GaAs that only spans half of the nanowire heterojunction (denoted by dashed green box in Fig. 2.19 a). With 300 kV, a 50 pA beam current, a 0.633 nm pixel size, and a 2.3 ms pixel dwell time, the dose per area per strip image, 1.8×10^6 e^-/nm^2, is $5.5\times$ that of the Fig. 2.16 experiment. As in the experiment of Fig. 2.18, we acquire low dose images before and after the high-dose images for purposes of comparison. (Here a 153 μs dwell time and 1.27 nm pixel size of the two low-dose images contributes only 1.1% of the combined dose from the three strip images.) The difference between the before and after images (Fig. 2.19 d) shows that the localized strip irradiation decreases the CCE across the entire width of the nanowire.

By comparing consecutive EBIC images we can, in some cases, precisely identify the position where an electrically-active defect is inserted. ADF (Fig. 2.19 e1, e2, e3) and EBIC (f1, f2, d3) images are collected simultaneously in the three high-dose strip images. In the (standard) raster pattern used here, the electron beam scans across one row from left to right, and then moves down to scan the next rows in sequence in the same direction. Each strip image shows a dose-induced EBIC decrease, as in Fig. 2.16. EBIC difference images (Fig. 2.19 g1, g2) reveal a sudden drop (8 pA magnitude) in the EBIC that occurs in a single 0.63 nm pixel. We attribute this sudden drop to the insertion of an electrically-active defect during the second strip image, at the pixel indicated by the yellow cross (Fig. 2.19 e2). Notably, since the displaced atom of a VI defect can travel only a few angstroms from its original position at these low energies, and likely in the direction of the electron beam, the yellow cross marks the final location of this single defect [25, 49]. Thus the defect generation volume is much smaller than the e-h generation volume, and EBIC imaging is able to locate

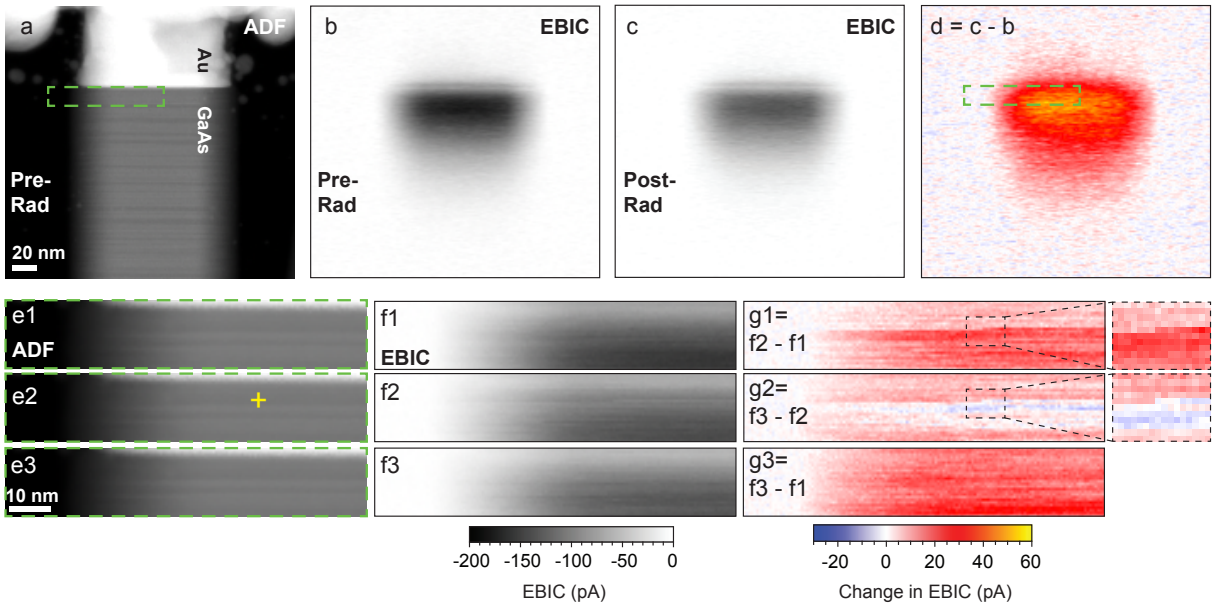

Figure 2.19: **Defect insertion and pinpoint localization with STEM EBIC at 300 kV**. We record the initial state of an Au-GaAs nanowire heterojunction with low-dose (3.0×10^4 e^-/nm^2) ADF STEM (a) and STEM EBIC (b) images acquired simultaneously. We then image the region outlined by the dashed box (a) three times (e1,e2,e3) with a high dose (1.8×10^6 e^-/nm^2 per image). After the three strip images we acquire a second low-dose EBIC image (c). A difference image (d) shows that the EBIC decreases across the entire nanowire, even though the dose was confined to a narrow region on the left side of the nanowire. Dark-field strip images (e1,e2,e3) show no change during irradiation, while the simultaneously-acquired EBIC strip images (f1,f2,f3) show significantly smaller signals. EBIC difference images (g1, g2) reveal a sudden drop in the EBIC magnitude within one 0.63 nm pixel, indicating that a defect was inserted during the second strip image at the location indicated by the yellow cross (e2). Zoom regions (dashed boxes on g1, g2) of 11 pixels $\times$16 pixels (7 nm $\times$10 nm) demonstrate that both the row and the column of the insertion event can be located precisely. A difference image between the first and third strip image (g3) indicates that, as in (d), the electronic impact of the defect is delocalized. The black-white color scale applies to panels (b,c,f), and the blue-yellow color scale applies to panels d and g.

VI insertion events with a much higher precision (< 1 nm) than its electronic resolution of 12.8 ± 0.2 nm.

This defect reduces the EBIC magnitude by 11 pA (a 10% reduction), as determined by comparing the mean EBIC of the 10 pixels before the insertion to the mean EBIC of the 10 pixels after the insertion. As with all of the other STEM-beam induced radiation damage here, this insertion leaves no signature in the conventional ADF imaging. The CCE reduction from this individual defect insertion event is again non-local (as in Fig. 2.19 d), since the difference between the first and third strip images (Fig. 2.19 g3) is uniform.

In summary, STEM EBIC imaging with an electron-beam acceleration potential of 80 or 200 kV maps the CCE of a GaAs nanowire diode without damaging the device. The minority-carrier diffusion length is found to decrease significantly near the thin edges of the nanowire, and is thus limited by surface recombination. Imaging with the acceleration potential increased to 300 kV introduces defects in the nanowire that decrease the diode's CCE. These VI defects can be annealed away to restore the original CCE of the diode. Even though it reduces the nanowire heterojunction's CCE globally, an individual, electrically-active defect inserted at 300 kV can be precisely located by identifying the time of insertion. As these results show, a modern, variable-energy STEM equipped for EBIC imaging is an experimentally potent combination for producing, locating, and characterizing defects in semiconductor devices with high spatial resolution. We expect such a system will be extremely effective at locally determining radiation hardness in microelectronic devices for aerospace applications.

2.6 Direct Measurement of e-h Generation Volume in STEM

EBIC within the gold contact, or the GaAs, can yield information on the spatial extent of the e-h generation function, g (units of current/volume), in each material. In SEM EBIC $g(x, y, z)$ is a pear-shaped 3-dimensional function), and is difficult to measure directly. In STEM EBIC, however, we make important assumptions on the symmetry of g, which

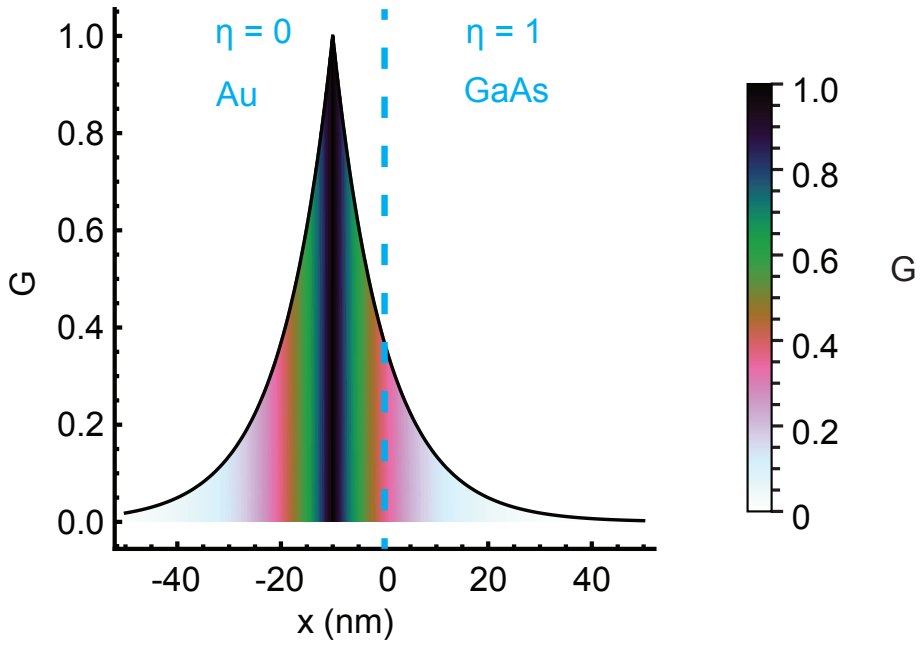

Figure 2.20: **One-dimensional convolution of G and CCE** A one-dimensional approximation of G is plotted along the nanowire axis (x), normalized to one. The electron beam position is -10 nm, the gold contact has a CCE (η) of zero at positions of $x < 0$. At positions of $x > 0$, the CCE is one due to the built-in E field within the GaAs.

greatly simplifies its measurement. Due to thin samples and high electron accelerating voltage, g will be the narrow neck of the pear-shaped generation volume in an SEM [16], and will have cylindrical symmetry around the axis of the primary beam. Thus $g(x, y, z)$ will become $g(\rho)$, where ρ is the radial distance from the primary beam. Note this perfect cylindrical symmetry is valid only when the beam is far from the edges of the nanowire, and far from the heterojunction interface (either of these features will truncate g). The purpose of the following is to calculate the shape of EBIC when g is truncated by the heterojunction interface, and therefore extract the size of g from measured EBIC. EBIC ($I(x, y)$) will be a 2-dimensional convolution of the CCE, $\eta(x, y)$, and $g(\rho)$:

$$I(x, y) = \eta(x, y) * g(\rho) \tag{2.3}$$

The coordinates x and y denote the STEM beam position, where x is parallel to axis of the nanowire, and y is orthogonal to x and the electron beam axis. The heterojunction is located at $x = 0$, and for the purposes of this calculation we will define η as a step function, $\eta = 0$ at $x < 0$ (within the gold) and $\eta = 1$ at $x \geq 0$ (within the GaAs). As an ansatz, g will take the form of $g(\rho) \sim e^{-\rho/R}$, where R is the decay length of the generation function. Note R will be different when the beam is incident on different materials: R_{Au} denotes the size of g within the gold and R_{GaAs} denotes the size of g within the GaAs. To find a simple analytic solution to this problem, we investigate the one-dimensional case, where $\rho \to x$ and $g(x) \sim e^{-|x|/R}$.

$$\begin{aligned} I(x) = \eta(x) * g(x) &\propto \int_{-\infty}^{\infty} \eta(x - x')g(x')dx' \\ &\propto \int_{-\infty}^{x} e^{x'/R_{Au}}dx' + \int_{x}^{\infty} 0 \times e^{x'/R_{Au}}dx' \\ &\propto Re^{x/R_{Au}} \end{aligned} \tag{2.4}$$

Taking the slope of the semi-log plot of EBIC vs. beam position, within the gold, will yield the radius of g within the gold:

$$\frac{d\ln[I(x)]}{dx} = 1/R_{Au} \tag{2.5}$$

This calculation is valid when $x < 0$, or when the beam is within the gold contact. Thus the EBIC is expected to increase exponentially within the gold contact as the beam moves closer to the GaAs (or decay exponentially as the beam moves away from the GaAs), with a decay length R that sets the size of the generation volume.

An equivalent calculation can be performed when $x > 0$, when the beam is within the gallium arsenide:

$$\begin{aligned} I(x) = \eta(x) * g(x) &\propto \int_{-\infty}^{\infty} \eta(x-x')g(x')dx' \\ &\propto \int_{-\infty}^{-x} 0 \times e^{x'/R_{GaAs}}dx' + \int_{-x}^{0} e^{x'/R_{GaAs}}dx' + \int_{0}^{\infty} e^{-x'/R_{GaAs}}dx' \\ &\propto R_{GaAs}(2 - e^{-x/R_{GaAs}}) \end{aligned} \tag{2.6}$$

Taking the logarithm of both sides and differentiating eliminates the constant of proportionality:

$$\begin{aligned} \frac{d\ln[I(x)]}{dx} &= \frac{d\ln[R_{GaAs}(2 - e^{-x/R_{GaAs}})]}{dx} \\ &= \frac{e^{-x/R_{GaAs}}}{R_{GaAs}(2 - e^{-x/R_{GaAs}})} \end{aligned} \tag{2.7}$$

Near the heterojunction, as $x \to 0$ from the positive direction (within the GaAs), this expression becomes simply $d\ln[I(x)]/dx = 1/R_{GaAs}$. Thus, taking the slope of the semi-log plot of EBIC on either immediately adjacent side of the heterojunction can yield either the radius R of g within gold or GaAs.

2.6.1 Validity of the 1-D Approximation

A simplifying approximation was made in the previous calculation, in that the 2-D cylindrical generation volume was transformed into 1-D to find an analytic solution. The full 2D solution

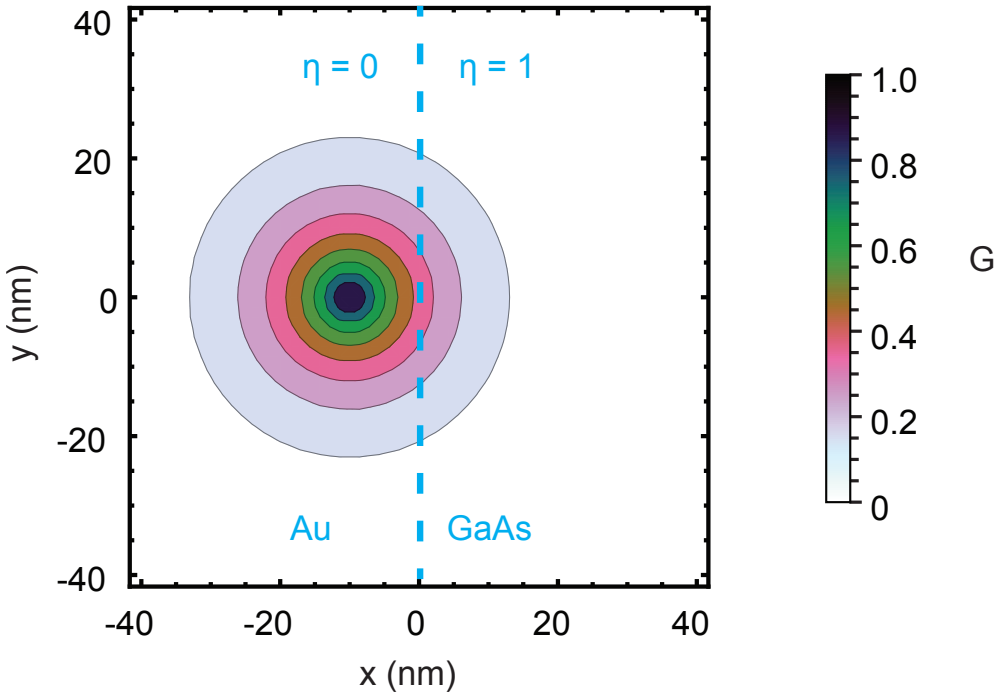

Figure 2.21: **Two-dimensional convolution of g and η.** The cylindrical form of g is plotted when the beam is located at a position of $(x, y) = (-10, 0)$ nm, normalized to one. As in the one-dimensional approximation, the gold contact has a CCE (η) of zero at positions of $x < 0$. At positions of $x > 0$, the CCE is one due to the built-in E field within the GaAs.

takes the form of a cylindrical g convolved with η, which is a step function in Cartesian coordinates (Fig. 2.21). To compare the 1D and 2D models, both must be normalized to the total integrated intensity of g:

$$\begin{aligned} g_{1D}(x) &\propto \frac{e^{-|x|/R}}{\int_{-\infty}^{\infty} e^{-|x|/R} dx} \\ &\propto \frac{e^{-|x|/R}}{2R} \\ g_{2D}(x) &\propto \frac{e^{-\rho/R}}{\int_0^{2\pi}\int_0^{\infty} \rho e^{-\rho/R} d\rho d\theta} \\ &\propto \frac{e^{-\rho/R}}{2\pi R^2} \end{aligned} \tag{2.8}$$

The exact expression for STEM EBIC in a simple heterojunction takes the form of a 2-D convolution in cylindrical coordinates. For $x < 0$:

$$\begin{aligned} I(x,y) &\propto \eta(x,y) * g_{2D}(\rho) \\ &\propto \frac{\int_{-\pi/2}^{\pi/2}\int_{-x/\cos[\theta]}^{\infty} \rho e^{-\rho/R} d\rho d\theta}{2\pi R^2} \\ &\propto \frac{\int_{-\pi/2}^{\pi/2} R(R - x\sec[\theta]) e^{x\sec[\theta]/R} d\theta}{2\pi R^2} \end{aligned} \tag{2.9}$$

For $x > 0$:

$$\begin{aligned} I(x,y) &\propto \eta(x,y) * g_{2D}(\rho) \\ &\propto \frac{\int_{-\pi/2}^{\pi/2}\int_{0}^{\infty} \rho e^{-\rho/R} d\rho d\theta + \int_{\pi/2}^{3\pi/2}\int_{0}^{-x/\cos[\theta]} \rho e^{-\rho/R} d\rho d\theta}{2\pi R^2} \\ &\propto \frac{\pi R^2 + \int_{\pi/2}^{3\pi/2} R^2 + R(x\sec[\theta] - R) e^{x\sec[\theta]/R} d\theta}{2\pi R^2} \end{aligned} \tag{2.10}$$

The integrations of Eqs. 2.9 and 2.10 are difficult to solve analytically, but can be solved numerically (Fig. 2.22, black points). The numerical solution agrees well with the analytic 1-D solution. The best-fit linear slope (Fig. 2.23, dashed-red line on the semi-log plot) of

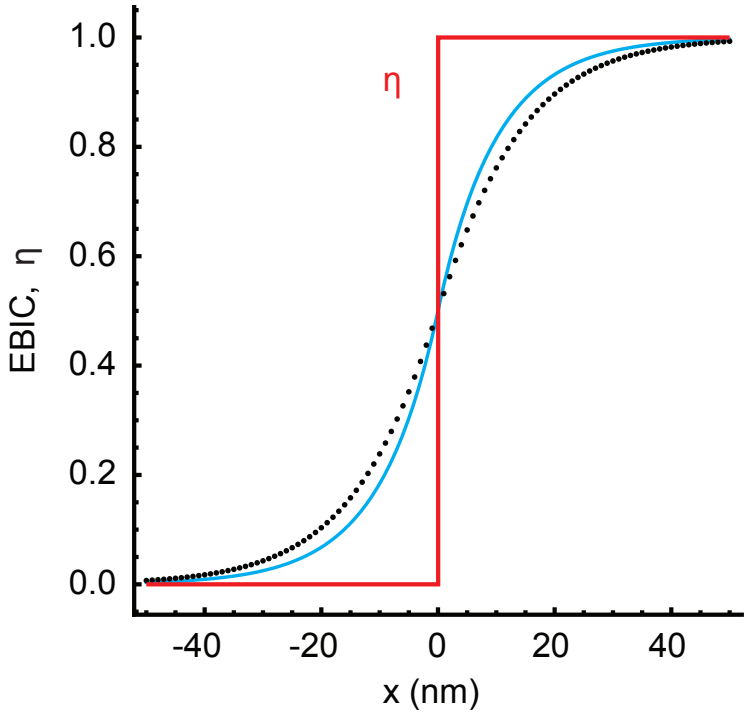

Figure 2.22: **Comparison of 2-D and 1-D convolution of g and η.** The 2-D convolution of g and η is performed numerically (black points) over positive and negative x positions. The 1-D analytic solution (blue line) is overlaid, and is a good qualitative approximation to the 2-D numerical solution. The CCE η (red) has a value of zero at $x < 0$ and a value of 1 at $x \geq 0$.

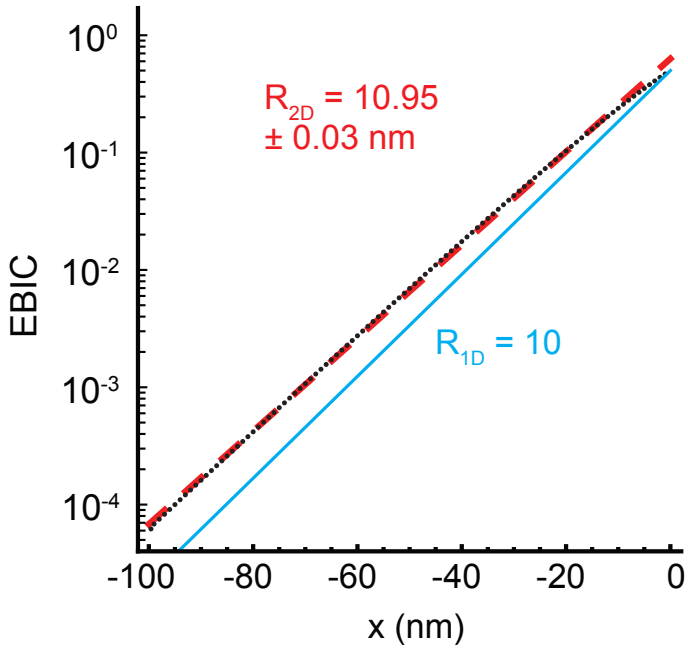

Figure 2.23: **Accuracy of the one-dimensional g approximation.** The 2-D convolution of g and η is performed numerically (black points). This data is well-fit to the function $I(x) \propto e^{x/R_{2D}}$, where $R_{2D} = 10.95 \pm 0.03$ nm. For comparison, the 1-D analytic solution is overlaid (cyan line). This function is also of the form $I(x) = e^{x/R_{1D}}/2$, where $R_{1D} = 10$ nm. The 1D approximation thus agrees with the 2-D numerical solution to within 10%.

the numerical solution of the 2-D convolution is $1/R$ where $R = 10.95 \pm .03$ nm. This slope is within 10% of the analytic value, $R = 10$ nm (solid-blue line on the semi-log plot).

The importance of the e-h generation volume g is made clear: The electronic structure, η, a step function, is blurred by the radius (R) of g. The simple model presented here applies to EBIC near the heterojunction interface ($x \approx 0$), and becomes inaccurate as the beam moves away from the interface and further into the GaAs. In a real device the CCE (η) is only equal to one within the space-charge region[45], and outside of the space-charge region decays exponentially with a length scale equal to the minority-carrier recombination length. The EBIC, in turn, also decays exponentially as the beam moves further from the space-charge region.

2.7 Measurement of Charge-Collection Efficiency with STEM EBIC

The charge-collection efficiency (CCE) of a detector is an important measure of device efficiency. In a previous section, we defined the CCE as the ratio of the collected current (EBIC) to the generated current. The CCE is closely related to the internal quantum efficiency (IQE) of a solar cell, except strictly speaking, the IQE is measured with light as the incident radiation. EBIC is simple to measure, but the generated current is much harder to calculate accurately for the same reasons that the generation volume is difficult to calculate: A variety of e-h generation pathways with unknown relative magnitude.

EBIC data can be acquired easily at three different accelerating voltages (80, 200, 300 keV) within UCLA's Titan STEM. In principle, more accelerating voltage values between these are possible, but in practice each accelerating voltage requires a unique alignment file to ensure the beam optics are aligned to produce a good image. EBIC line profiles extracted from the central axis of the nanowire (Fig. 2.24 a) increase in magnitude as the accelerating voltage decreases, indicating a higher electron stopping power in GaAs with increasing primary beam energy.

The EBIC profiles taken at three different accelerating voltages are normalized to one,

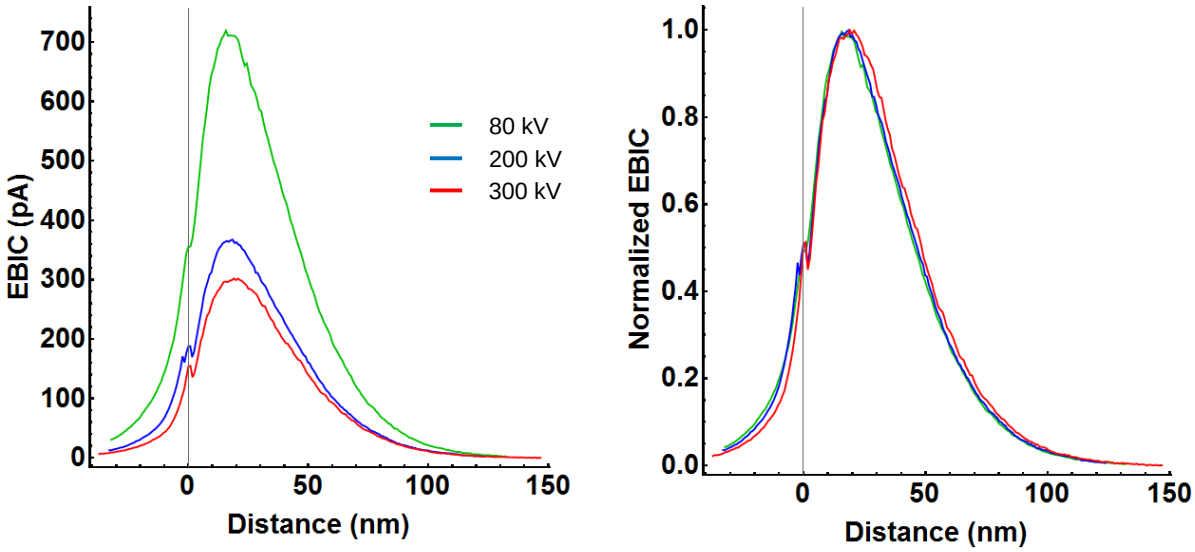

Figure 2.24: **STEM EBIC profiles acquired at 80, 200 and 300 kV**. EBIC profiles down the central axis of the nanowire (left). These EBIC profiles are normalized to one, and overlap closely (right). The close overlap of the profiles confirms the e-h generation volume is cylindrical at all three accelerating voltages.

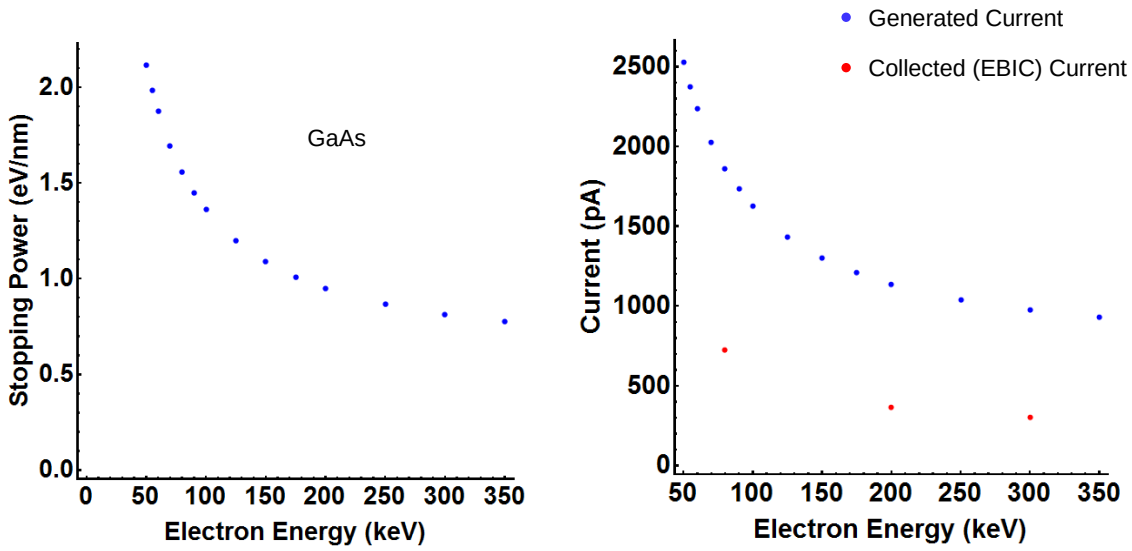

Figure 2.25: **Stopping power of GaAs and predicted e-h pair generation rate**. Stopping power of GaAs is plotted versus accelerating voltage (data from NIST ESTAR database) (left). Stopping power is converted to energy deposited in the nanowire, and the maximum rate of e-h pairs is plotted (blue, right). The actual collected EBIC is shown in red.

and found to overlap closely (Fig. 2.24 b). This is direct evidence that the e-h generation function within these samples is cylindrical. If the generation function lacked cylindrical symmetry, the profiles would change shape with accelerating voltage, and would not overlap so closely.

Stopping power from the NIST ESTAR database is plotted over the range of primary electron energies used within our STEM (Fig. 2.25 a). The data decreases monotonically over this energy range, which agrees with our EBIC data. Ionization energies, i.e. the mean energy required to create an e-h pair, are available in multiple semiconductor materials, including GaAs[14]. In GaAs the ionization energy is 4.6 eV. Using the measured STEM beam current, the stopping power at each accelerating voltage, the GaAs nanowire thickness

of 110 nm, and the ionization energy, it is possible to calculate the generated current at the range of primary beam energies used (Fig. 2.25 b). The EBIC current is roughly less than half of the generated current, and thus the CCE in these devices is less than half.

The CCE can be plotted along different slices of the nanowire diode device. Because the e-h generation volume is cylindrical, the e-h generation rate is proportional to thickness. Taking a slice across the width of the nanowire yields a thickness profile, and thus generation profile, that takes the shape of a projected hexagon (Fig. 2.26 a). EBIC current is plotted on the same axis, and notably has rounded corners instead of the angled corners of the thickness profile. This qualitative difference is reflected quantitatively in the CCE plot. The maximum CCE of nearly 60% is near the central axis of the nanowire. Near the thinner edges of the device, the CCE decreases dramatically to nearly 20%. This decrease is due to surface recombination of the beam-generated e-h pairs. Thus surface recombination not only decreases the minority-carrier diffusion length of the nanowire, but also decreases the CCE.

Along the central axis of the nanowire, the thickness of the GaAs, and thus the generation rate, is constant (Fig. 2.27 a). The CCE is thus directly proportional to the EBIC, as assumed in the previous section on the effect of Frenkel defects within the GaAs nanowires. The maximum CCE of the diode is nearly 60%, approximately 15 nm from the Schottky heterojunction interface. The CCE decreases at closer distances because some of the energy deposited by the primary beam is put into the gold contact, where it does not generate e-h pairs. A more sophisticated model would take this effect into account, because the CCE should be at its maximum immediately adjacent to the interface, where the E field is at its strongest. Far from the heterojunction interface, the CCE (and EBIC) decays at a length scale equal to the minority-carrier diffusion length.

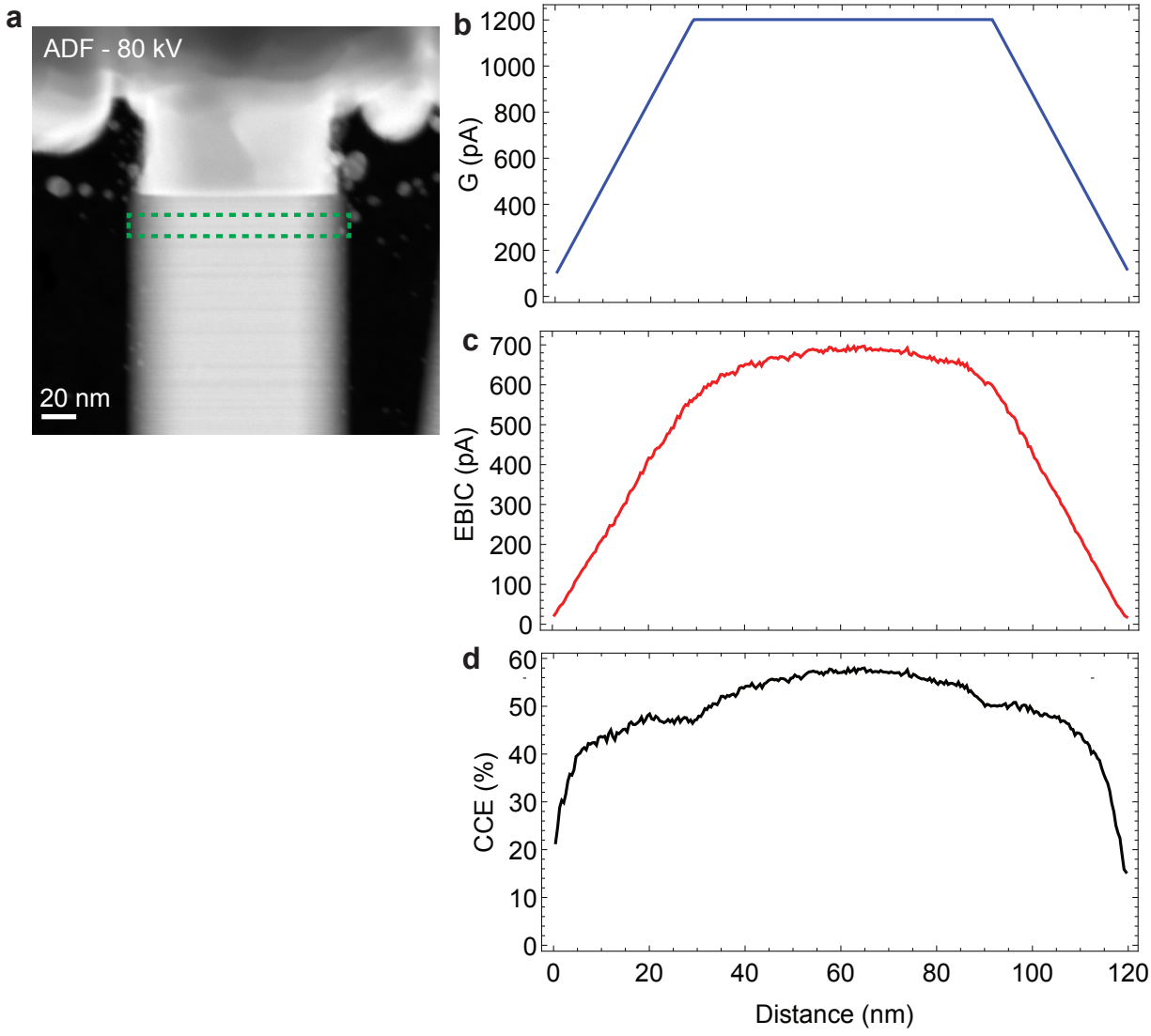

Figure 2.26: **Charge-collection efficiency across the width of the nanowire**. An ADF image (a) shows the GaAs nanowire and its intruded contact. The e-h generation rate (b), measured EBIC (c), and CCE (d) are taken from the dashed-green line in (a).

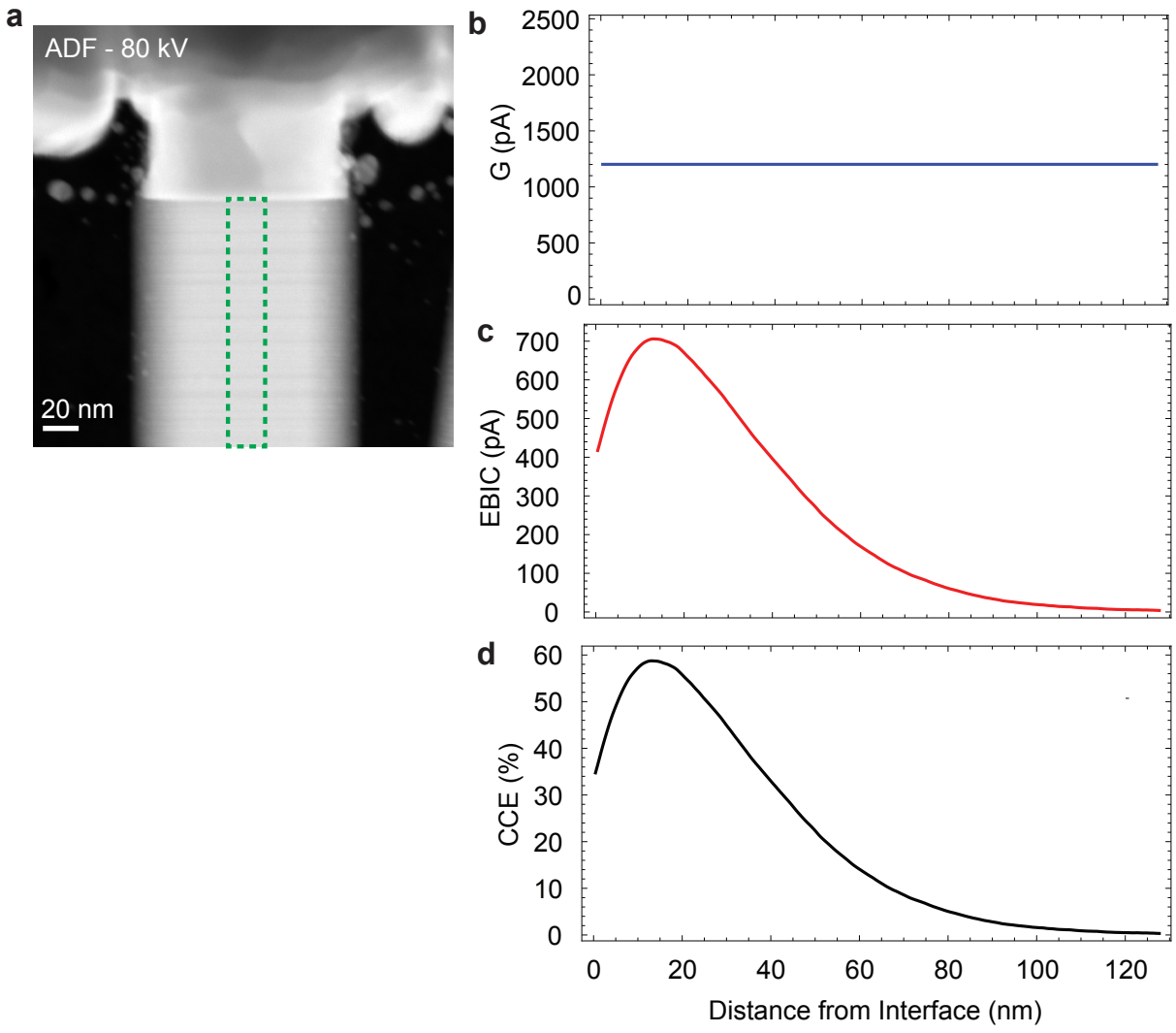

Figure 2.27: **Charge-collection efficiency along the axis of the nanowire**. An ADF image (a) shows the GaAs nanowire and its intruded contact. The e-h generation rate (b), measured EBIC (c), and CCE (d) are taken from the dashed-green line in (a).

2.8 EBIC's structural resolution limit

The physical strucural resolution limit of an EBIC image can surpass the electronic strucural resolution of ~ 10 nm. The reason for this is straightforward: The energy deposited within the sample is proportional to the material thickness which the primary beam passes through, and in a STEM the primary beam is approximately one nanometer in diameter, or even narrower. Manifestations of this effect are apparent in several places within an EBIC image of the nanowire heterojunction (Fig. 2.28). A small hiccup in the EBIC occurs exactly at the sharp Au-GaAs heterojunction interface. The EBIC abruptly increases as the beam moves from the GaAs into the gold, a result of gold's higher atomic charge and increased secondary electron generation rate.

A second feature is less obvious, both in terms of signal processing and also its physical origin. Vertical undulations (perpendicular to the nanowire axis) are faintly visible in both the EBIC image and its corresponding line profile (Fig. 2.28 c). These undulations are more obvious with the use of a high-pass filer, which removes signal that varies slowly with beam position (Fig. 2.28 d). These undulations correlate almost exacly with undulations in a simultaneously-acquired HAADF image. Changes in HAADF singal indicate either changes in thickness, or nuclear charge per volume. The undulations in HAADF are due to twin boundaries in the zincblende gallium arsenide crystal. Twin boundaries should not induce strain (or a change in nuclear charge density) within the nanowire since each orientation of gallium arsenide is close packed, and thus will not induce a change in HAADF. The most likely explanation for these undulations are changes in thickness caused by the twin boundaries, and thus changes in the energy the primary deposits (and the e-h pair geneartion current).

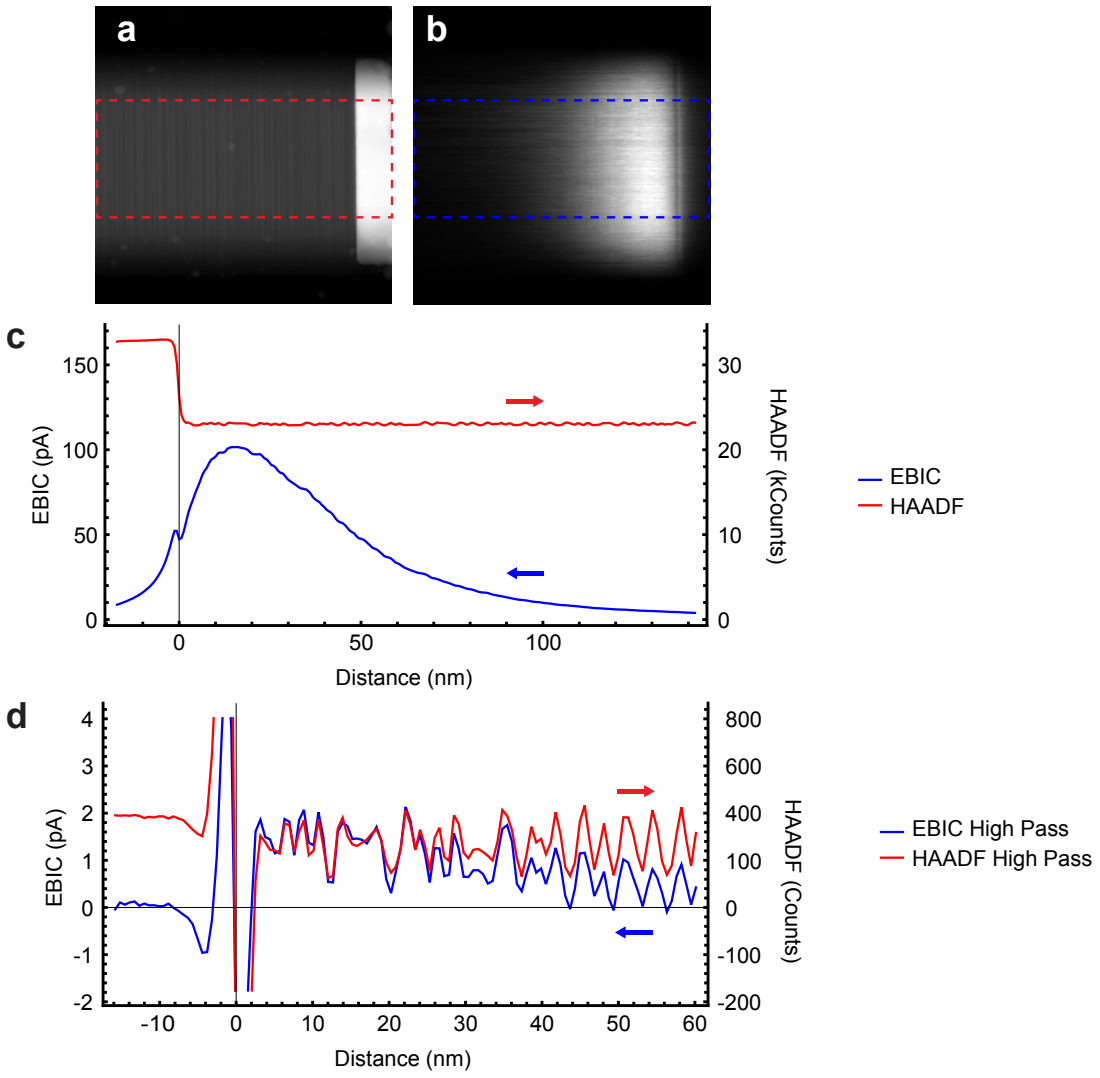

Figure 2.28: **STEM EBIC physical structural resolution**. A nanowire heterojunction device is imaged with HAADF (a) and EBIC (b) modes at 200 kV accelerating voltage. Line profiles are extracted from the dashed-red (a) and dashed-blue (b) boxes and plotted in (c). A step function in the HAADF signal, and a corresponding hiccup of width ~ 3 nm, are due to the gold-GaAs heterojunction interface. Undulations in EBIC, due to the twin boundaries within the GaAs nanowire, are made clear (d) by applying a high-pass frequency filter to the HAADF and EBIC signals. The undulations in both modes overlap closely, thus the STEM EBIC resolution reflects the physical structure of the sample, and is thus equal to the HAADF resolution of ~ 2 nm.

CHAPTER 3

Strain and Temperature Measurement with 4D-STEM and PEET

3.1 Introduction to 4D-STEM

STEM has been used for decades to probe precise regions of a sample, and collect phase and density information. In STEM mode, elastic scattering allows quantized reflections of electrons off a crystal, which in practice are cones of scattering with angle equal to the convergence angle of the STEM beam[3]. This convergent-beam electron diffraction pattern (CBED) contains much crystallographic information that is often thrown away due to computational, data storage, and detector limitations. In conventional STEM, an ADF detector is used which effectively only has one bin for data collection (Fig. 3.1). This scheme allows for phase contrast through a circular bright-field detector, which effectively takes scattering contrast from the center (zero-order) CBED disk. Contrast at higher scattering angles from an ADF of HAADF detector provides a mixture of crystal structure and inelastic (atomic charge) contrast, and it is difficult to totally separate those two contributions.

4D-STEM, a technique in which the CBED pattern is projected on a fast detector and saved at each probe position, has become possible over the past decade due to improvements in detector and computer speed[51]. The "4D" in 4D-STEM comes from the 4-D data cube of information that is acquired: Two dimensions for real space (beam-position), and two more dimensions for reciprocal space (detector pixel location). A single 4D-STEM image can be of order 100 GB in size or larger, and a dataset can span into the TB regime. Although these datasets are enormous and thus challenging to analyze, the end product is extremely sparse.

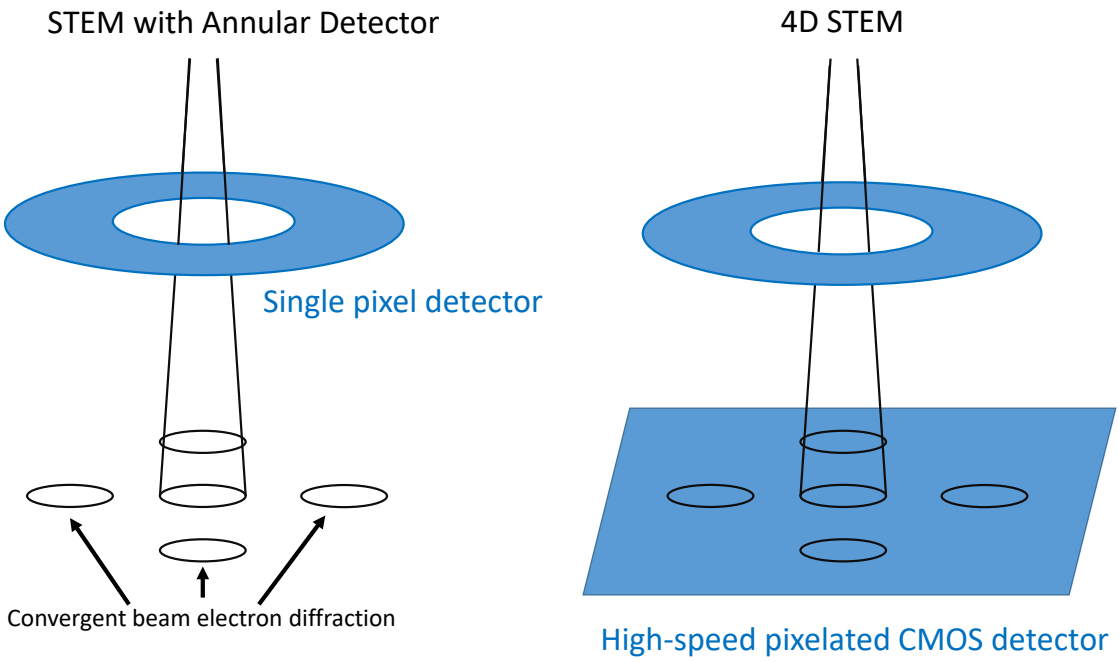

Figure 3.1: **Cartoon of 4-D STEM data acquisition** CBED patterns are averaged over a single annular detector in conventional STEM (left). In 4D-STEM (right), CBED patterns are captured on a high-speed CMOS detector at each electron beam position

The locations of the CBED disks (Fig. 3.2) relative to the central non-diffracted beam are the scattering vectors (G) of the crystal.

3.2 Extracting Temperature from Strain Measurements

Strain can be measured in a 4D-STEM dataset by measuring tiny changes in the locations of the CBED disks. Strain, (ϵ) is simply equal to a normalized change in scattering vector ($\epsilon = -\Delta G/G_0$). If a sample is heated or biased *in situ* , and is allowed to expand freely, this strain can be converted to a temperature change given a known coefficient of thermal expansion. If a material expands uniformly in all directions, and the strain is $\ll 1$, the following formula holds:

$$\epsilon = -3\left(\frac{l - l_0}{l_0}\right) = -3\int_{T_0}^{T} \alpha(T')dT' \tag{3.1}$$

If ΔT is small, $\alpha(T')$ can be Taylor expanded, and $\epsilon = -3\alpha_0\Delta T$, where α_0 is the thermal expansion coefficient at room temperature.

Measuring strain in a polycrystalline film is challenging. In a single-crystal film, a double-tilt holder may be used which can rotate the crystal to lie on zone-axis. Positioning a single crystal on zone-axis will produce good quality CBED patterns with bright, uniformly illuminated disks. Polycrystalline films produce much worse-quality CBED patterns (Fig. 3.2), where only a few, or possibly no CBED disks are illuminated besides the central undiffracted disk. An additional challenge arises where if grains are small, the beam may pass through two or more differently-oriented grains which produce overlapping CBED patterns, complicating data analysis. The precision of the G measurement algorithm will increase as the signal-to-noise ratio of the CBED disks increases. The central, undiffracted disk will always nearly saturate the detector, and thus the signal-to-noise ratio of the diffracted disks will depend on the dynamic range of the detector. The fast Gatan K2 CMOS detector used on the TEAM 1.0 has relatively poor dynamic range compared to a CCD detector, and is the limiting factor for the signal-to-noise ratio of the diffracted CBED disks.

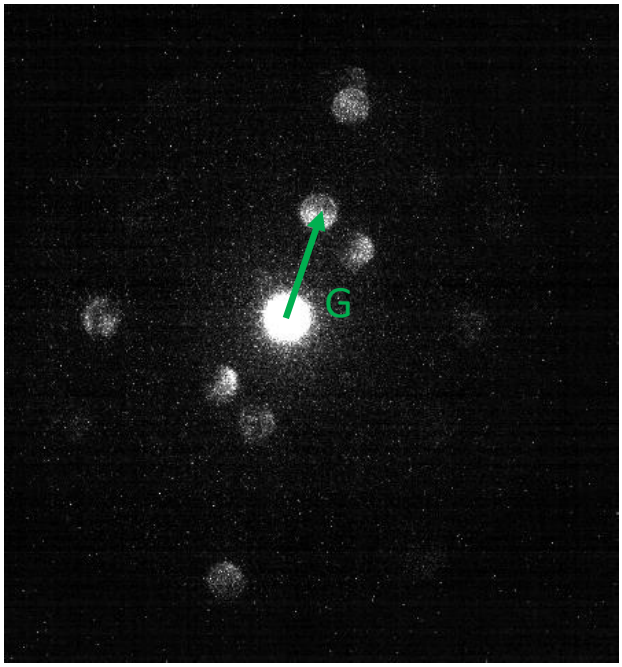

$$\frac{\Delta G}{G_0} = -\Delta\varepsilon$$

Figure 3.2: **CBED pattern acquired on a K2 CMOS detector** A typical CBED pattern acquired from an aluminum film. The central (undiffracted) disk is brightest by over an order of magnitude and consumes most of the dynamic range of the detector. Several diffracted disks are visible, and G is measured as the vector between the undiffracted central disk and a diffracted disk.

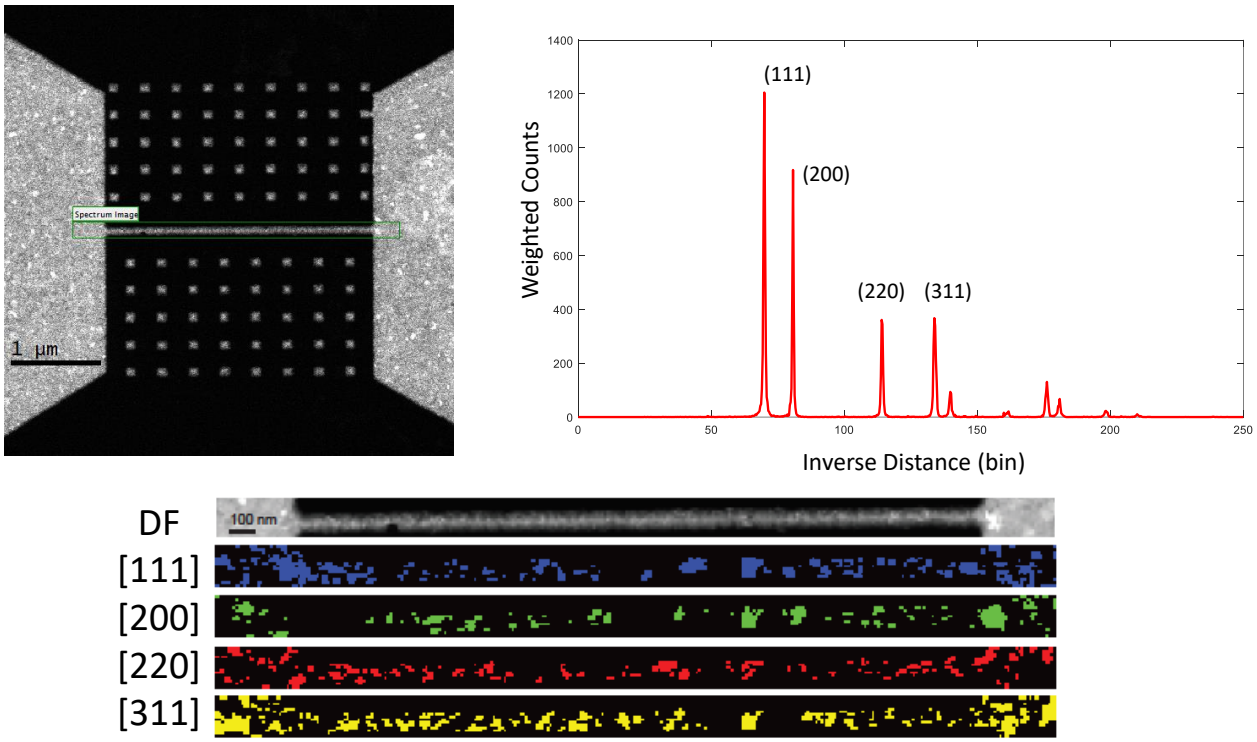

Figure 3.3: **Grain orientations within a polycrystalline aluminum nanowire.** A 4D-STEM dataset is acquired from the green ROI (top left). Each CBED pattern is analyzed to identify G vectors. The G vector lengths are binned and plotted versus cross-correlation fit quality (upper right). Grain orientations can be mapped across the nanowire (lower plots).

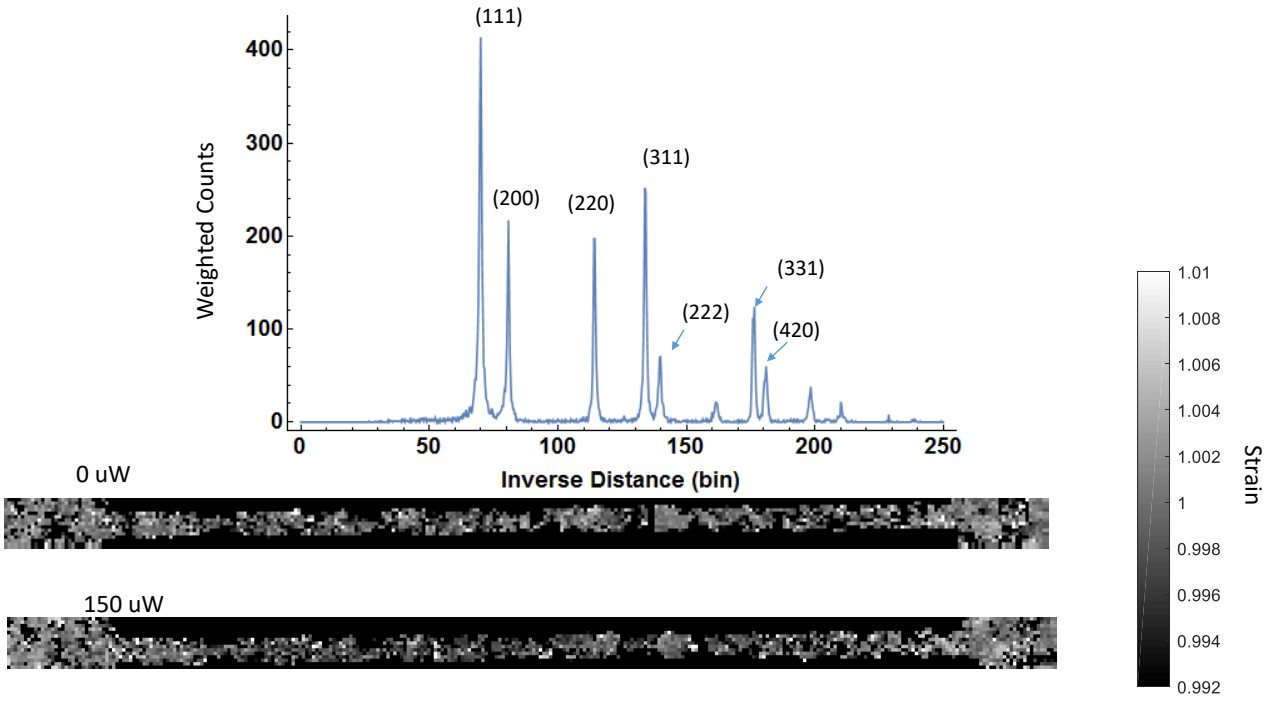

Figure 3.4: **Strain measured from shifts in G.** Strain can be measured from shifts in the G vectors. Changes in G from the (222), (331) and (420) aluminum reflections are averaged and converted to strain. The wire undergoes tensile strain when biased at 150 µW.

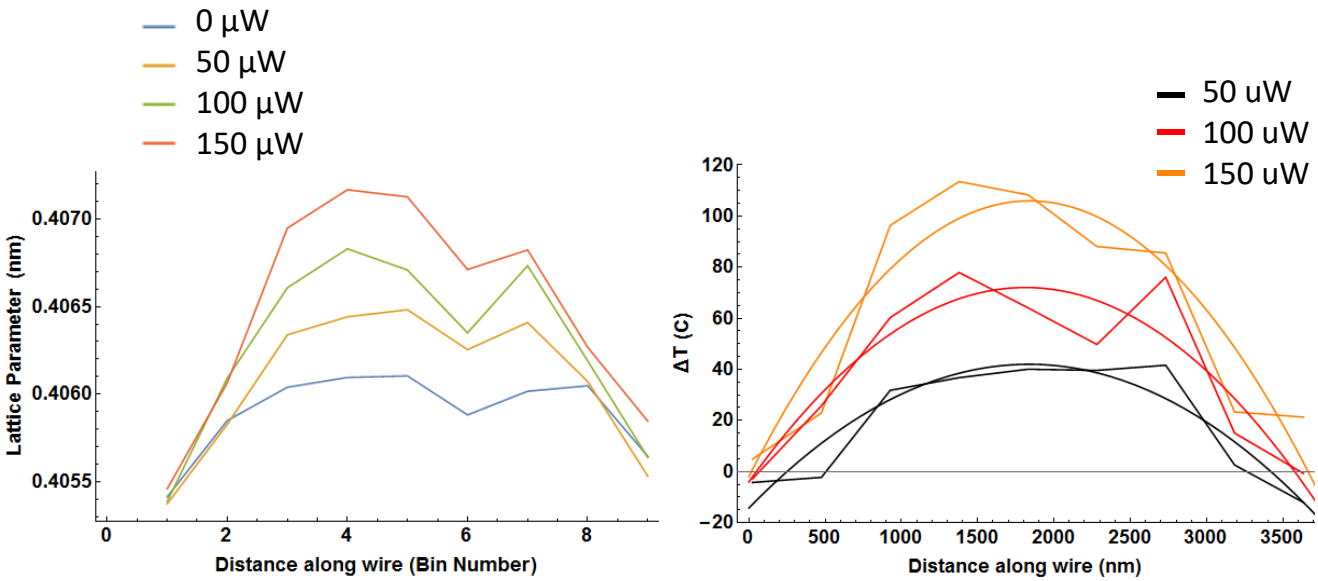

Figure 3.5: **Temperature in an aluminum nanowire measured with 4D-STEM.** Changes in lattice parameter across the length of an aluminum nanowire (left) are converted to changes in temperature (right) given aluminum's known coefficient of thermal expansion.

In this 4D-STEM experiment we bias aluminum nanowires *in situ* on the TEAM 1.0 microscope at the National Center for Electron Microscopy (NCEM) located at Lawrence Berkeley National Laboratory (LBNL). Nanowires are patterned on our group's in-house fabricated silicon nitride windows, supported on silicon substrates. The nanowire patterns are written with e-beam lithography, and 100 nm of aluminum is deposited with an electron-beam evaporator. An ADF image of the nanowire displays the region (green ROI) where 4D-STEM data is collected at each biasing power (Fig. 3.3, top-left).

CBED disks are located[51], and in turn G vectors extracted. G vector length (inverse distance) is binned and plotted versus fit quality (Fig. 3.3, top-right). Quantized peaks are easily visible corresponding to allowed G scattering vectors. Displaying G information in this form is analagous to a standard powder-diffraction pattern acquired with x-ray diffraction.

Windows can be placed around each allowed scattering vector, and the real-space positions that fall within the reciprocal-space window can be mapped (Fig. 3.3, bottom). This is an ability unique to 4D-STEM: Other STEM techniques cannot map grain boundary orientations. It is possible to map grain boundary orientation using dark-field TEM, but this process is cumbersome since an aperture must be aligned over each G vector that is mapped.

Strain is calculated by measuring the changes in position of the center of a diffraction peak (Fig. 3.4). The centers of the peaks can be localized by fitting them to each to a Gaussian distribution. A shift upward in lattice parameter (tensile strain) is visible when the sample is biased at 150 µW (Fig 3.4), although the signal to noise ratio is too poor to see clearly by eye.

Changes in lattice parameter (strain) are easier to see when lattice parameters are binned across the length of the nanowire (Fig. 3.5). In this case the 3 µm wire is binned into nine sections, and thus the spatial resolution is $\sim$ 300 nm. With this binning, a clear parabolic shift in lattice parameter is visible that increases with increasing power. The parabolic change in lattice parameter is because the temperature profile of a Joule-heated wire that is perfectly heat sunk is parabolic[52].

The changes in lattice parameter are converted to changes in temperature using aluminum's coefficient of thermal expansion (Fig. 3.4). Three temperature profiles are plotted, one for each increasing bias power. Each temperature profile is well-fit to a parabola, which is the solution to the 1-D heat equation for a biased wire. A maximum change in temperature (relative to room temperature) of $\sim$ 100°C is measured with 150 µW of bias power.

3.3 Mapping Temperature with Plasmon Energy Expansion Thermometry

The bulk plasmon energy in some materials is described well via the free electron model. The plasma frequency is the solution to a simple harmonic oscillator system: An ionic (negatively) charged gas displaced from its (positively charged) nuclei. The restoring force in this system

is the Coulomb force, and the resonance (plasma) frequency is:

$$\omega_p = \sqrt{\frac{e^2 n}{\epsilon_0 m}} \tag{3.2}$$

where n is the valence electron density. The quantization of this frequency is the plasmon energy, $E_p = \hbar\omega_p$. When a material can expand freely, the valence electron density is temperature-dependent,

$$R(T) \equiv \frac{E_p(T) - E_p(T_0)}{E_p(T_0)} = -\frac{3}{2}\left(\frac{l - l_0}{l_0}\right) = -\frac{3}{2}\int_{T_0}^{T} \alpha(T')dT' \tag{3.3}$$

If the $\Delta T = T - T_0$ is small, $\alpha(T)$ can be Taylor expanded: $\alpha(T) \simeq \alpha_1 \Delta T + \alpha_2 \Delta T^2$. This expression can be inverted to solve for a change in temperature ΔT:

$$\Delta T = \frac{\alpha_1}{2\alpha_2}\left(\sqrt{1 - \frac{8R\alpha_2}{3\alpha_1^2}} - 1\right) \tag{3.4}$$

Therefore a change in bulk plasmon energy can be converted into a temperature change. If the plasmon generation cross-section in a material is large, the low-loss scattering regime will be dominated by primary electrons which have generated one (or multiple) plasmon excitations. Even with a monochromated primary electron beam, the full-width at half maximum (FWHM) of this plasmon peak is fairly broad, on the order of an eV. Notably, an EELS spectrum does not give absolute measurements of energy; They must be referenced to the ZLP. This is because the entire spectrum can be shifted in energy due to imperfectly-aligned electron optics. This shift in energy is also a function of (x,y) position of the probe, since electrons entering the spectrometer from a non-normal angle will be shifted in energy relative to normally-incident electrons. Each individual spectrum must contain at least two fits: the ZLP and the plasmon resonance. The plasmon energy is then the difference between the center of the plasmon and the center of the ZLP. In practice, the ZLP is usually fit well to a normal distribution, and either a normal or Lorentzian distribution is used to fit the plasmon peak.

PEET works remarkably well in aluminum, due to aluminum's sharp plasmon resonance, large plasmon-generation cross section, and large thermal expansion coefficient ($\alpha_1 = 23.5 \times 10^{-6}$ K^{-1}). The free electron model yields an accurate value of plasmon energy: At room temperature ($T_0 = 273$ K), $n(T_0) \simeq 1.8 \times 10^{29}$ m^{-3}, and from equation 3.2, $E_p = 15.8$ eV. This predicted value is within 4% of the measured 15.2 eV.

PEET can be used to measure Joule heating in nanoscale interconnects[53]. An aluminum nanowire is fabricated on an electron-transparent *in situ* biasing substrate using e-beam lithography (Fig. 3.6). The wire is biased at 60 μW in both bias polarities, and EELS spectrum images are collected *in situ* . Changes in plasmon energy are converted to temperature (Eq. 3.4) using aluminum's known coefficient of thermal expansion[53].

Temperature maps and corresponding line profiles show roughly parabolic temperature profiles, which overlap closely in both bias polarities. This overlap in temperature profiles is an important check to the validity of these temperature measurements, since Joule heating is independent of bias polarity. The signal-to-noise ratio is obviously better than the temperature measurements performed by 4D-STEM (Fig. 3.5), which is mainly due to the fact that the strength of a plasmon excitation is not significantly affected by the orientation of a crystal, whereas 4D-STEM only obtains strong signal from preferentially-oriented grains.

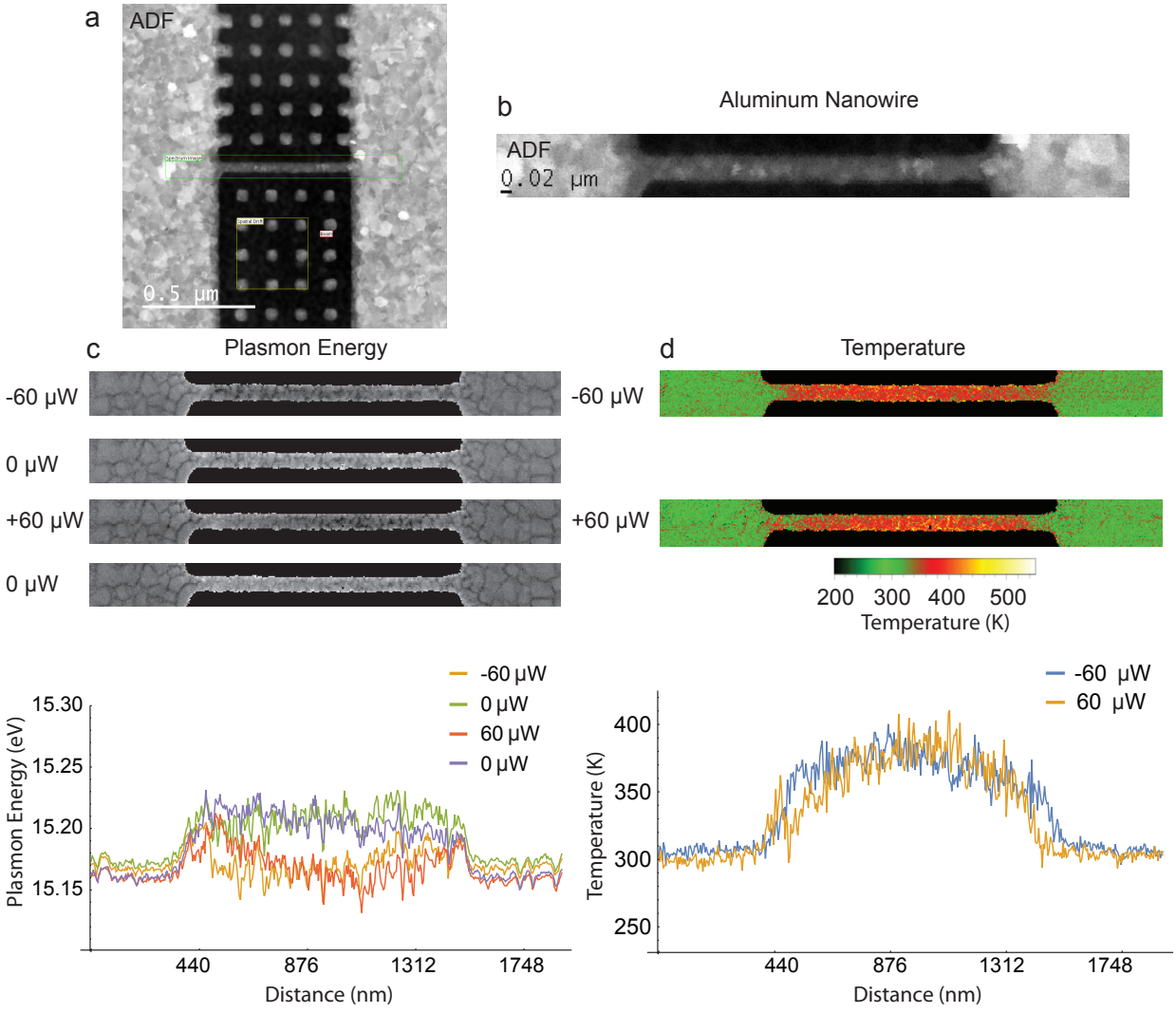

Figure 3.6: **Temperature mapping in a biased aluminum nanowire.** ADF STEM image of an aluminum nanowire (a,b). Plasmon energy maps (c) and corresponding line profiles acquired at two different bias polarities. Changes in plasmon energy are converted to changes in temperature (d).

CHAPTER 4

Mapping Electromigration and Temperature in Cobalt Nanowires

4.1 Introduction to Electromigration

Copper is the current standard back end of line (BEOL) material used in processors[54]. Compared to the previous industry-standard aluminum BEOL interconnects, copper has both higher electrical and thermal conductivity, and superior resistance to electromigration failure[54]. However, as the critical dimension of transistors, and in turn first-level BEOL interconnects, continues to decrease, the resistivity of copper increases along with its susceptibility to electromigration failure[55]. Additionally, copper interconnects require barrier and adhesion layers which increase its resistivity at small critical dimensions[56].

Cobalt is being investigated as a next-generation interconnect material to replace copper[55, 57, 58]. Cobalt's carrier mean-free-path is shorter than copper's, and its bulk electrical conductivity is lower[59]. However, because its carrier mean-free-path is short, cobalt's electrical conductivity is less dependent on an interconnect's critical dimension[58, 59, 60]. Cobalt's activation energy of 1.89 eV is also higher than copper's 1.11 eV, making cobalt more resistant to electromigration at elevated temperatures[55] than copper. Cobalt is also a practical material as it can be deposited by chemical vapor deposition[55] or electrodeposition[57].

The standard model of electromigration ion flux was proposed by Blech and Meieran[61]:

$$J = \frac{nZ^* e \rho j D_0}{kT} e^{-Q/kT} \tag{4.1}$$

where Q and Z^* are the activation energy for self-diffusion and effective charge of the activated ion, respectively, and D_0 is the self-diffusion coefficient. Void growth is caused by a divergence in J, which is usually by a non-zero divergence in j (current crowding), or T (Joule heating). The effective ion charge is a critical material-based parameter, which determines partly how resistant a material is to electromigration failure. There is agreement that at high temperatures (1250 °C), cobalt's Z^* is positive[62, 63], and at lower temperatures (below 615 °C) it switches to negative[64, 65]. The reason for a switch in sign of the effective ionic charge is not known with certainty, but may be due to different electromigration mechanisms dominating at different temperatures.

4.2 Optimization of Multi-Peak Fit Windows

EELS analysis, as with most spectroscopic methods, is done by fitting functions to excitations, such as core-loss excitations, plasmon excitations, and the zero-loss peak. Most work in EELS centers around core-loss excitations, which can be analyzed by fitting a power-law background to an energy windows immediately adjacent to a core-loss edge[6]. Multiple edges from different elements can be fit within one spectrum, and the relative intensities of the edges can give elemental concentrations. Additionally, the near edge structure of a core-loss edge can yield valuable bonding information that is not possible with EDS.

To analyze Joule heating and changes in thickness due to electromigration, we focus on the low-loss spectra, in particular the plasmon excitation and the zero-loss peak. Cobalt nanowires are suspended on 15-20 nm silicon nitride membranes. Unfortunately, silicon nitride also has a sizeable plasmon resonance, which overlaps almost exactly with the cobalt plasmon in terms of energy and full-width at half maximum. This overlap can produce systematic errors in material thickness and PEET-derived temperature, as we have demonstrated in a previous study with silicon nanoparticles suspended on silicon nitride membranes[66].

As we have reported previously[66], when imaging silicon nanoparticles with EELS the intensity of the silicon nitride plasmon relative to the intensity of the silicon plasmon increases near the thin edges of the silicon nanoparticle. Since the the energy of the silicon nitride plasmon is higher ($\sim$ 23 eV) than the silicon plasmon ($\sim$ 16 eV), a single-function fit will yield artifically high plasmon energies near the thin edge of the silicon nanoparticle. This effect is an artifact of overly-simple curve fitting and not a real phenomenon. The solution to this problem is to increase the complexity of the curve fitting routine: The sum of two Lorentzian distrubutions must be used to fit the sum of the silicon nitride and silicon plasmon peaks. Adding 3 extra parameters to the fit would double the number of free parameters and increase the error of the fit parameters. To minimize this problem, the silicon nitride width and center are fit off the edge of the nanoparticle, when the beam is over bare silicon nitride. The center and width of the silicon nitride plasmon are assumed to not change when the beam is over the silicon and silicon nitride, and thus are fixed parameters. The intensity

of the silicon nitride plasmon can change when the beam is off the nanoparticle versus on the nanoparticle, and thus the intensity of the silicon nitride peak is a free parameter across the image.

With this algorithm the number of parameters is only increased by one, from three to four, and the systematic effect based on silicon thickness is greatly minimized. We apply this same algorithm to the analysis of cobalt nanowie EELS data. Although the thickness of the nanowire is relatively uniform, at least compared to a spherical nanoparticle, there are still two significant systematic errors that can be corrected by implementing a multi-peak fitting scheme. Firstly, the absolute thickness of the cobalt film is artifically inflated by neglecting to separate the silicon nitride signal. Secondly, the PEET-derived temperatures can be artifically lowered, since the CTE of silicon nitride is significantly smaller (3×10^{-6}), than cobalt's CTE (12×10^{-6}). Since the silicon nitride expands at approximately a quarter of the rate of cobalt's, its plasmon energy will hardly change with temperature. Adding a shifting cobalt plasmon with an unmoving silicon nitride plasmon will reduce the shift of their sum (if fit with a single Lorentzian distribution), and thus will artificially reduce the PEET-derived temperatures.

Multi-peak fitting is performed in Mathematica using the "NonlinearModelFit" built-in function. Prior to fitting the spectra to the various model functions, the proper fit windows must be selected. Both the fit windows for the ZLP and the plasmon must be independently optimized. The ZLP is asymmetric, and both its left and right fit are optimized separately (Fig. 4.1). To optimize the fit bounds, two relevant parameters of fit quality must be compared against each other. The choice is somewhat arbitrary, but we choose the reduced chi squared and the error in the center of the Gaussian model. As the window size increases, in general the reduced chi squared parameter will increase, and the error will decrease. The optimal value for the fit window edge strives to minimize these two fit quality parameters.

In the case of an asymmetric distribution, like the ZLP, first one bound of the fit is fixed, and the right bound is varied. Once the right bound is optimized, it then held constant and the left bound of the fit is optimized. This process is performed iteratively until the values

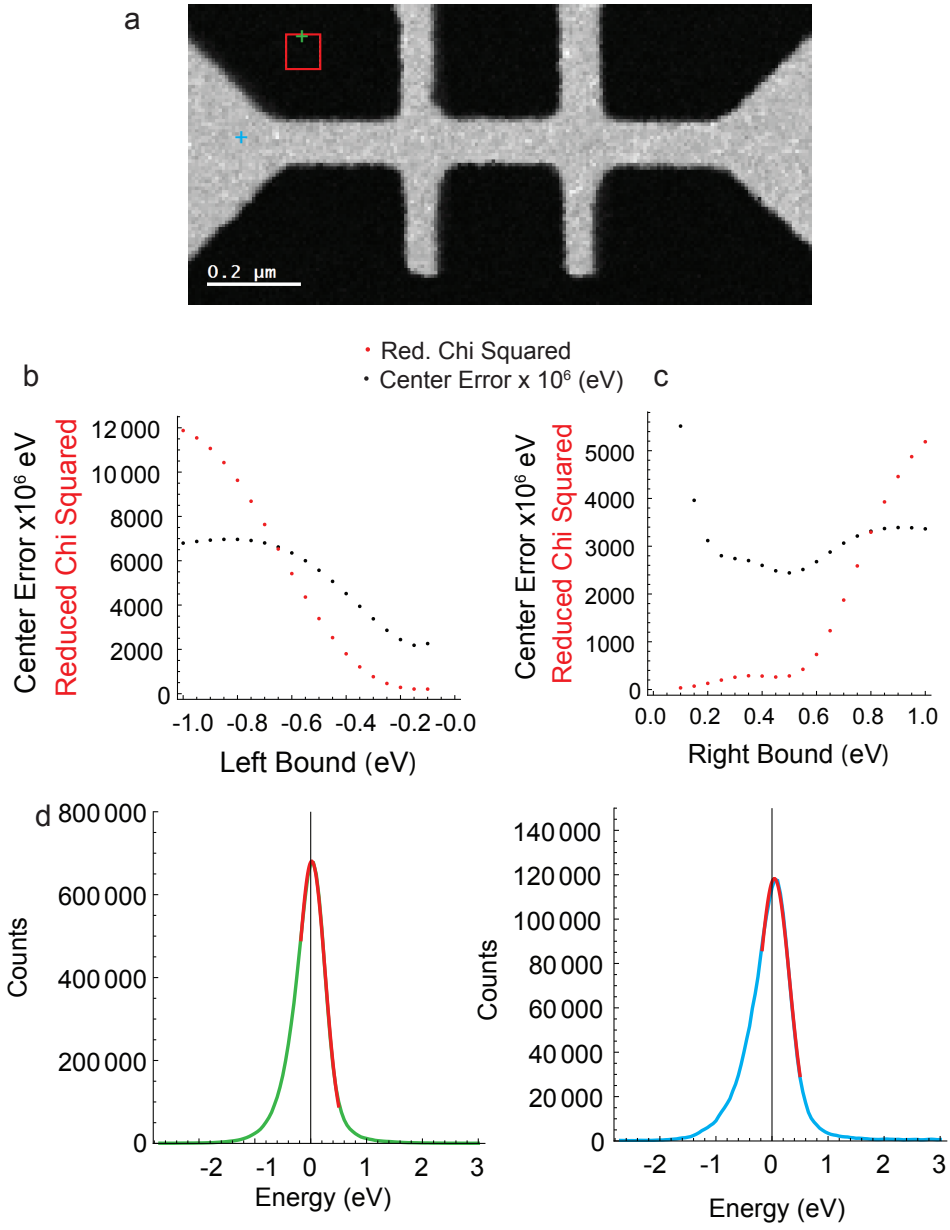

Figure 4.1: **Optimizing the fit bounds for an asymmetric ZLP.** A red square ROI displayed on the STEM ADF image of the nanowire (a) denotes the location spectra that are used to optimize the ZLP fit bounds. The left bound (b) and the right bound (c) are optimized iteratively. The fit window works well for spectra taken from the silicon nitride alone (d) and the silicon nitride and cobalt (e), despite a large difference in ZLP amplitude.

for both bounds are the same from one iteration to the next. Importantly, since the spectra are noisy and vary from one beam position to the next, every spectrum within a region of 10 by 10 pixels (100 pixels total) is fit with a Gaussian distribution, and the mean values of the reduced chi squared and center mean are taken. The final convergent solution for this iterative process is plotted for both the left (Fig. 4.1 b) and right (Fig. 4.1 c) bounds of the fit window. The optimal bounds are determined to be -0.0175 eV and 0.5 eV . Although the amplitude of the ZLP changes when the beam is off the cobalt (Fig. 4.1 d) relative to impacting the cobalt (Fig. 4.1 e), the quality of the fit is the same, and thus the bounds need not change across the EELS image.

As the next step in the multi-peak fitting process, the silicon nitride is fit independently of the cobalt (i.e. when the beam is not incident on the cobalt), in order to extract a mean plasmon energy and width of the silicon nitride. Unlike the ZLP, the silicon nitride plasmon is nearly symmetrical, and thus the window optimizaton process is simpler: Instead of optimizing both bounds of the fit window, the fit window will be centered on the center of the plasmon peak and only the width of the window need be optimized. Again, a 10 by 10 array of EELS spectra (Fig. 4.2 a, red ROI) are fit independently for a range of fit window widths, and the mean of the reduced chi squared the mean of the center error is plotted versus fit window width (Fig. 4.2 b). The optimal value of fit window width, which minimizes both the center error and the reduced chi squared is 11 eV. A typical silicon nitride spectrum with a Lorentzian distribution fit is plotted (Fig. 4.2 c), using the optimal window found through the reduced chi squared and center error minimization routine.

Using the fit windows optimized through the previously-described routine, ZLP is fit across the entire silicon nitride membrane (Fig. 4.3). Fits are performed quickly in Mathematica, using the "ParallelTable" command to utilize multiple CPU threads simultaneously. Values for ZLP amplitude, center, and standard deviation are sorted into bins and plotted. Gaussian distributions are fit to the histograms for the amplitude and standard deviation fit parameters. The center of the Gaussian distribution is taken to be the mean value of the fit parameter, and the standard deviation is taken to be the error bar of that fit parameter.

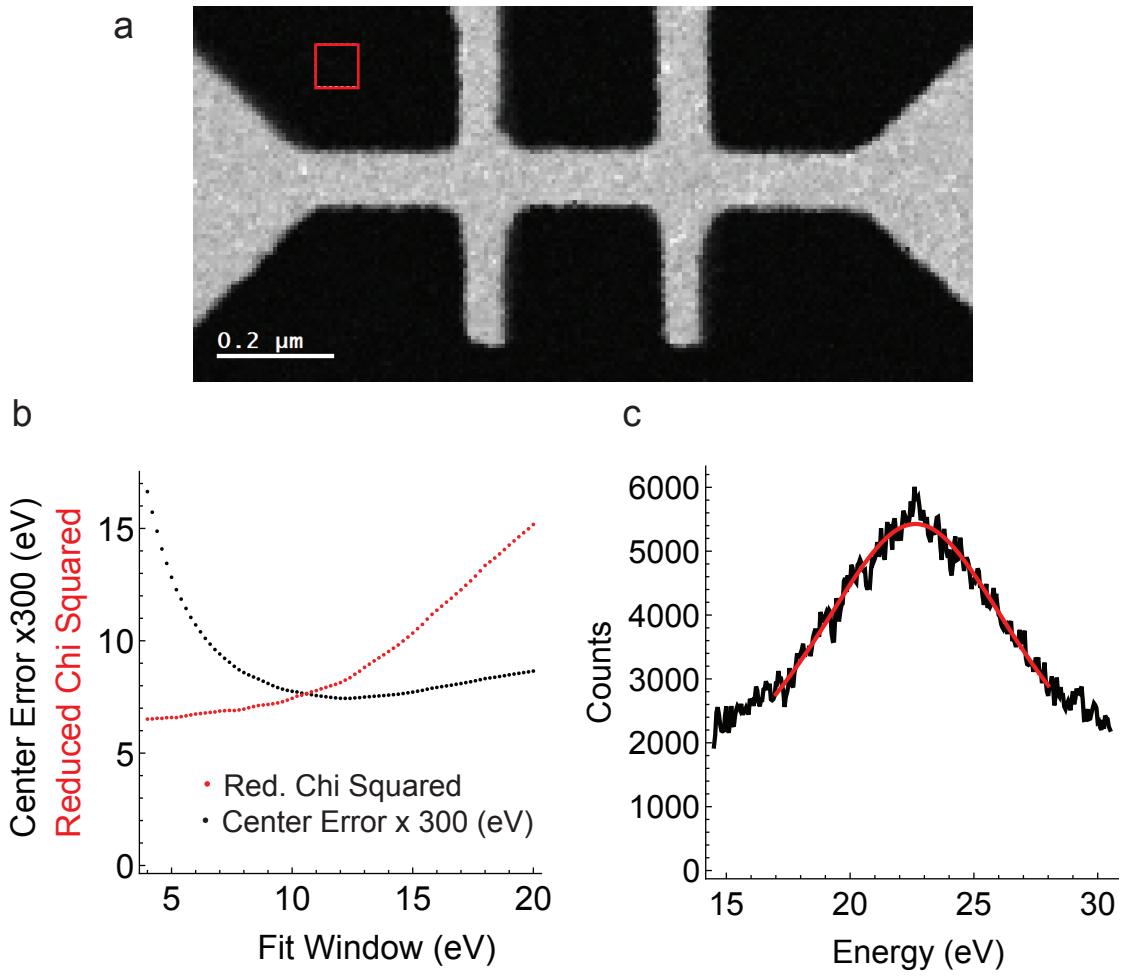

Figure 4.2: **Optimizing fit bounds for the silicon nitride plasmon** A red square ROI displayed on the STEM ADF image of the nanowire (a) denotes the location of spectra that are used to optimize the silicon nitride fit bounds. Unlike the ZLP, the nitride plasmon peak is symmetric and only requires an optimization of the width of the fit window (b). The final fit (red line) is superimposed on a typical silicon nitride spectrum (c).

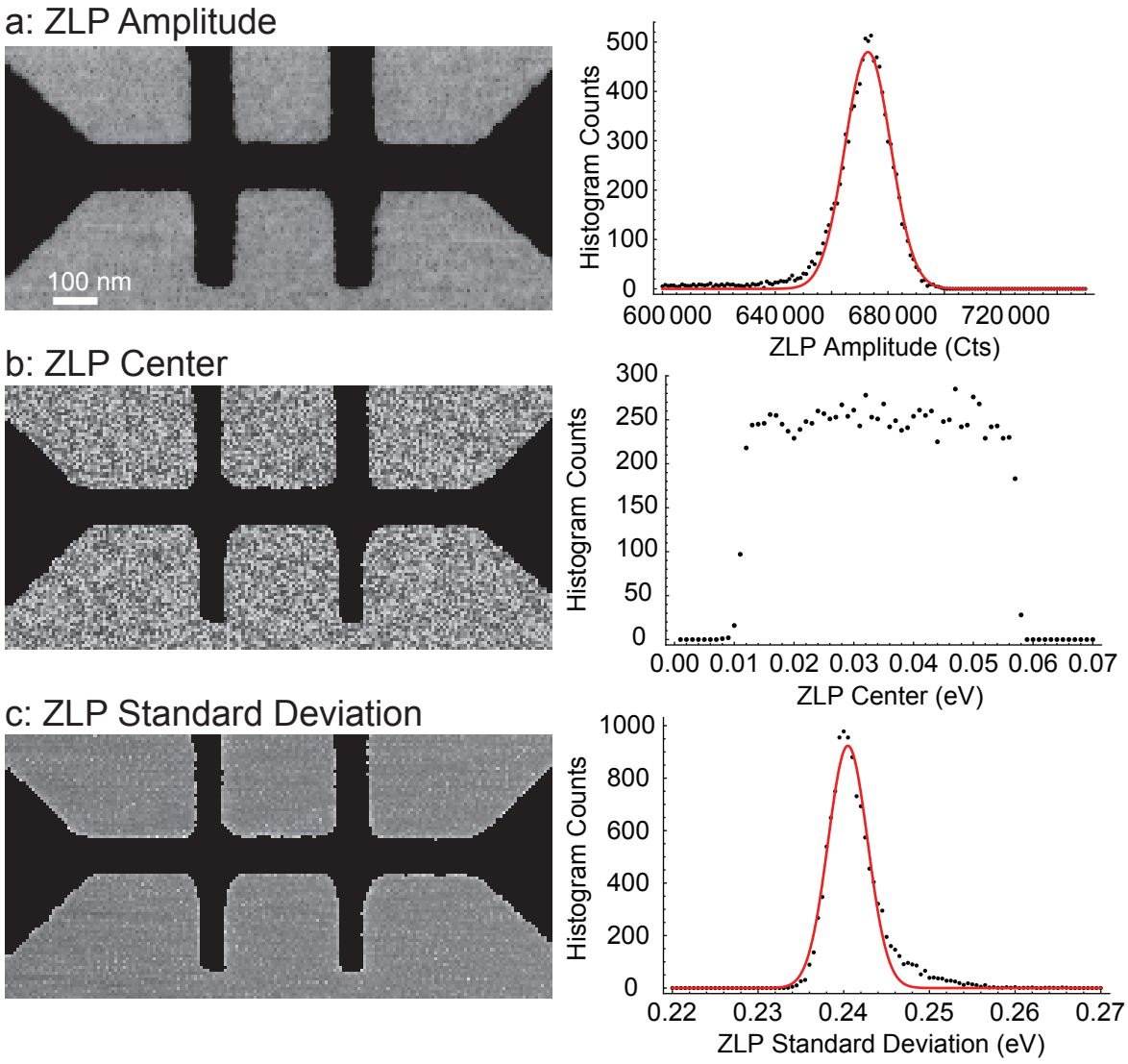

Figure 4.3: **ZLP fit parameters and histograms** The ZLP is fit individually for each spectrum, and histograms of the ZLP amplitude (a), center (b), and standard deviation (c) show the distribution of the fit parameters. The amplitude and standard deviations are normally distributed. The center of the Gaussian histogram fit is the mean value, and the standard deviation of the histogram fit is the error.

This scheme works well for the amplitude and standard deviation of the ZLP fit, however the values for ZLP center are not normally distributed. The reason for this is that the EELS images are roughly aligned using a custom script written by Matthew Mecklenburg in Digital Micrograph, before they are imported into Mathematica.

A similar scheme is applied to analyze the silicon nitride plasmon when the beam is not impacting the cobalt. Lorentzian distributions are fit to each individual EELS spectrum, and a simple filter is used to determine when the beam is passing through solely the silicon nitride, or the cobalt and silicon nitride. The filter in this case is derived from the ZLP amplitude fits. When the beam is impacting the cobalt and the silicon nitride, a higher fraction of primary electrons scatter inelasically out of the ZLP relative to when the beam is only impacting the silicon nitride. Thus the ZLP will have a significantly lower amplitude in spectra acquired when the beam is incident on the cobalt. Although the cutoff criteria can vary from sample to sample, a limit of 4000 counts of ZLP amplitude serves as a good filter in Fig. 4.4 to distinguish the nanowire from its silicon nitride support membrane. Each of the Lorentzian fit parameters (amplitude, center, width) is Gaussian distributed, and fits to these parameters binned into histograms yield the best fit value and the error.

4.3 PEET in Cobalt by Multi-Peak Fitting

Another optimization routine is performed to set the bounds for the cobalt multi-peak fitting. Three functions are used in this scheme, along with data collected from when the beam is over the bare silicon nitride membrane.

The first assumption that is made is that the silicon nitride support membrane is of uniform thickness, which is reasonable considering the relevant area is a micron square of a 4 inch wafer coated by CVD silicon nitride. There are multiple ways to calculate thickness EELS data, each of which is derived from Poisson statistics. The counts under each peak (I_n) are described by the following formula[6]:

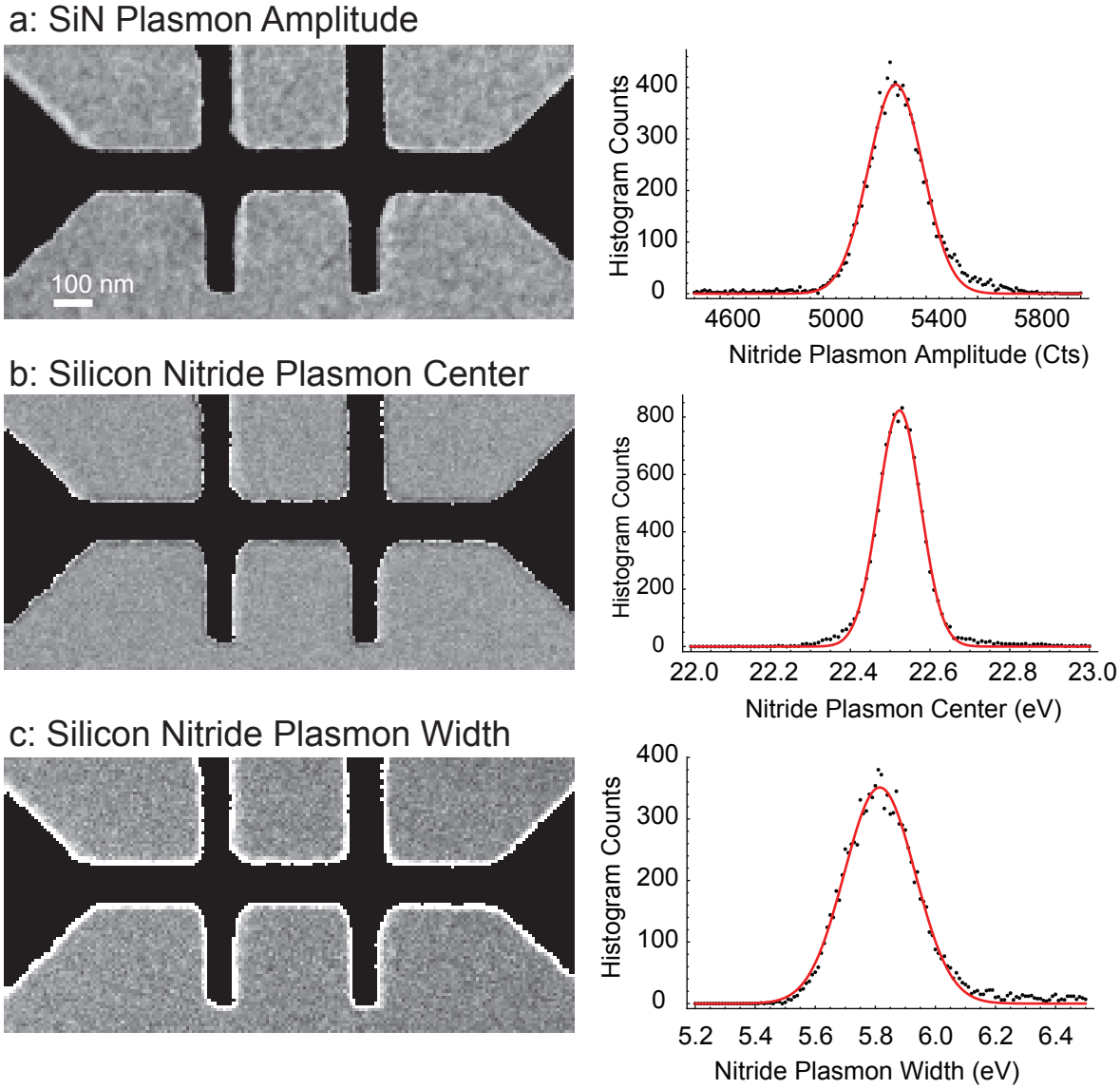

Figure 4.4: **Silicon nitride fit parameters and histograms** The silicon nitride plasmon is fit individually for each spectrum, and histograms of the silicon nitride amplitude (a), center (b), and standard deviation (c) show the distribution of the fit parameters. All fit parameters are normally distributed. The center of the Gaussian histogram fit is the mean value, and the standard deviation of the histogram fit is the error.

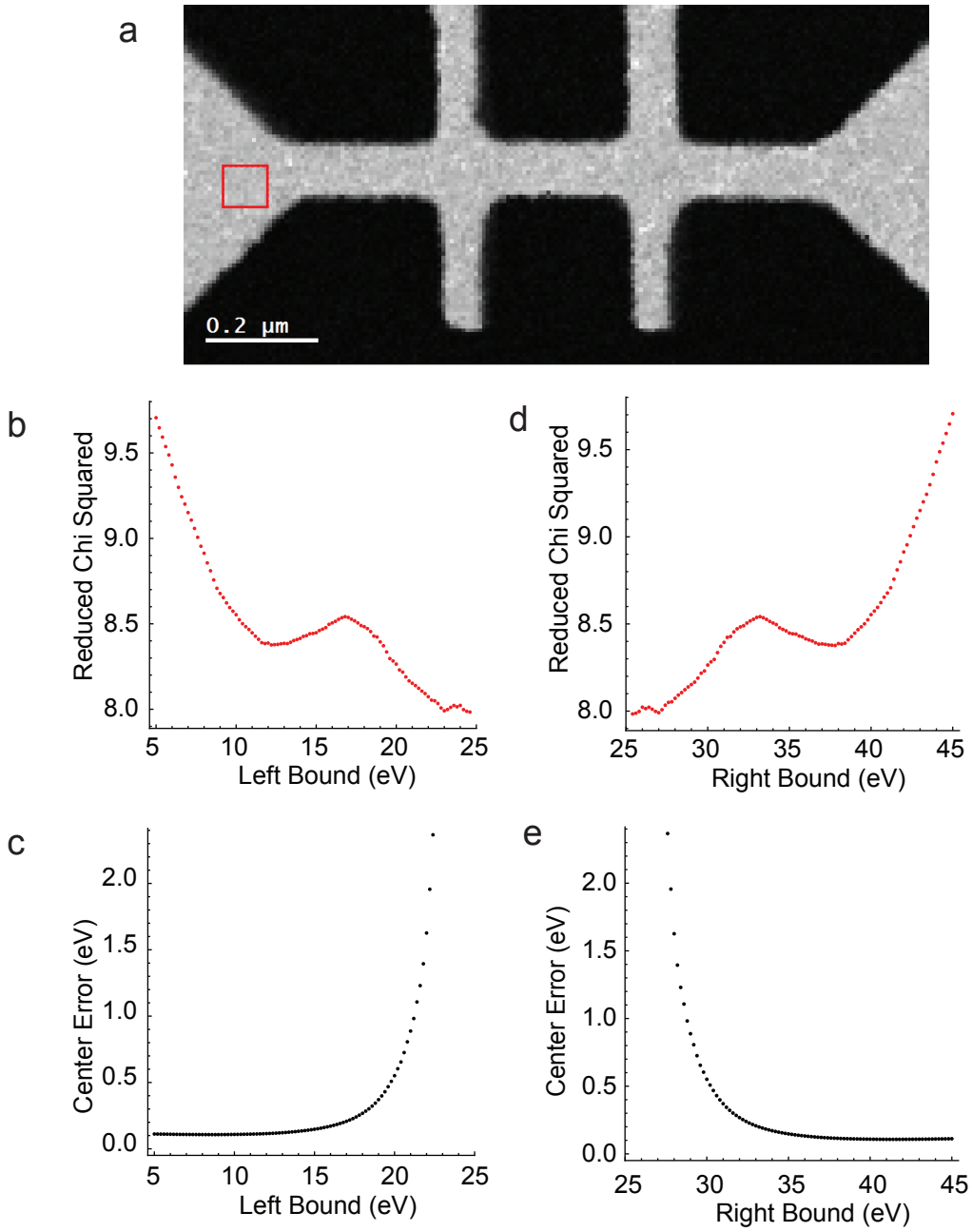

Figure 4.5: **Cobalt multi-peak fit window optimization**. A red square ROI displayed on the STEM ADF image of the nanowire (a) denotes the location of spectra that are used to optimize the cobalt multi-peak fit bounds. The reduced chi squared metric (b) and center error (c) metric are plotted as a function of left fit bound location. The process is repeated for the right fit bound: The reduced chi squared metric (d) and center error (e) metric are plotted as a function of right fit bound location.

$$I_n = \frac{I_T}{n!}\left(\frac{t}{\lambda}\right)^n e^{-t/\lambda} \tag{4.2}$$

where t is the film thickness, λ is the plasmon generation mean free path, n is the order of the plasmon excitation, and I_T are the total counts. In our data the relevant peaks are the ZLP ($n = 0$) and the first cobalt plasmon ($n = 1$). From Eq. 4.2:

$$\frac{I_1}{I_0} = \frac{t}{\lambda} \tag{4.3}$$

In other words, the thickness of the a film (in MFP's) is equal to the ratio of the counts under the plasmon to the counts under the ZLP. In this way the thickness of the silicon nitride membrane can be precisely measured in each image. The counts under the ZLP are proportional to the product of the Gaussian standard deviation and the amplitude, which are precisely determined (Fig. 4.3). Similarly, the counts under a Lorentzian distribution are proportional the product of the amplitude and the width, which are both precisely determined using histogram fits of data from all bare nitride beam positions (Fig. 4.4). The ratio of counts under the silicon nitride plasmon to the counts under the ZLP is then the mean thickness of the film.

The sum of two Lorentzian distributions is fit to the overlapping silicon nitride and cobalt plasmons. The silicon nitride plasmon width and center are assumed to be the same when the beam is incident on the cobalt compared to when the beam is impacting bare nitride. Thus the silicon nitride width and center, extracted from histogram fits (e.g. Fig 4.4), do not vary with beam position across a spectrum image. The silicon nitride amplitude, however, is not constant since when the beam is incident on the cobalt since the cobalt will scatter many electrons away from the EELS detector, and reduce the counts under the ZLP and silicon nitride plasmon. However, since the thickness of the silicon nitride is constant, the ratio of the ZLP counts to the silicon nitride plasmon counts stays constant across the image. At each beam position, the counts under the ZLP, along with the constant nitride thickness, are used to lock in the counts under the silicon nitride plasmon.

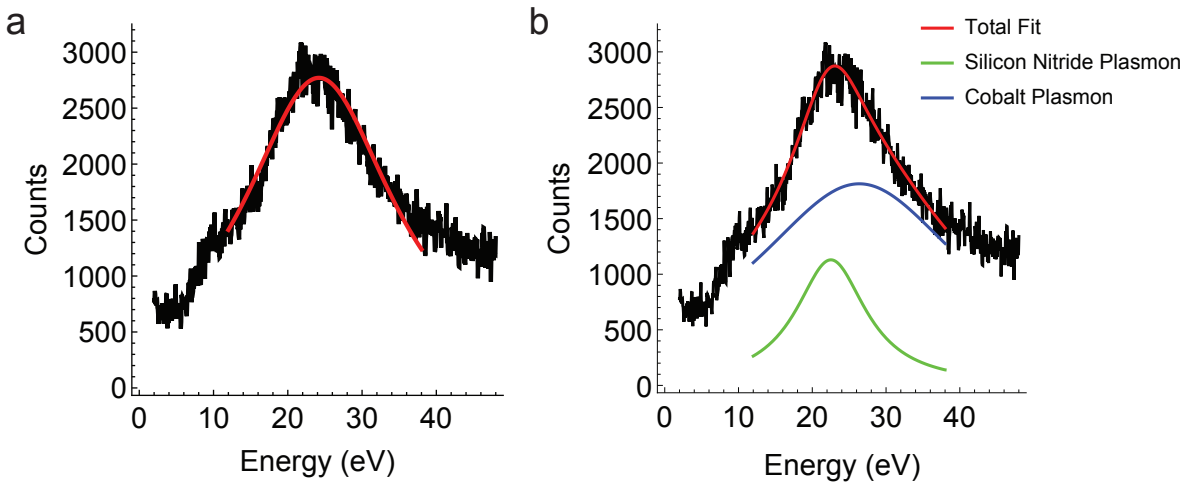

Figure 4.6: **Optimized cobalt multi-peak fit**. The cobalt and silicon nitride plasmons, fit by a single Lorentzian distribution (a). The same fit window is fit with the sum of two Lorentzians, one each for the silicon nitride and the cobalt plasmons. The silicon nitride parameters are set by the thickness of the silicon nitride (determined by analysis done when the beam is off the cobalt), and the counts under the ZLP.

Thus there are no extra added fit parameters in the multi-peak fitting scheme, which minimizes fit errors. Again, the fit window bounds are optimized independently due to the asymmetry of summed silicon nitride and cobalt plasmons. Reduced chi squared and cobalt center error are minimized simultaneously for the left and right bound of the cobalt multi-peak fit (Fig. 4.5). Comparing an example Lorentzian single-peak fit (Fig. 4.6 a) to the multi-peak fit of the same optimized window (Fig. 4.6 b), the multi-peak fit has a better reduced chi squared value, but almost double the error in cobalt plasmon center. Also notable, the cobalt plasmon is ~ 2 eV higher when the nitride is fit separately, compared to when the sum of the nitride and cobalt are fit to a single Lorentzian.

4.4 Plasmon Energy Expansion Thermometry (PEET)

Plasmon energy expansion thermometry (PEET) is an EELS-based STEM technique which has been used to measure temperature in aluminum[53], silicon[66], molybdenum disulfide[67],

silicon nitride[68], and indium[69], with sub-10 nm spatial resolution. PEET measures temperature-dependent changes in a material's bulk plasmon energy using EELS, and converts those changes into temperature measurements:

$$E_p = \hbar\omega_p = \hbar\sqrt{\frac{e^2 n}{\epsilon_0 m}} \tag{4.4}$$

where n is the valence electron density. When a material can expand freely, the valence electron density is temperature-dependent: $n(T) \simeq n(T_0)[1 - 3f(T)]$, where $f(T) \equiv \int_{T_0}^{T} \alpha(T')dT'$. A normalized change in plasmon energy, $R(T)$, can thus be related to a temperature change:

$$R(T) \equiv \frac{E_p(T) - E_p(T_0)}{E_p(T_0)} = -\frac{3}{2}\int_{T_0}^{T} \alpha(T')dT' \tag{4.5}$$

If the $\Delta T = T - T_0$ is small, $\alpha(T)$ can be Taylor expanded: $\alpha(T) \simeq \alpha_1$. This expression can be inverted to solve for a change in temperature ΔT:

$$\Delta T = -\frac{2}{3}\frac{R}{\alpha_1} \tag{4.6}$$

where the thermal expansion coefficient in cobalt[70], α_1, is 13×10^{-6}/K, and the rate of change in temperature per change in plasmon energy is -2.1 K/meV.

4.5 Measuring Temperature in Cobalt Nanowires via the TCR

Temperature changes due to Joule heating can be measured using cobalt's temperature coefficient of resistance (TCR). Measuring a temperature change using a known TCR is the basis for resistance thermometry[71, 72], and we apply it here in these nanowires. The sense leads on these nanowires are placed close to the center of the nanowire, where the temperature increase due to Joule heating will be uniform. A bulk material's resistance, $R_b(T)$, is due to phonon scattering and is thus temperature dependent:

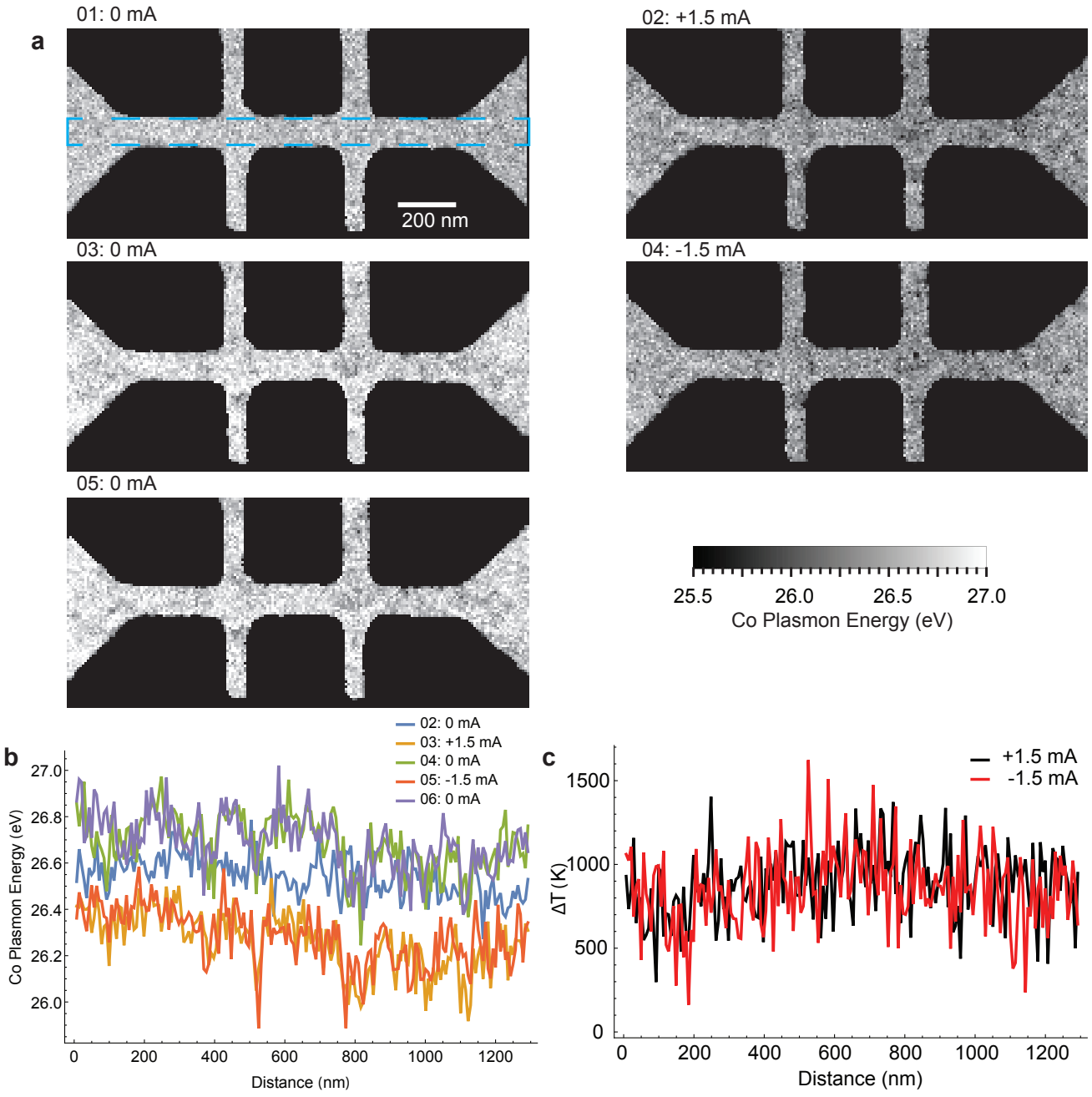

Figure 4.7: **PEET temperature profiles across a biased cobalt nanowire.** PEET temperatures, vertically averaged over the dashed blue box (a), are calculated at two different bias current and both polarities are superimposed on a line profile (b). The maximum change in temperature measured due to Joule heating is 1000 ± 200 K.

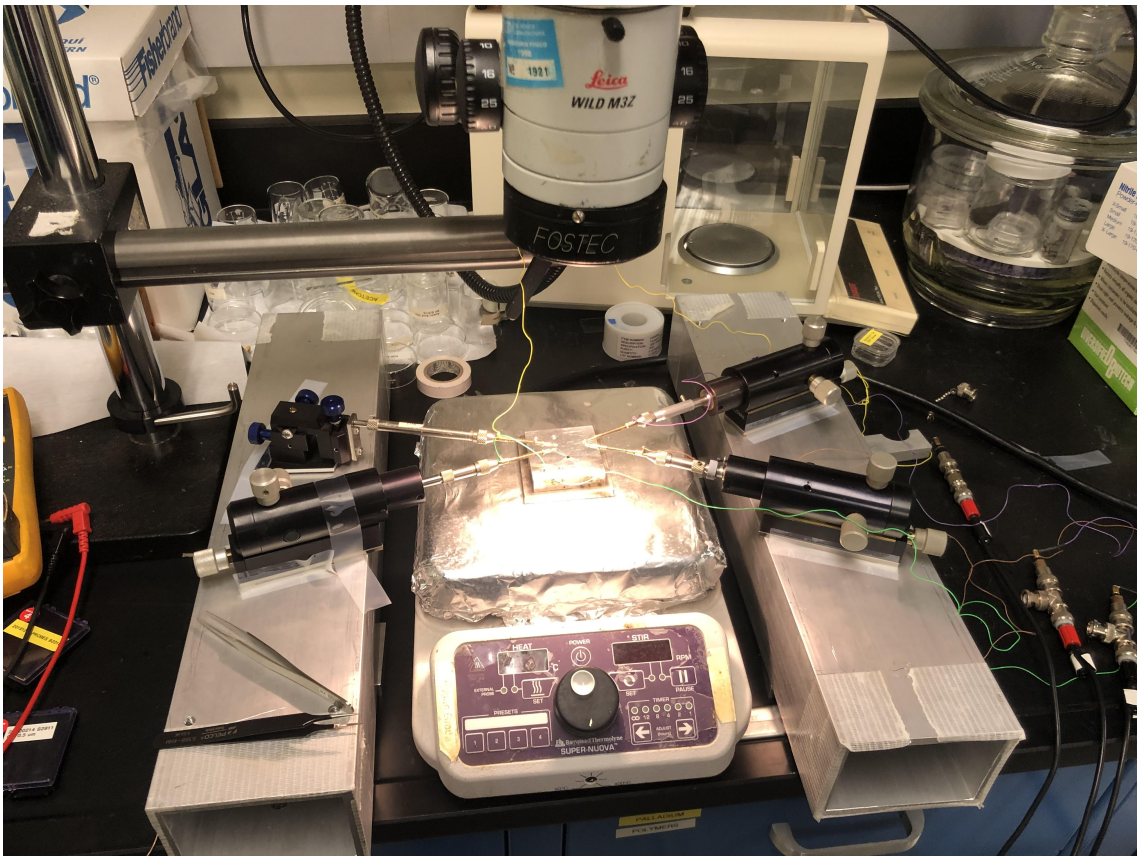

Figure 4.8: **Heated probe station setup** A probe station with a heated stage is rigged with micromanipulators and a hot plate. A block of aluminum is used as a support base for the chip to provide a uniform temperature. Temperatures are measured by touching a thermocouple to the aluminum block.

$$\frac{R_b(T)}{R_{b0}} = 1 + \alpha(T - T_0) \tag{4.7}$$

where R_{b0} is the bulk resistance at room temperature, and α is the TCR in units of inverse Kelvin. TCR coefficients are available in a wide range of materials. The above formula (Eq. 4.7) can be inverted to measure changes in temperature given a change resistance. Metals with a high TCR can measure temperature changes more precisely, and fortuitously bulk cobalt has a high TCR[73] of $0.0068K^{-1}$ compared to other metals.

However, the resistance of a thin-film with smaller grains has an added temperature-independent component, R_g, which is due increased grain-boundary and surface scattering.

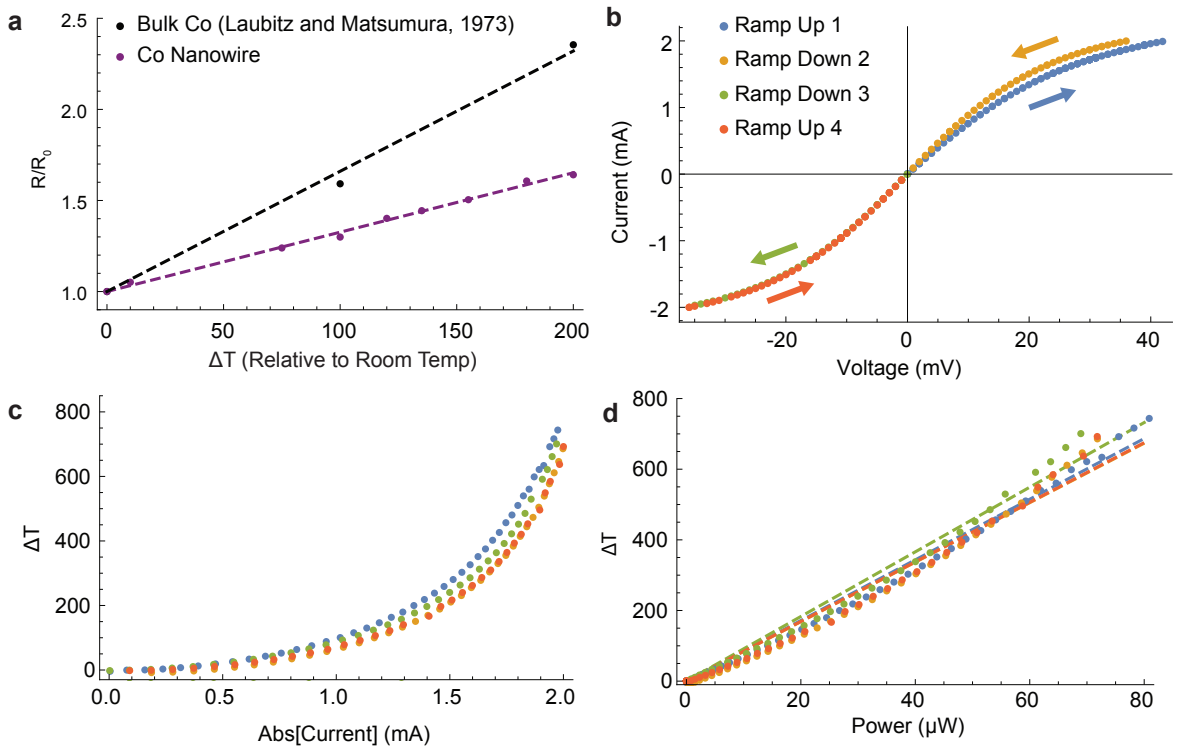

Figure 4.9: **Measuring temperature via cobalt's TCR.** Resistance measured in a 4-wire nanowire device is measured versus chuck temperature, and compared to bulk (a). Transport data for all four current ramps demonstrates a decrease in resistance after the first ramp, due to grain growth. Temperature changes due to Joule heating are plotted versus current (c) and power (d). The ΔT vs. power plots are fit well to lines, as expected from the heat equation.

The total resistance is the sum of these two terms[74]:

$$R(T) = R_b(T) + R_g \tag{4.8}$$

The grain boundary and surface resistance term, R_g varies with film thickness, grain structure, and surface-to-volume ratio among other factors, and must be measured.

$$R(T) = R_{b0}(1 + \alpha(T - T_0)) + R_g \tag{4.9}$$

$$\frac{R(T)}{R_{b0} + R_g} = 1 + \frac{R_{b0}}{R_{b0} + R_g}\alpha(T - T_0) \tag{4.10}$$

The 4-wire resistance $R(T)$ can be measured as a function of temperature by using a probe station with a heated stage, and the quantity $R_{b0}/(R_{b0} + R_g)$ is the slope of the normalized resistance versus temperature. This was done for an individual nanowire on a hot plate (Fig. 4.8) heated to 200 K above room temperature (Fig. 4.9 a, purple points). The slope of the nanowire data is 48% the slope of bulk cobalt, and therefore 48% of the room temperature resistance is temperature-independent and due to surface and grain boundary scattering.

The 4-wire transport data from the four ramps of the experiment of Fig. 4.13 is significantly non-linear due to a resistance increase caused by Joule heating (Fig. 4.9 b). The ramp down after 15 minutes of bias at 2.0 mA has significantly higher current the ramp up (Fig. 4.9), due to an increase in grain size and a corresponding drop in resistance.

To calculate temperature from transport data, the differential resistance is measured and the temperature-independent resistance is subtracted from that quantity, yielding the temperature-dependent resistance. This resistance is converted to a change in temperature (Fig. 4.9 c) using the bulk function for cobalt's TCR, which has been measured[73] up to 1700 K. When plotted versus current, the temperatures reached in the first ramp are higher than subsequent ramps, which is a result of the wire's higher resistance before grain growth occurs.

When temperature is plotted versus power (Fig. 4.9 d), all four ramps overlap closely. The temperature points also fall nearly on a line, which is expected by the steady-state heat equation $j^2\rho = -\kappa\nabla^2 T$. The solution to this equation in a Joule heated wire[52] dictates a maximum temperature of $T_{max} = T_0 + j^2\rho L^2/8\kappa$. The total power deposited by Joule heating is $P = j^2\rho LA$, therefore $T_{max} = T_0 + \alpha P$, where A is the cross-sectional area of the wire, L is the length of the wire, P is the power deposited, and $\alpha = L/8\kappa A$. The maximum

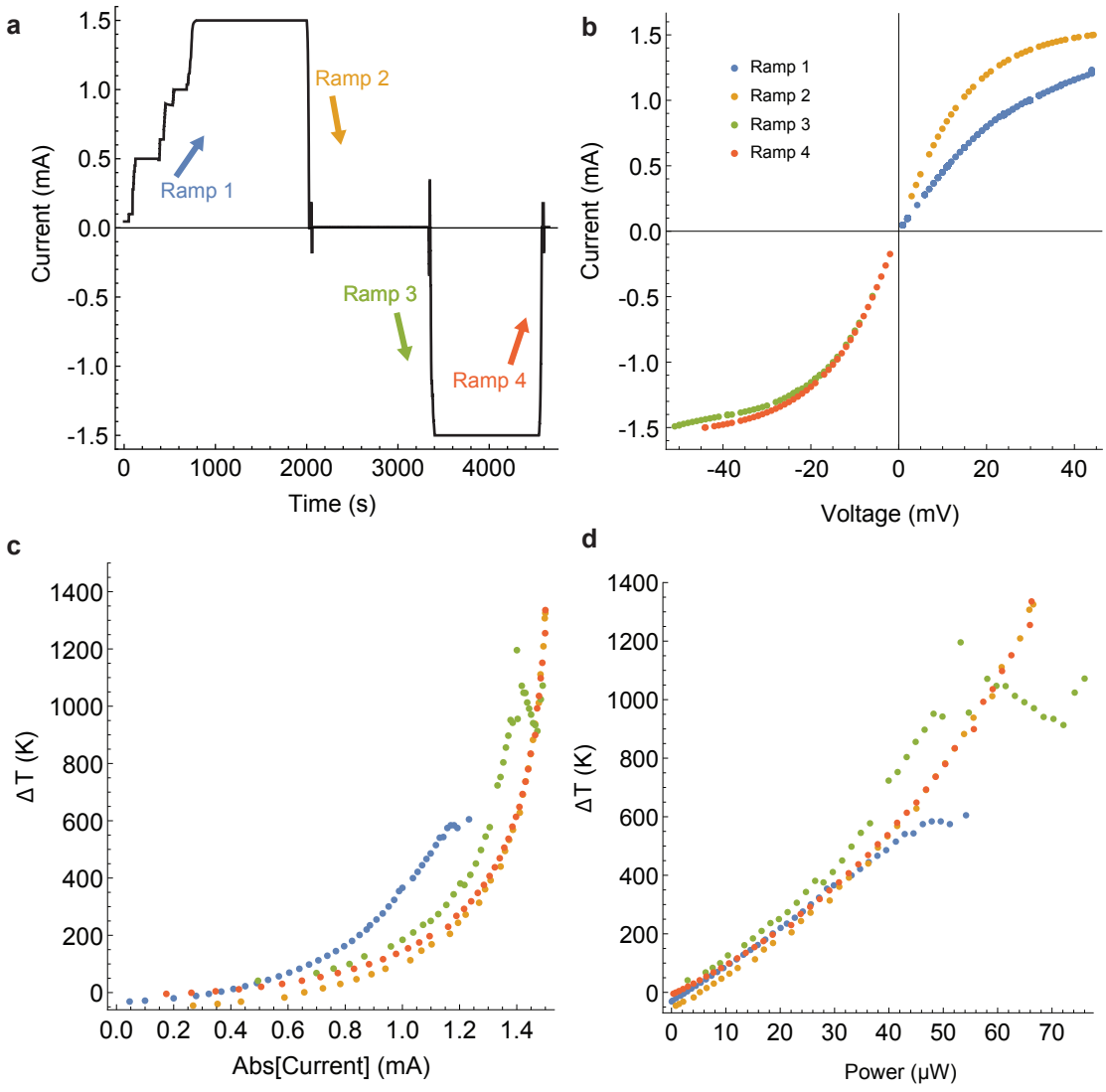

Figure 4.10: **4-wire transport data and temperature measurements in both polarities.** In this experiment a device is biased at 1.5 mA constant current in both polarities (a). 4-wire transport data is non-linear due to Joule heating (b). Using cobalt's TCR, temperature can be measured versus current (c) and power (d).

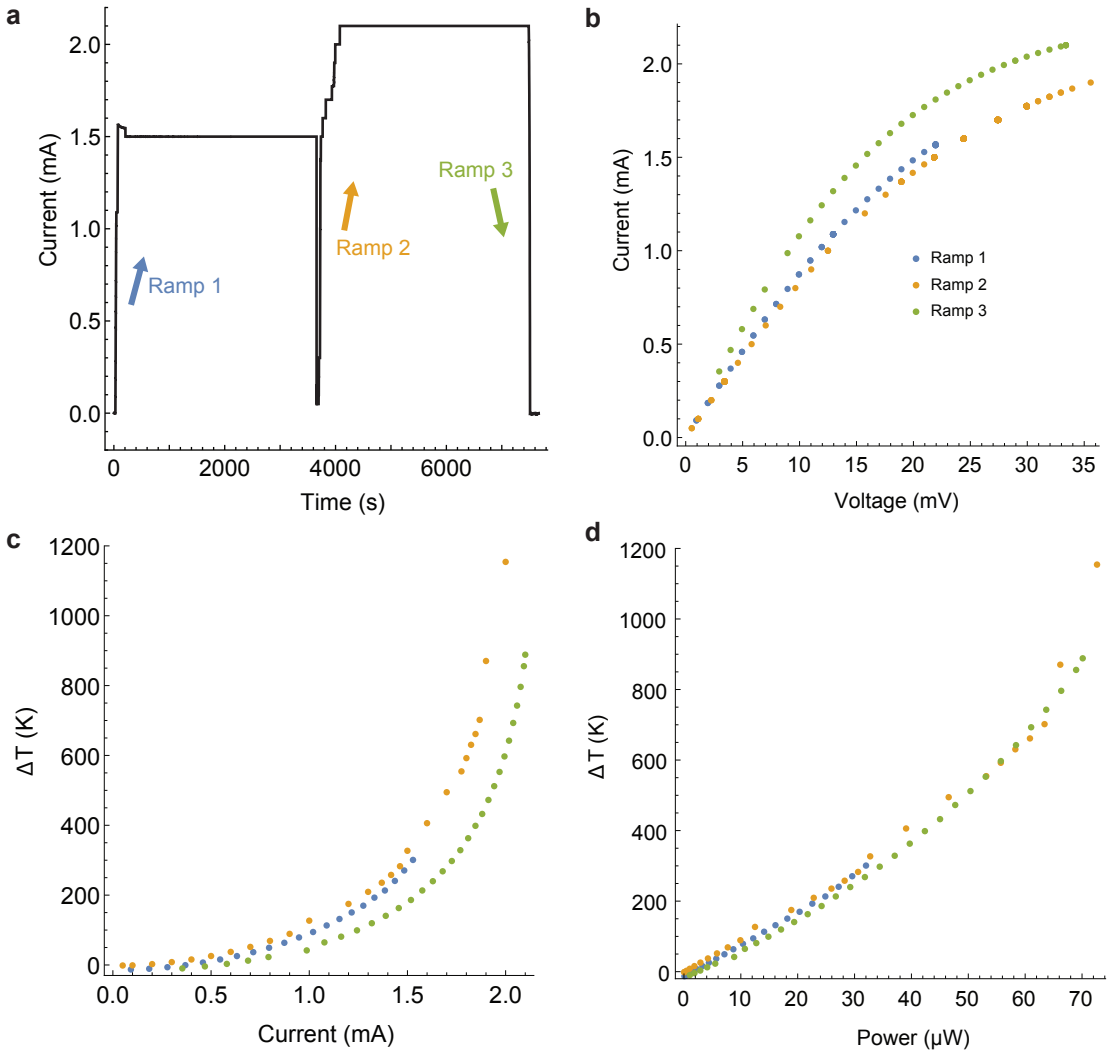

Figure 4.11: **4-wire transport data and temperature measurements in one polarity** In this experiment a device is biased at 1.5 mA then 2.1 ma constant current in one polarity (a). 4-wire transport data (b) is converted to temperature and plotted versus current (c) and power (d).

temperature of the wire is therefore proportional to power dissipated by Joule heating. The slight curving upward of the temperature change versus power plot of Fig. 4.7 d is likely due to a decrease in cobalt's thermal conductivity at high temperatures[73, 75], dictated by cobalt's temperature coefficient of thermal conductivity.

This method of measuring temperature through the TCR is not limited by statistical error since resistance can be measured to better than three digits. Systematic error is larger, evident by the variation in slope of the linear fits of temperature versus power of the four ramps (Fig. 4.7 d). Nominally, the slopes should be the same since the thermal conductivity of the nanowire is unlikely to change significantly between power ramps. The variations in slope are likely due to changes in resistance due to grain boundary growth which occur during the course of each ramp, which cannot be fully accounted for by measuring room-temperature resistance after ramp 2 and ramp 4. The linear fits of the four ramps have a mean slope of 8.6 ± 0.3 K/μW. This error bar is 4% of the mean, and sets the systematic error bar for this temperature measurement method. This accuracy is equal to or better than current state-of-the art commercially available *in situ* STEM heating chips.

We thus have two independent measurements of temperature at our disposal when performing *in situ* biasing experiments on cobalt nanowires. The temperature data (found through the multi-peak fitting algorithm) displayed in Fig. 4.7 corresponds to TCR transport data displayed in Fig. 4.10. The maximum change in temperature measured with PEET is 1000 ± 200 K. Although there are differences in temperature measured between the four ramps via the TCR method, Ramp 2 and Ramp 4 overlap closely, and a maximum change in temperature of ~ 1300 K is measured. The TCR-derived temperature nearly falls within the error bar of the PEET-derived temperature. At a maximum, the difference in best-estimate values implies a systematic difference of 30% between the two methods, which may be explained by imperfect subtraction of the silicon nitride background plasmon.

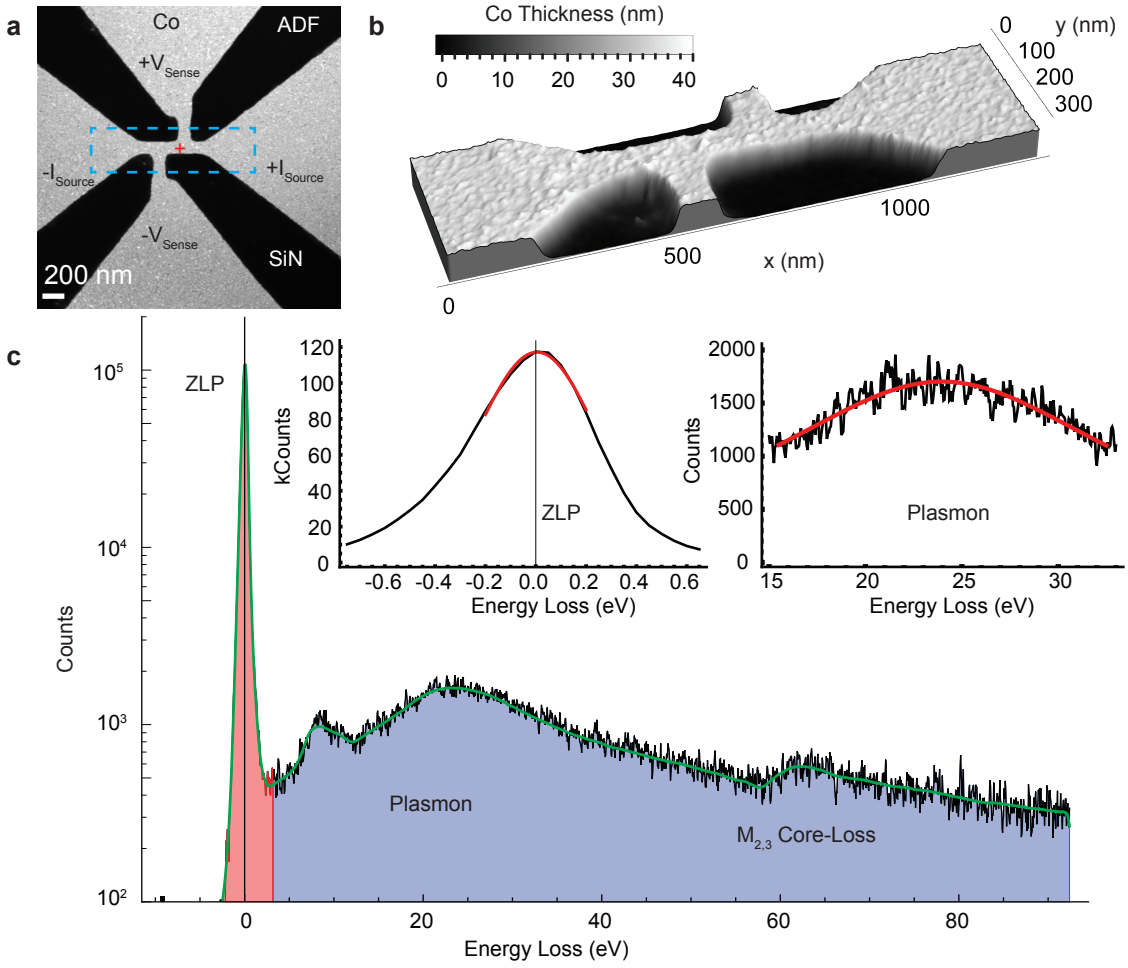

Figure 4.12: **Device architecture and EELS spectra.** A STEM ADF image of a cobalt nanowire supported on a silicon nitride membrane (a). A 3-D rendering of device thickness, measured with the EELS log-ratio method (b). An example EELS spectrum (c), taken from the pixel marked by the red cross in (a) shows the zero-loss peak, cobalt plasmon, and $M_{2,3}$ core-loss edge. A mean spectrum, taken from the right contact is superimposed in orange. The ZLP and plasmon peaks are fit with Gaussian and Lorentzian distributions, respectively (c, insets).

4.6 Electromigration-Driven Grain Growth in Cobalt Nanowires

Cobalt nanowires (30 nm thick, 100 nm wide) are patterned on electron-transparent (15 nm thick) in-house fabricated silicon nitride membranes (Fig. 4.12 a). The cobalt nanowires are designed to have a 4-wire geometry to allow for precise electrical transport data to be acquired from the center of the nanowire. EELS spectrum images are acquired from the dashed-blue region-of-interest (ROI). An example spectrum (Fig. 4.12 c), acquired from the location denoted by a red cross (Fig. 4.12 a), reveals the zero-loss peak (ZLP), the first plasmon and the $M_{2,3}$ core-loss excitation. The ZLP is fit to a Gaussian distribution, and the plasmon is fit to a Lorentzian distribution (Fig. 4.12 c, insets), and the plasmon energy is the difference in center values between the two fits.

EELS is a powerful quantitative technique which can be used to accurately measure thickness[46, 76] and density[66] of a material with nanometer spatial resolution. Thickness is commonly calculated through the log ratio method[46], which assumes plasmon generation is a Poisson process (Eq. 4.2).

In the sample spectrum displayed in Fig. 4.12 c, the counts in the blue shaded region are equal to I_1, and the counts under the red shaded region are equal to I_0. the The Poisson formula (Eq. 4.2) can be rearranged to yield thickness in terms of the plasmon generation mean free path: $t = \lambda I_1/I_T$. Using an 80 keV electron accelerating voltage, and a 20 mrad EELS collection angle, $\lambda = 59$ nm in cobalt films[76]. The log-ratio method yields precise out-of-plane measurements of thickness with high in-plane spatial resolution: A 3-dimensional rendering of thickness (Fig. 4.12 b) clearly shows sub-nm undulations in thickness due to the fine (~ 5 nm) grain structure of the cobalt nanowire.

Changes in thickness due to EM can be precisely mapped across the cobalt nanowire. Thickness is calculated from EELS spectrum-images, using the plasmon-ratio method. In this experiment multiple 15-minute EELS images are acquired with bias currents of (0, +1.5, 0, -1.5, 0, 2, 0, -2, 0 mA). As the biasing experiment progresses, changes in cobalt are displayed by averaging vertically over the width of the nanowire (Fig. 4.13 c). Changes in

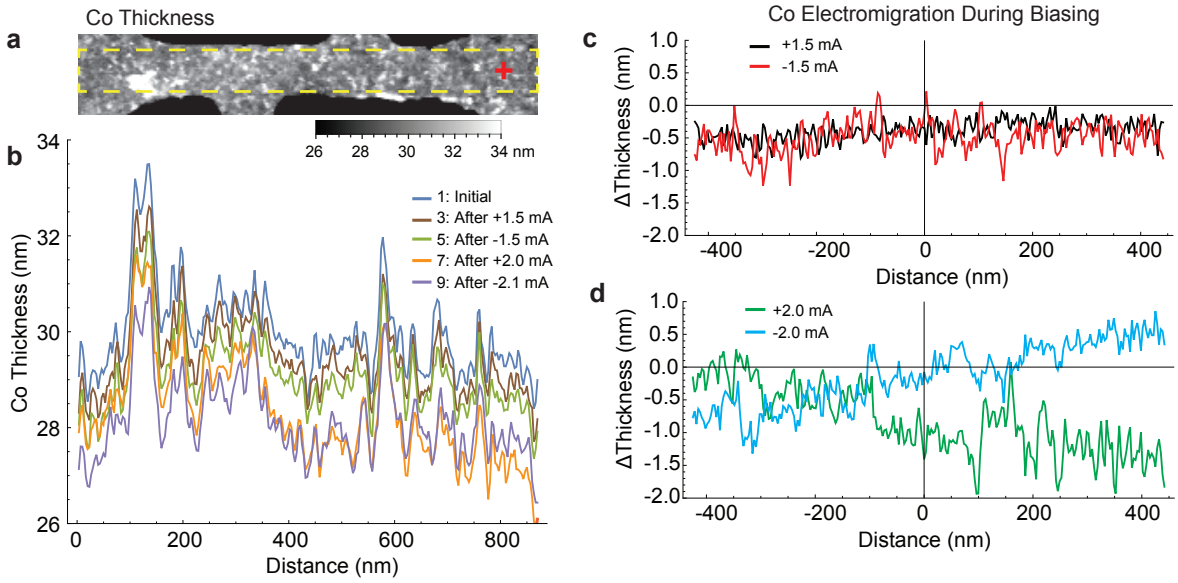

Figure 4.13: **Electromigration measured by EELS** The initial thickness of the cobalt nanowire is calculated with by the EELS log-ratio method. Thickness profiles (b), averaged vertically along the dashed-yellow box (a) are calculated after each 15 minute bias. Little cobalt moves at the 1.5 mA bias in either polarity (c). Greater amounts of cobalt are removed from the anode at 2.0 mA bias, in both bias polarities.

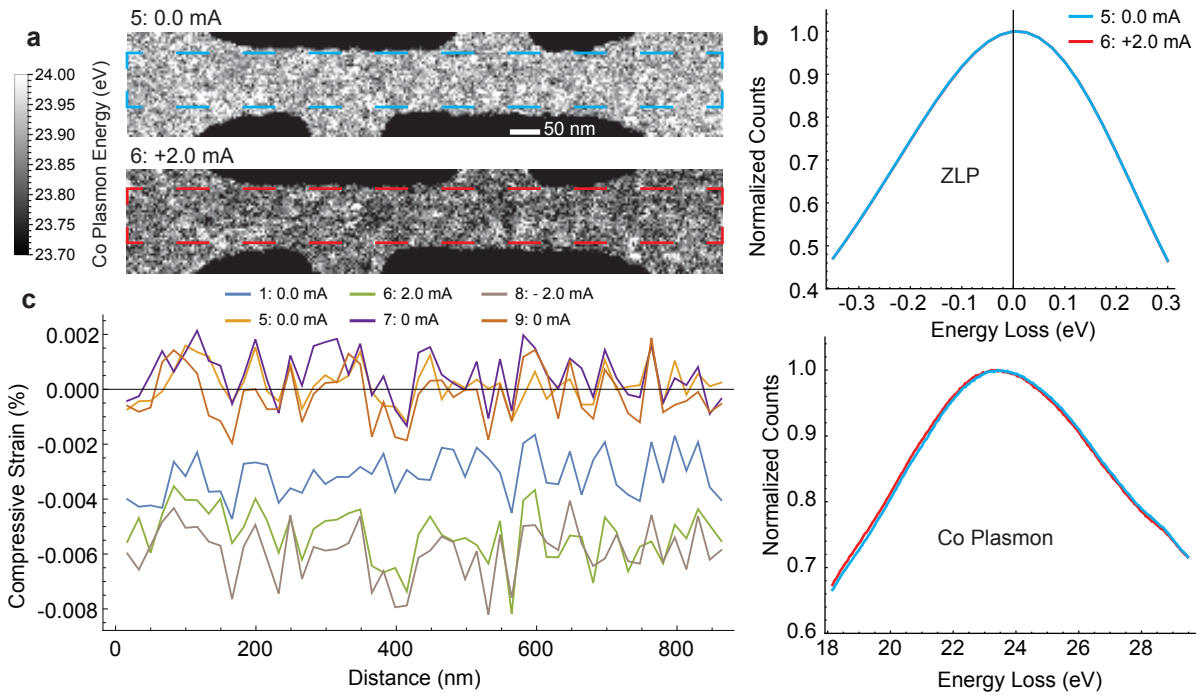

Figure 4.14: **Strain measurements across the nanowire.** Plasmon energy is mapped at 0.0 mA bias an 2.0 mA bias (a). A small shift in plasmon energy due to thermal expansion is barely visible by eye (b). Changes in plasmon energy are converted to strain, and vertically averaged over the dashed-blue and dashed-red ROI's (a) to yield line profiles (c). A tensile strain between the unbiased and biased data is due to thermal expansion of the cobalt lattice. A tensile strain between the as-deposited film subsequent unbiased data is due to a relaxation of strain in the as-deposited film[77].

thickness, calculated by subtracting an "off" image from the previous "off" image (Fig. 4.13 c), demonstrate that little cobalt is removed at 1.5 mA bias, but much larger amounts are removed at 2.0 mA bias (d). At both positive and negative 2.0 mA, cobalt is removed from the anode and deposited at the cathode, indicating the Z^* coefficient of this EM process is positive. These measured thickness changes are at their largest $\sim$ 1.5 nm, which is relatively small compared to the 30 nm thickness of the film.

Thickness measured by the log-ratio method cannot distinguish changes in thickness from changes in density, but cobalt density (and strain) can be measured directly through cobalt's

plasmon energy. If strain is isotropic in all three dimensions, $\Delta n/n \propto \epsilon^3$. Substituting this expression into the formula for plasmon energy (Eq. 4.4) yields an expression for strain: $\epsilon = 2\Delta E_p/3E_p$.

Cobalt plasmon energy is mapped, simultaneously with thickness, across each image in the experiment described in Fig. 4.13. Changes in plasmon energy are converted to strain, and plotted together (Fig. 4.14 c). The second and third "off" plasmon energy profiles overlap closely with each other, but are different than the as-grown plasmon energy. The cobalt film appears to be under significant compressive strain as-grown[77], which is quickly relaxed by Joule heating at the 1.5 mA bias. The plasmon energy measured when the wire is under positive or negative bias is nearly identical, and is significantly lower than the "off" plasmon energy due to thermal expansion of the cobalt lattice.

Thickness changes, measured directly via EELS, yield valuable EM information which is invisible in 4-wire electrical transport data. In a different experiment than shown in Fig. 4.13 and Fig. 4.9, a cobalt nanowire is biased at +1.5 mA for 60 mins, followed by +2.1 mA for 60 mins. Annular dark-field (ADF) images (Fig. 4.15 a, b, c) provide detailed maps of grain size within the polycrystalline wire. At the 1.5 mA bias, little change is visible in the crystal structure (Fig. 4.15 b), but at 2.1 mA bias, grain size increases dramatically (Fig. 4.15 b).

This increase in grain size is correlated with the cobalt hcp to fcc phase transition[77] at 380 °C. Indeed, the temperature (measured by the TCR method) at 1.5 mA bias current is 300 °C (Fig. 4.15 g), which is below this phase transition temperature, and the resistance of the nanowire increases slightly (5%) throughout the 60 min bias at this constant current. After scan 4, the current is increased in steps up to 2.1 mA, and the temperature increase due to Joule heating correspondingly increases. When the temperature of the wire surpasses 400 °C the resistance begins to decrease over time when held at constant current, which is an indication of grain-growth. When the bias is held at 2.1 mA for 60 mins the resistance of the nanowire decreases dramatically from from 19.0 Ω to 14.6 Ω, which is accompanied by a massive increase in grain size (Fig. 4.15 c). This grain growth results in fewer scattering

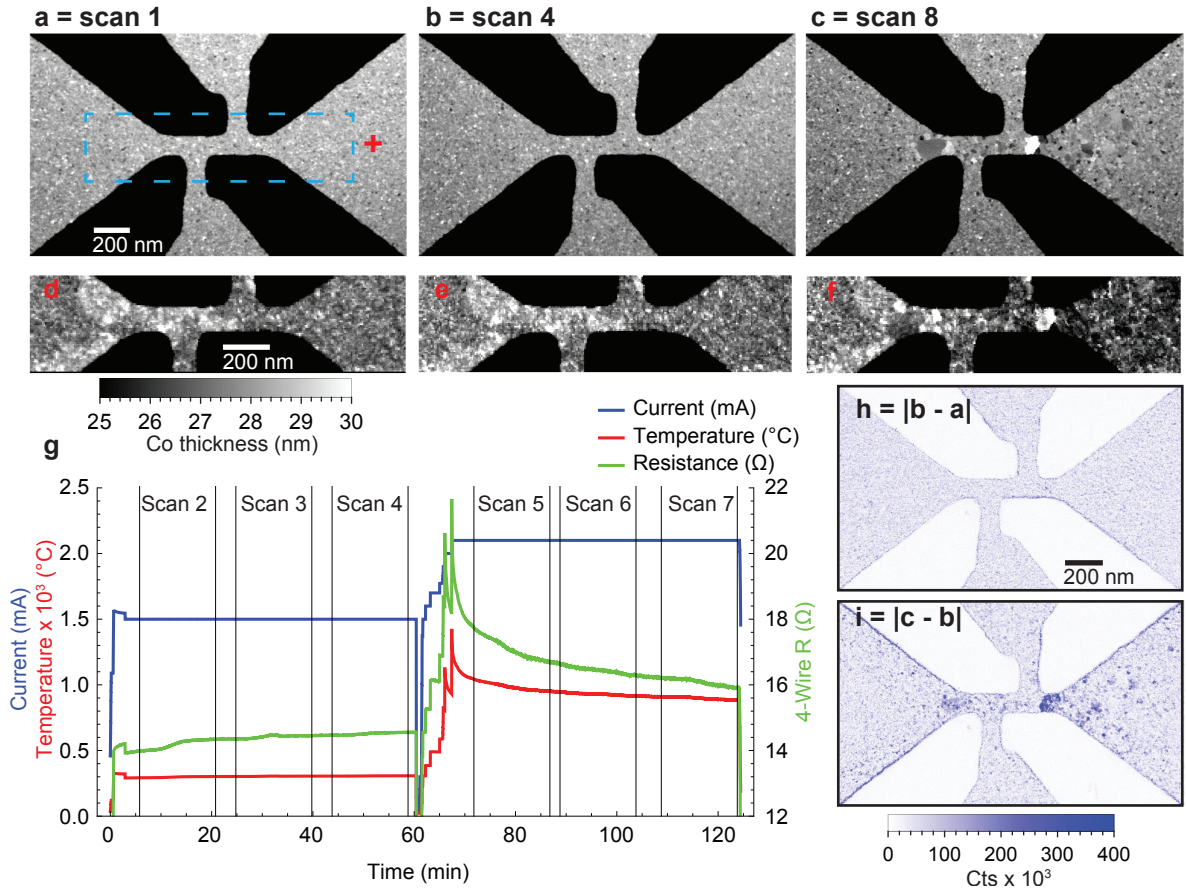

Figure 4.15: **Correlating 4-wire electrical transport to thickness changes.** ADF (a, b, c) and thickness (d, e, f) images taken before biasing (a,d), after 60 mins of 1.5 mA bias (a, e), and after 60 mins of 2.1 mA (a, f). Negligible change is observed in grain structure or thickness at 1.5 mA bias, but at 2.1 mA bias the grains grow dramatically and significant cobalt is removed from the anode. 4-wire data is acquired in real-time while the spectrum images are acquired (g), and temperature can be calculated via the TCR method. Resistance increases slightly during the 1.5 mA bias, and decreases dramatically during the 2.1 mA bias due to expanding grains (c). Absolute value difference images (h, i) demonstrate that grain growth occurs primarily on the anode of the device.

centers for charge carriers, which lowers the resistance of the nanowire.

Thickness maps (Fig. 4.15 d, e, f), calculated by the log-ratio method, show negligible changes at the 1.5 mA bias, and dramatic removal of cobalt on the anode after the 2.1 mA bias. The thickness of the anode decreases significantly at 2.1 mA bias, while the thickness of the cathode is almost unchanged. Depletion of metal on the anode of a wire is an indication of an EM process with a positive effective ionic charge ($+Z^*$). This EM signal is not indicated by transport data: EM will in general remove material, decreasing a device's cross section, and in turn increase its resistance. Yet in these devices resistance is dominated by grain size, and decreases dramatically as the device anneals due to Joule heating. ADF imaging channels are also a poor metric of thickness since they contain both inelastic and elastic scattering. EELS is a precise, high-resolution technique to directly measure thickness changes due to EM which are invisible by other techniques.

Similarly to EM, changes in grain structure are negligible at 1.5 mA, and are much larger on the anode at 2.1 mA bias. Changes in grain structure are mapped by taking difference images (Fig. 4.15 h, i) between the three ADF images (Fig. 4.15 a, b, c). At 2.1 mA bias, the nanowire is Joule to nearly 1000 °C, and changes in grain structure due to annealing are visible over the entire device. However, these changes in grain size are not symmetric across the center of the wire, and the anode has developed significantly larger grains than the cathode, which also extend over 500 nm away from the narrow section of the nanowire.

In a separate experiment a different cobalt nanowire is biased at alternating polarities and increasing current densities (Fig. 4.16). Changes in crystal structure are measured by mapping the squared difference (right column) of before (left column) and after (center column) ADF STEM images. The squared difference in ADF signal is chosen as a metric of grain growth, since grain growth can produce a positive or negative change in ADF signal, depending on the grain's crystal orientation. Thus the sign of the change in ADF signal is not as useful for detecting grain growth as the absolute value of the magnitude of the change in signal. For all four bias values (two magnitudes and two directions), significantly more grain growth is apparent on anode compared to the cathode. The results of this experiment

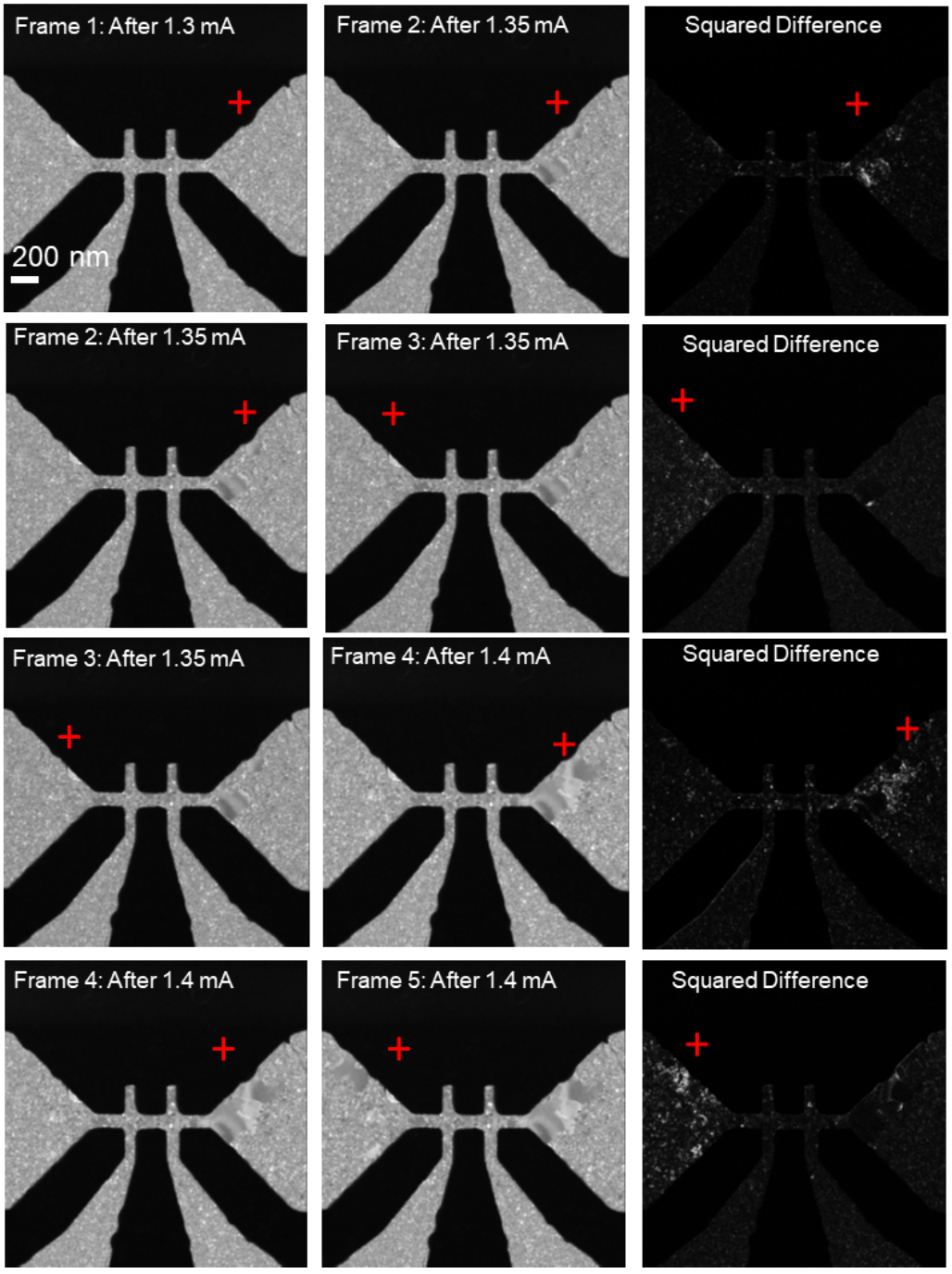

Figure 4.16: **Secondary grain growth induced by EM.** A cobalt device is biased in constant current mode, with forward and reverse bias at increasing current density. After each period of bias, the squared difference in before (left column) and after (center column) is taken (right column). Significantly more grain growth is visible on the anode in both bias polarities.

confirm that EM accelerates grain growth on the anode of the nanowire.

4.7 *Ex Situ* Analysis of Cobalt Grain Structure with Transmission Kikuchi Diffraction

The grain structure and texture of the polycrystalline cobalt nanowires can be analyzed with an SEM-based technique, transmisssion Kikuchi diffraction (TKD). TKD can map grain orientations, classify phases, among many other useful parameters[78]. It is closely related to the more common electron backscatter diffraction (EBSD) technique, but with a different detector angle. In EBSD the detector is located above the plane of the sample, and collects Kikuchi diffraction patterns from backscattered electrons. In TKD, the detector is located beneath the plane of the sample, and collects Kikuchi patterns from transmitted electrons. The primary practical difference between the two techniques is increased spatial resolution, which results from the smaller interaction volume with an electron-transparent sample in TKD. The spatial resolution of EBSD is limited to 20-50 nm, whereas in TKD spatial resolution is significantly below 10 nm[78]. All cobalt nanowire devices that are used for *in situ* STEM experiments are fabricated on electron-transparent silicon nitride windows, which allows them to be easily analyzed using TKD without any modification.

At high current densities, Joule heating induces a partial phase transition within the cobalt nanowires (Fig. 4.17). The hcp to fcc phase transition temperature [77] is 380 °C, indicating that Joule heating within the nanowire has surpassed that threshold. This phase map was acquired *ex situ* at room temperature, after biasing. The fact that the low-temperature hcp phase is not recovered at room temperature is surprising, but has been found to occur in thin-film cobalt by at least one other group[77].

The grain orientations of hcp grains are mapped simultaneously using Kikuchi patterns (Fig. 4.17). Pole figures of the hcp $< 0001 >$ orientation are generated from data taken within the left (cathode) and right (anode). The hcp $< 0001 >$ orientation of grains within the anode is better aligned to the out-of-plane direction compared to grains on the cathode.

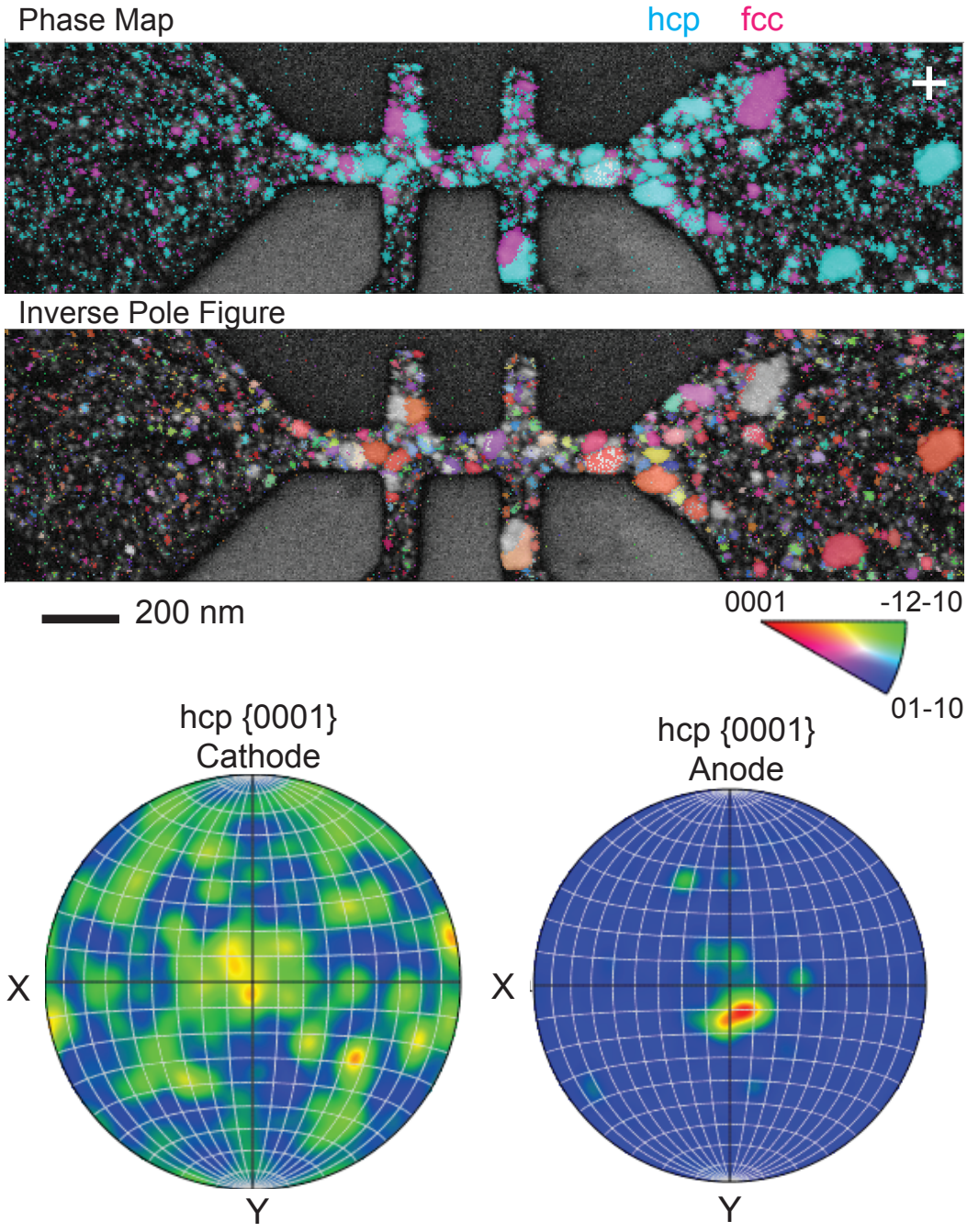

Figure 4.17: ***Ex-situ* TKD grain analysis of a biased cobalt nanowire.** Phase map (top) and inverse pole (center) figure of a cobalt nanowire that has been biased to a maximum current of 1.4 mA. The pole figures (bottom) reveal strong tendency for hcp grains to align with the 0001 direction normal to the film surface.

Not only are grains on the anode larger, but they are also better aligned along the $< 0001 >$ orientation.

4.8 Measurement of Effective Ionic Charge (Z^*) in Cobalt

For a given current density and temperature, it is possible to make an interconnect short enough so that a back-stress gradient cancels out electromigration[79]. This short-length (or Blech) effect is one of the most effective tools available to circuit designers to prolong the lifetime of short interconnects. The back-strain gradient induced by EM is directly proportional to the effective ionic charge (Z^*):

$$\frac{d\sigma}{dx} = \frac{2}{E_p}\frac{dE_p}{dx} = \frac{ej\rho Z^*}{3B\Omega B} \tag{4.11}$$

where b is a stress state-dependent coefficient, taken to be $b = 2/3$ for an equi-biaxial stress state[80], Ω is cobalt's atomic volume, and B is cobalt's bulk modulus of 190 GPa [81].

Changes in plasmon energy can be converted to changes in strain (Eq. 4.4). PEET assumes strains are thermally-induced, and converts them to temperature changes given a material's known coefficient of thermal expansion. As a function of position, thermally-induced strain will be parabolic. Superimposed on this thermal strain (due to Joule heating) is a linear strain due to EM, which is also bias-polarity dependent (Eq 4.11). Linear combinations of plasmon energy maps at positive, negative, and zero bias can be taken to cancel the thermal contribution and isolate the wind-force strain.

$$\frac{\Delta n_+}{n} = -\frac{Zej\rho\Delta x}{3\Omega B} - 3\alpha\Delta T \tag{4.12}$$

$$\frac{\Delta n_-}{n} = +\frac{Zej\rho\Delta x}{3\Omega B} - 3\alpha\Delta T \tag{4.13}$$

Where Δn_+ is the normalized difference in atomic density between the positive bias and zero bias images, and Δn_- is the normalized difference in atomic density between the

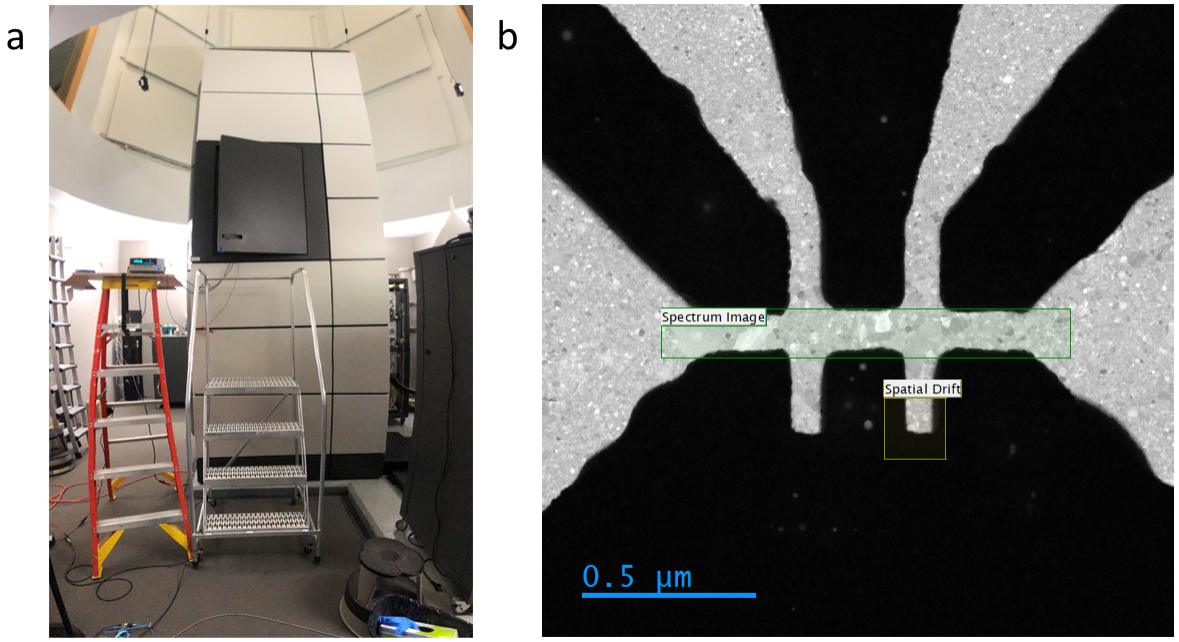

Figure 4.18: **TEAM 1.0 STEM equipped with a Gatan Continuum EELS spectrometer.** A photograph taken of the TEAM 1.0 probe-corrected STEM equipped with a high-speed Gatan Continuum EELS spectrometer, at LBNL's Molecular Foundry. The Keithley 2602 sourcemeter is visible atop the ladder, and sources current *in situ* to the cobalt nanowire via a Hummingbird biasing holder. An ADF STEM image (b) is acquired of a 4-wire cobalt nanowire device.

negative bias and zero bias images. The change plasmon energy is related to the change in atomic density simply: $\Delta n/n = 2\Delta E_p/E_p$. The temperature-induced strain is then:

$$\frac{1}{2}\left(\frac{\Delta n_-}{n} + \frac{\Delta n_-}{n}\right) = -3\alpha\Delta T \tag{4.14}$$

And correspondingly the wind-force induced strain is:

$$\frac{1}{2}\left(\frac{\Delta n_-}{n} + \frac{\Delta n_-}{n}\right) = -\frac{Zej\rho\Delta x}{3\Omega B} \tag{4.15}$$

To increase our signal-to-noise ratio, we acquire *in situ* biased cobalt nanowire data at the TEAM 1.0 probe-corrected electron microscope (Fig. 4.18 a) at the National Center for Electron Microscopy (NCEM) at Lawrence Berkeley National Laboratory (LBNL). This microscope is equipped with a Gatan Continuum EELS spectrometer, capable of acquiring 800 low-loss spectra per second. For comparison, the Gatan Quantum SE spectrometer at USC is only capable of approximately 20 spectra per second, or a factor of 40 slower. This instrument increases our signal-to-noise ratio in plasmon energy measurements by a factor of $\sqrt{40}$.

Due to the Continuum's high acquisition rate, plasmon energy maps (Fig. 4.19 b) can be acquired with 0.5 nm pixel size. Plasmon energy profiles are extracted by averaging vertically over the dashed-red ROI. Small areas of carbon contamination on the surface of the nanowire become visible in the plasmon energy map, because carbon's plasmon overlaps with cobalt's and introduces a shift upward in energy.

Grain boundaries in the nanowire are visible in the plasmon energy map (Fig. 4.20 a), a testament to the spatial resolution of plasmon energy mapping. Within ~ 5 nm of a grain boundary, the plasmon energy decreases relative to the center of a grain. This is because the cobalt lattice is no longer close-packed within a grain boundary (Fig. 4.20 c), and thus the local atomic density (and plasmon energy) decreases. Notably, the plasmon energy dip is wider (~ 5 nm) than the physical extent of a grain boundary (an atom wide). The blurring of the grain boundary in the plasmon energy map is due to plasmon delocalization, and is

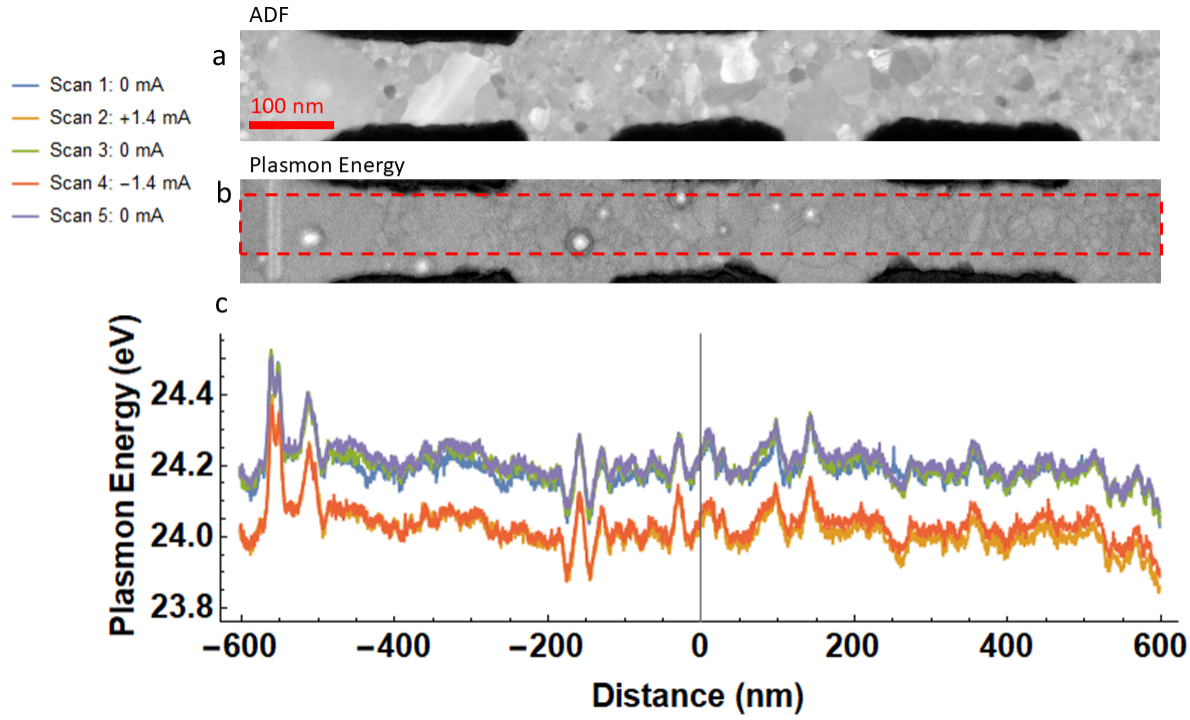

Figure 4.19: **Plasmon energy maps acquired on a Continuum EELS spectrometer.** ADF (a) and plasmon energy maps (b) are acquired over the narrow section of a cobalt nanowire. Plasmon energy is vertically averaged over the red ROI (b) and plotted (c).

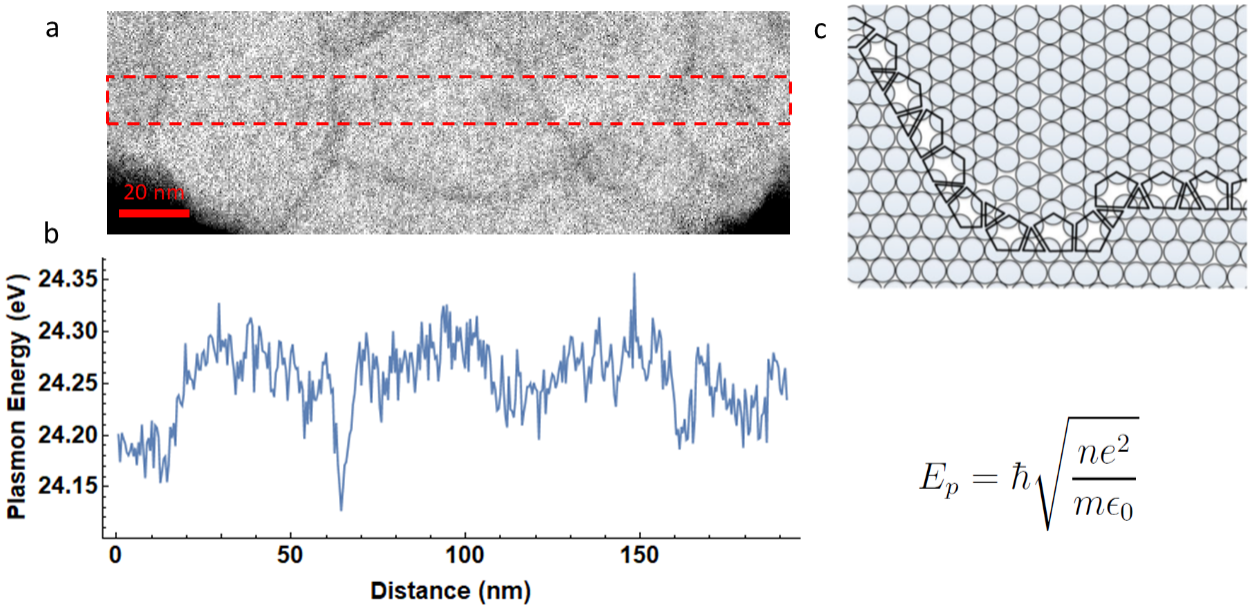

Figure 4.20: **Changes in plasmon energy due to grain boundaries**. The step size (0.5 nm) is small enough in the plasmon energy map (a) to resolve decreases in density due to grain boundaries. The density of cobalt is decreased at a grain boundary due to imperfect atomic packing (c). Panel (c) is reproduced from [82].

an indication of the spatial resolution of plasmon-based strain mapping.

The average temperature at +1.40 mA and −1.40 mA bias is mapped along the length of the nanowire (Fig. 4.21). Compared to data acquired on the Quantum SE (Fig. 4.7), the signal-to-noise ratio of the temperature measurements is dramatically improved. The temperature profile can be fit to a quadratic function (red line), but is nearly uniform across the length of the nanowire. Joule heating raises the temperature of the nanowire by $\Delta T = 380 \pm 20$ K.

Pressure due to the wind force is plotted across the length of the nanowire (Fig. 4.22). Although somewhat noisy, a clear pressure gradient is visible, and can be fit well to a line (red overlay). This pressure gradient of 680 kPa/nm corresponds to a $Z^* = +0.62 \pm 0.09$. The magnitude of this measurement is nearly an factor of three smaller than the $Z^* = +1.6$

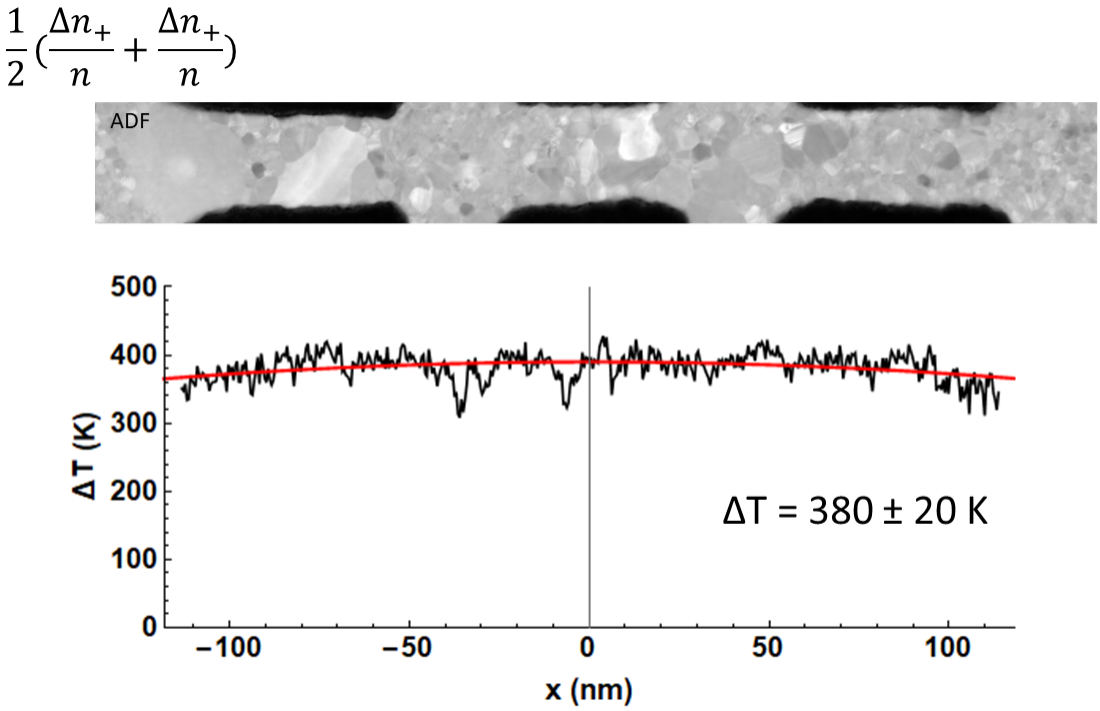

Figure 4.21: **Temperature measurement in a cobalt nanowire with a Continuum EELS spectrometer.** The average temperature is plotted between the positive and negative 1.4 mA bias. The signal-to-noise ratio is visibly better than previous data acquired on a Quantum SE spectrometer.

$$\frac{1}{2}\left(\frac{\Delta n_+}{n} - \frac{\Delta n_+}{n}\right)$$

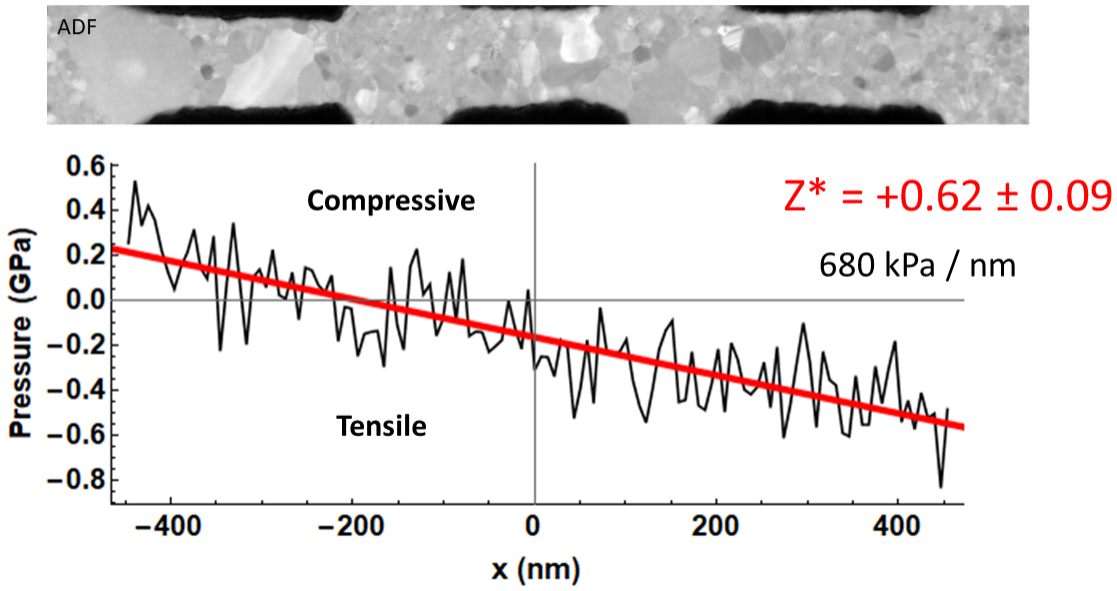

Figure 4.22: **Maps of electromigration-induced pressure.** Pressure due to the electron wind force is plotted versus position along the nanowire axis. A Z^* of $+0.62 \pm 0.09$ is extracted from this data.

measured by Ho[63] at 1300 °C. This discrepancy is possibly due to a significant difference in temperature at which the two experiments were performed.

A significant tensile strain of ~ 500 MPa is measured on the anode of the nanowire. This tensile strain may explain the asymmetric grain growth described earlier in this chapter (Fig. 4.16). Cobalt has been found[83] in *in situ* TEM stressing experiments to evolve larger grains under tensile stress. Here, instead of mechanically inducing tensile stress, we induce tensile stress with a high current density. This control of grain growth with an electronic current is a unique feature of these cobalt nanowires which may allow engineering of larger grains with lower resistivity, and in turn higher EM resistance.

CHAPTER 5

Conclusion

In this dissertation we further expand on quantitative STEM techniques like EBIC and EELS to probe electrically-active defects *in situ* . EBIC, normally an SEM-based technique, is applied to electron-transparent GaAs nanowire devices using a STEM biasing holder. The spatial distribution of e-h generation, the fundamental limit to EBIC's spatial resolution, is measured directly. The narrow, cylindrical e-h generation function is measured to have a radial decay length of 12.8 ± 0.2 nm, which allows order-of-magnitude higher-resolution EBIC than is achievable with SEM EBIC.

By raising the accelerating voltage of the STEM above the knock-on damage threshold of GaAs, we converted the STEM to a highly-precise source of β radiation. Vacancy-interstitial defects introduced by the primary beam were found to function as effective recombination centers, reducing the charge-collection efficiency, and in turn EBIC, of the heterojunction devices. By recording abrupt drops in EBIC as the beam is rastering, individual insertion events can be located with single-pixel (sub nm) precision. We expect this new EBIC capability will open the door to high-resolution studies of radiation sensitivity within nanoscale semiconductor devices.

Electromigration is a critical source of failure in nanoscale interconnect, and we have developed new techniques based on EELS characterize EM within cobalt. Cobalt is a next-generation interconnect material, and is highly resistant to EM, compared to the now-standard copper. EELS provides highly-precise (sub-nm) out-of-plane thickness measurements, and has been implemented *in situ* to measure small thickness changes induced by EM within cobalt nanowires. The superior thickness precision of EELS relative to HAADF

has been critical to characterizing EM within these nanowires, since cobalt is highly resistant to EM and little material moves on the few-hour timescale possible for *in situ* TEM experiments.

Converting changes in cobalt's plasmon energy to strain yields measurements of temperature changes from Joule heating. A gradient in strain is found within a nanowire under bias, allowing for the magnitude of the effective ionic charge can be measured ($Z^* = +0.62 \pm 0.09$).

Conventional ADF STEM movies acquired in-situ demonstrate clear influence of EM on secondary grain growth. Grains on the anode are consistently larger than grains on the cathode of cobalt nanowires. This effect is likely due to the electromigration-induced buildup of tensile strain on the anode of the nanowire. Larger grains lower the resistivity of a nanowire, and in turn increase its EM resistance. It may be possible to exploit this property of cobalt to engineer larger grains within cobalt nanowires.

REFERENCES

[1] P. W. Hawkes, "Ernst Ruska," *Physics Today*, vol. 43, p. 84, Jan. 2008. Publisher: American Institute of PhysicsAIP.

[2] L. Reimer and H. Kohl, *Transmission Electron Microscopy*. Springer, fifth ed., 2008. p. 170.

[3] D. Williams and B. Carter, *Transmission Electron Microscopy*. Springer, 2009.

[4] S. J. Pennycook, "The impact of STEM aberration correction on materials science," *Ultramicroscopy*, vol. 180, pp. 22–33, Sept. 2017.

[5] B. Zutter, H. Kim, W. Hubbard, D. Ren, M. Mecklenburg, D. Huffaker, and B. C. Regan, "Mapping Charge Recombination and the Effect of Point Defect Insertion in Gallium Arsenide Nanowire Heterojunctions," *arXiv:2010.05140 [cond-mat]*, Oct. 2020. arXiv: 2010.05140.

[6] R. Egerton, *Electron Energy-Loss Spectroscopy in the Electron Microscope*. Springer, 3rd ed., 2011.

[7] A. Rothwarf, "Plasmon theory of electron-hole pair production: efficiency of cathode ray phosphors," *Journal of Applied Physics*, vol. 44, pp. 752–756, Feb. 1973.

[8] W. A. Hubbard, *Visualizing the Invisible in Functioning Nanoelectronic Devices*. PhD thesis, UCLA, 2017.

[9] E. R. White, J. J. Lodico, and B. C. Regan, "Intercalation events visualized in single microcrystals of graphite," *Nature Communications*, vol. 8, p. 1969, Dec. 2017.

[10] J. J. Lodico, *Fingerprinting electrode-electrolyte interfaces and intercalant kinematics in flake graphite*. PhD thesis, UCLA, 2019.

[11] T. E. Everhart and P. H. Hoff, "Determination of Kilovolt Electron Energy Dissipation vs Penetration Distance in Solid Materials," *Journal of Applied Physics*, vol. 42, pp. 5837–5846, Dec. 1971.

[12] H. J. Leamy, "Charge collection scanning electron microscopy," *Journal of Applied Physics*, vol. 53, pp. R51–R80, June 1982.

[13] T. Everhart, O. Wells, and R. Matta, "A novel method of semiconductor device measurements," *Proceedings of the IEEE*, vol. 52, pp. 1642–1647, Dec. 1964. Conference Name: Proceedings of the IEEE.

[14] L. Reimer, *Scanning Electron Microscopy*. Springer-Verlag, second ed., 1998.

[15] A. Howie, "Recent developments in secondary electron imaging," *Journal of Microscopy*, vol. 180, no. 3, pp. 192–203, 1995. _eprint: https://onlinelibrary.wiley.com/doi/pdf/10.1111/j.1365-2818.1995.tb03678.x.

[16] M. Kociak and L. F. Zagonel, "Cathodoluminescence in the scanning transmission electron microscope," *Ultramicroscopy*, vol. 176, pp. 112–131, May 2017.

[17] C. Donolato, "Contrast and resolution of SEM charge-collection images of dislocations," *Applied Physics Letters*, vol. 34, pp. 80–81, Jan. 1979. Publisher: American Institute of Physics.

[18] N. I. of Standards and Technology, "ESTAR Stopping Power and Range Tables for Electrons," 2020.

[19] C. Gutsche, R. Niepelt, M. Gnauck, A. Lysov, W. Prost, C. Ronning, and F.-J. Tegude, "Direct Determination of Minority Carrier Diffusion Lengths at Axial GaAs Nanowire p–n Junctions," *Nano Letters*, vol. 12, pp. 1453–1458, Mar. 2012. Publisher: American Chemical Society.

[20] J. E. Allen, E. R. Hemesath, D. E. Perea, J. L. Lensch-Falk, Z. Y. Li, F. Yin, M. H. Gass, P. Wang, A. L. Bleloch, R. E. Palmer, and L. J. Lauhon, "High-resolution detection of Au catalyst atoms in Si nanowires," *Nature Nanotechnology*, vol. 3, pp. 168–173, Mar. 2008.

[21] M. B. Panish, "Ternary Condensed Phase Systems of Gallium and Arsenic with Group lB Elements," *Journal of The Electrochemical Society*, vol. 114, pp. 516–521, May 1967.

[22] V. T. Fauske, J. Huh, G. Divitini, D. L. Dheeraj, A. M. Munshi, C. Ducati, H. Weman, B.-O. Fimland, and A. T. J. van Helvoort, "In Situ Heat-Induced Replacement of GaAs Nanowires by Au," *Nano Letters*, vol. 16, pp. 3051–3057, May 2016.

[23] M. Orrù, S. Rubini, and S. Roddaro, "Formation of axial metal–semiconductor junctions in GaAs nanowires by thermal annealing," *Semiconductor Science and Technology*, vol. 29, no. 5, p. 054001, 2014.

[24] S. M. Sze and J. C. Irvin, "Resistivity, mobility and impurity levels in GaAs, Ge, and Si at 300K," *Solid-State Electronics*, vol. 11, pp. 599–602, June 1968.

[25] A. Johnston, *Reliability and Radiation Effects in Compound Semiconductors*. Singapore: World Scientific, 2010.

[26] M. McCluskey, *Dopants and Defects in Semiconductors*. Boca Raton, FL: Taylor & Francis Group, second edition ed., 2018.

[27] E. Hieckmann, M. Nacke, M. Allardt, Y. Bodrov, P. Chekhonin, W. Skrotzki, and J. Weber, "Comprehensive Characterization of Extended Defects in Semiconductor Materials by a Scanning Electron Microscope," *JoVE (Journal of Visualized Experiments)*, p. e53872, May 2016.

[28] J. R. Srour and J. W. Palko, "Displacement Damage Effects in Irradiated Semiconductor Devices," *IEEE Transactions on Nuclear Science*, vol. 60, pp. 1740–1766, June 2013. Conference Name: IEEE Transactions on Nuclear Science.

[29] F. Li, Z. Li, L. Tan, Y. Zhou, J. Ma, M. Lysevych, L. Fu, H. H. Tan, and C. Jagadish, "Radiation effects on GaAs/AlGaAs core/shell ensemble nanowires and nanowire infrared photodetectors," *Nanotechnology*, vol. 28, p. 125702, Feb. 2017. Publisher: IOP Publishing.

[30] L. C. Hirst, M. K. Yakes, J. H. Warner, M. F. Bennett, K. J. Schmieder, R. J. Walters, and P. P. Jenkins, "Intrinsic radiation tolerance of ultra-thin GaAs solar cells," *Applied Physics Letters*, vol. 109, p. 033908, July 2016. Publisher: American Institute of Physics.

[31] C. O. Thomas, D. Kahng, and R. C. Manz, "Impurity Distribution in Epitaxial Silicon Films," *Journal of The Electrochemical Society*, vol. 109, pp. 1055–1061, Nov. 1962.

[32] D. V. Lang, "Deep-level transient spectroscopy: A new method to characterize traps in semiconductors," *Journal of Applied Physics*, vol. 45, pp. 3023–3032, July 1974.

[33] J. H. Warner, S. R. Messenger, R. J. Walters, G. P. Summers, M. J. Romero, and E. A. Burke, "Displacement Damage Evolution in GaAs Following Electron, Proton and Silicon Ion Irradiation," *IEEE Transactions on Nuclear Science*, vol. 54, pp. 1961–1968, Dec. 2007. Conference Name: IEEE Transactions on Nuclear Science.

[34] V. Naumann, D. Lausch, A. Hähnel, J. Bauer, O. Breitenstein, A. Graff, M. Werner, S. Swatek, S. Großer, J. Bagdahn, and C. Hagendorf, "Explanation of potential-induced degradation of the shunting type by Na decoration of stacking faults in Si solar cells," *Solar Energy Materials and Solar Cells*, vol. 120, pp. 383–389, Jan. 2014.

[35] D. Ban, E. H. Sargent, S. J. Dixon-Warren, I. Calder, A. J. SpringThorpe, R. Dworschak, G. Este, and J. K. White, "Direct imaging of the depletion region of an InP p–n junction under bias using scanning voltage microscopy," *Applied Physics Letters*, vol. 81, pp. 5057–5059, Dec. 2002.

[36] C.-C. Chang, C.-Y. Chi, M. Yao, N. Huang, C.-C. Chen, J. Theiss, A. W. Bushmaker, S. LaLumondiere, T.-W. Yeh, M. L. Povinelli, C. Zhou, P. D. Dapkus, and S. B. Cronin, "Electrical and Optical Characterization of Surface Passivation in GaAs Nanowires," *Nano Letters*, vol. 12, pp. 4484–4489, Sept. 2012.

[37] E. R. White, A. Kerelsky, W. A. Hubbard, R. Dhall, S. B. Cronin, M. Mecklenburg, and B. C. Regan, "Imaging interfacial electrical transport in graphene–MoS2 heterostructures with electron-beam-induced-currents," *Applied Physics Letters*, vol. 107, p. 223104, Nov. 2015.

[38] J. D. Poplawsky, C. Li, N. R. Paudel, W. Guo, Y. Yan, and S. J. Pennycook, "Nanoscale doping profiles within CdTe grain boundaries and at the CdS/CdTe interface revealed by atom probe tomography and STEM EBIC," *Solar Energy Materials and Solar Cells*, vol. 150, pp. 95–101, June 2016.

[39] M.-G. Han, M. S. J. Marshall, L. Wu, M. A. Schofield, T. Aoki, R. Twesten, J. Hoffman, F. J. Walker, C. H. Ahn, and Y. Zhu, "Interface-induced nonswitchable domains in ferroelectric thin films," *Nature Communications*, vol. 5, p. 4693, Aug. 2014.

[40] Z. Warecki, V. Oleshko, K. Celio, A. Armstrong, A. Allerman, A. A. Talin, and J. Cumings, "Measuring the minority carrier diffusion length in n-GaN using bulk STEM EBIC," *Microscopy and Microanalysis*, vol. 24, pp. 1842–1843, Aug. 2018. Publisher: Cambridge University Press.

[41] W. A. Hubbard, M. Mecklenburg, H. L. Chan, and B. C. Regan, "STEM Imaging with Beam-Induced Hole and Secondary Electron Currents," *Physical Review Applied*, vol. 10, p. 044066, Oct. 2018.

[42] M. Mecklenburg, W. A. Hubbard, J. J. Lodico, and B. C. Regan, "Electron beam-induced current imaging with two-angstrom resolution," *Ultramicroscopy*, p. 112852, Oct. 2019.

[43] K. A. Dick, C. Thelander, L. Samuelson, and P. Caroff, "Crystal Phase Engineering in Single InAs Nanowires," *Nano Letters*, vol. 10, pp. 3494–3499, Sept. 2010. Publisher: American Chemical Society.

[44] D. Rudolph, S. Funk, M. Doblinger, S. Morkotter, S. Hertenberger, L. Schweickert, J. Becker, S. Matich, M. Bichler, D. Spirkoska, I. Zardo, J. J. Finley, G. Abstreiter, and G. Koblmüller, "Spontaneous Alloy Composition Ordering in GaAs-AlGaAs Core–Shell Nanowires," *Nano Letters*, vol. 13, pp. 1522–1527, Apr. 2013. Publisher: American Chemical Society.

[45] M. Nichterwitz and T. Unold, "Numerical simulation of cross section electron-beam induced current in thin-film solar-cells for low and high injection conditions," *Journal of Applied Physics*, vol. 114, p. 134504, Oct. 2013.

[46] R. F. Egerton, "Electron energy-loss spectroscopy in the TEM," *Reports on Progress in Physics*, vol. 72, no. 1, p. 016502, 2009.

[47] A. Pillukat, K. Karsten, and P. Ehrhart, "Point defects and their reactions in e-irradiated GaAs investigated by x-ray-diffraction methods," *Physical Review B*, vol. 53, pp. 7823–7835, Mar. 1996. Publisher: American Physical Society.

[48] K. Nordlund, J. Peltola, J. Nord, J. Keinonen, and R. S. Averback, "Defect clustering during ion irradiation of GaAs: Insight from molecular dynamics simulations," *Journal of Applied Physics*, vol. 90, pp. 1710–1717, Aug. 2001.

[49] N. Chen, S. Gray, E. Hernandez-Rivera, D. Huang, P. D. LeVan, and F. Gao, "Computational simulation of threshold displacement energies of GaAs," *Journal of Materials Research*, vol. 32, pp. 1555–1562, Apr. 2017. Publisher: Cambridge University Press.

[50] L. W. Aukerman and R. D. Graft, "Annealing of Electron-Irradiated GaAs," *Physical Review*, vol. 127, pp. 1576–1583, Sept. 1962.

[51] C. Ophus, "Four-Dimensional Scanning Transmission Electron Microscopy (4D-STEM): From Scanning Nanodiffraction to Ptychography and Beyond," *Microscopy and Microanalysis*, vol. 25, pp. 563–582, June 2019. Publisher: Cambridge University Press.

[52] Y. Fan, S. B. Singer, R. Bergstrom, and B. C. Regan, "Probing Planck's Law with Incandescent Light Emission from a Single Carbon Nanotube," *Physical Review Letters*, vol. 102, p. 187402, May 2009. Publisher: American Physical Society.

[53] M. Mecklenburg, W. A. Hubbard, E. R. White, R. Dhall, S. B. Cronin, S. Aloni, and B. C. Regan, "Nanoscale temperature mapping in operating microelectronic devices," *Science*, vol. 347, pp. 629–632, Feb. 2015.

[54] K. N. Tu, "Recent advances on electromigration in very-large-scale-integration of interconnects," *Journal of Applied Physics*, vol. 94, pp. 5451–5473, Oct. 2003. Publisher: American Institute of Physics.

[55] F. Griggio, J. Palmer, F. Pan, N. Toledo, A. Schmitz, I. Tsameret, R. Kasim, G. Leatherman, J. Hicks, A. Madhavan, J. Shin, J. Steigerwald, A. Yeoh, and C. Auth, "Reliability of dual-damascene local interconnects featuring cobalt on 10 nm logic technology," in *2018 IEEE International Reliability Physics Symposium (IRPS)*, pp. 6E.3–1–6E.3–5, Mar. 2018. ISSN: 1938-1891.

[56] J. S. Clarke, C. George, C. Jezewski, A. M. Caro, D. Michalak, and J. Torres, "Process technology scaling in an increasingly interconnect dominated world," in *2014 Symposium on VLSI Technology (VLSI-Technology): Digest of Technical Papers*, pp. 1–2, June 2014. ISSN: 2158-9682.

[57] R. Gusley, K. Sentosun, S. Ezzat, K. R. Coffey, A. C. West, and K. Barmak, "Electrodeposition of Epitaxial Co on Ru(0001)/Al2O3(0001)," *Journal of The Electrochemical Society*, vol. 166, p. D875, Nov. 2019. Publisher: IOP Publishing.

[58] M. H. van der Veen, N. Heyler, O. V. Pedreira, I. Ciofi, S. Decoster, V. V. Gonzalez, N. Jourdan, H. Struyf, K. Croes, C. J. Wilson, and Z. Tőkei, "Damascene Benchmark of Ru, Co and Cu in Scaled Dimensions," in *2018 IEEE International Interconnect Technology Conference (IITC)*, pp. 172–174, June 2018. ISSN: 2380-6338.

[59] D. Gall, "Electron mean free path in elemental metals," *Journal of Applied Physics*, vol. 119, p. 085101, Feb. 2016. Publisher: American Institute of Physics.

[60] E. Milosevic, S. Kerdsongpanya, M. E. McGahay, A. Zangiabadi, K. Barmak, and D. Gall, "Resistivity scaling and electron surface scattering in epitaxial Co(0001) layers," *Journal of Applied Physics*, vol. 125, p. 245105, June 2019. Publisher: American Institute of Physics.

[61] I. A. Blech and E. S. Meieran, "Electromigration in Thin Al Films," *Journal of Applied Physics*, vol. 40, pp. 485–491, Feb. 1969.

[62] B. Engler and R. Hull, "Accelerated Electromigration Study of Cobalt Thin Films by In-Situ TEM," *Microscopy and Microanalysis*, vol. 25, pp. 1902–1903, Aug. 2019.

[63] P. S. Ho, "Electromigration and soret effect in cobalt," *Journal of Physics and Chemistry of Solids*, vol. 27, pp. 1331–1338, Aug. 1966.

[64] G. J. van Gurp, "Electromigration and Hall effect in cobalt films," *Journal of Physics and Chemistry of Solids*, vol. 38, pp. 627–633, Jan. 1977.

[65] J. J. B. Prasad and K. V. Reddy, "Lateral self-diffusion and electromigration in cobalt thin films," *Journal of Physics D: Applied Physics*, vol. 17, pp. 125–133, Jan. 1984. Publisher: IOP Publishing.

[66] M. Mecklenburg, B. Zutter, and B. Regan, "Thermometry of Silicon Nanoparticles," *Physical Review Applied*, vol. 9, p. 014005, Jan. 2018.

[67] L. Shen, M. Mecklenburg, R. Dhall, B. C. Regan, and S. B. Cronin, "Measuring nanoscale thermal gradients in suspended MoS2 with STEM-EELS," *Applied Physics Letters*, vol. 115, p. 153108, Oct. 2019.

[68] B. Zutter, M. Mecklenburg, and B. C. Regan, "Temperature Dependence of the Silicon Nitride Volume Plasmon," *Microscopy and Microanalysis; Cambridge*, vol. 22, pp. 1574–1575, July 2016.

[69] W. A. Hubbard, M. Mecklenburg, J. J. Lodico, Y. Chen, X. Y. Ling, R. Patil, W. A. Kessel, G. J. K. Flatt, H. L. Chan, B. Vareskic, G. Bal, B. Zutter, and B. C. Regan, "Electron-Transparent Thermoelectric Coolers Demonstrated with Nanoparticle and Condensation Thermometry," *ACS Nano*, vol. 14, pp. 11510–11517, Sept. 2020. Publisher: American Chemical Society.

[70] Y. Kasamatsu, M. Koyama, K.-i. Masumoto, K.-i. Kojima, T. Hihara, and T. Kamigaichi, "Dilatometric Measurement of the Thermal Expansion of Cobalt Single Crystal," *Japanese Journal of Applied Physics*, vol. 20, p. 37, Jan. 1981. Publisher: IOP Publishing.

[71] Q. Cai, Y.-C. Chen, C. Tsai, and J. F. DeNatale, "Development of a platinum resistance thermometer on the silicon substrate for phase change studies," *Journal of Micromechanics and Microengineering*, vol. 22, p. 085012, July 2012. Publisher: IOP Publishing.

[72] K. G. Kreider, D. C. Ripple, and W. A. Kimes, "Thin-film resistance thermometers on silicon wafers," *Measurement Science and Technology*, vol. 20, p. 045206, Feb. 2009. Publisher: IOP Publishing.

[73] M. J. Laubitz and T. Matsumura, "Transport Properties of the Ferromagnetic Metals. I. Cobalt," *Canadian Journal of Physics*, vol. 51, pp. 1247–1256, June 1973. Publisher: NRC Research Press.

[74] J. W. C. De Vries, "Temperature and thickness dependence of the resistivity of thin polycrystalline aluminium, cobalt, nickel, palladium, silver and gold films," *Thin Solid Films*, vol. 167, pp. 25–32, Dec. 1988.

[75] W. Betteridge, "The properties of metallic cobalt," *Progress in Materials Science*, vol. 24, pp. 51–142, Jan. 1980.

[76] T. Malis, S. C. Cheng, and R. F. Egerton, "EELS log-ratio technique for specimen-thickness measurement in the TEM," *Journal of Electron Microscopy Technique*, vol. 8, no. 2, pp. 193–200, 1988. _eprint: https://onlinelibrary.wiley.com/doi/pdf/10.1002/jemt.1060080206.

[77] C. Cabral, K. Barmak, J. Gupta, L. A. Clevenger, B. Arcot, D. A. Smith, and J. M. E. Harper, "Role of stress relief in the hexagonal-close-packed to face-centered-cubic phase transformation in cobalt thin films," *Journal of Vacuum Science & Technology A*, vol. 11, pp. 1435–1440, July 1993.

[78] G. C. Sneddon, P. W. Trimby, and J. M. Cairney, "Transmission Kikuchi diffraction in a scanning electron microscope: A review," *Materials Science and Engineering: R: Reports*, vol. 110, pp. 1–12, Dec. 2016.

[79] I. A. Blech, "Electromigration in thin aluminum films on titanium nitride," *Journal of Applied Physics*, vol. 47, pp. 1203–1208, Apr. 1976.

[80] P.-C. Wang, G. S. Cargill, I. C. Noyan, and C.-K. Hu, "Electromigration-induced stress in aluminum conductor lines measured by x-ray microdiffraction," *Applied Physics Letters*, vol. 72, pp. 1296–1298, Mar. 1998.

[81] R. Ramji Rao and A. Ramanand, "Thermal expansion and bulk modulus of cobalt," *Journal of Low Temperature Physics*, vol. 26, pp. 365–377, Feb. 1977.

[82] G. S. Rohrer, "Grain boundary energy anisotropy: a review," *Journal of Materials Science*, vol. 46, pp. 5881–5895, Sept. 2011.

[83] G. J. Fan, L. F. Fu, D. C. Qiao, H. Choo, P. K. Liaw, and N. D. Browning, "Grain growth in a bulk nanocrystalline Co alloy during tensile plastic deformation," *Scripta Materialia*, vol. 54, pp. 2137–2141, June 2006.